Stony Brook University

Excitation of Helium to Rydberg States Using STIRAP

A Dissertation Presented

by

Xiaoxu Lu

to

The Graduate School

in Partial Fulfillment of the Requirements

for the Degree of

Doctor of Philosophy

in

Physics

Stony Brook University

May 2011

Stony Brook University

The Graduate School

Xiaoxu Lu

We, the dissertation committee for the above candidate for the Doctor of Philosophy degree, hereby recommend acceptance of this dissertation.

Harold J. Metcalf – Dissertation Advisor
Distinguished Teaching Professor, Department of Physics and Astronomy

Thomas K. Hemmick – Chairperson of Defense
Distinguished Teaching Professor, Department of Physics and Astronomy

Xu Du
Assistant Professor, Department of Physics and Astronomy

Thomas Pattard
Senior Assistant Editor, American Physical Society

This dissertation is accepted by the Graduate School.

Lawrence Martin
Dean of the Graduate School

Abstract of the Dissertation

Excitation of Helium to Rydberg States Using STIRAP

by

Xiaoxu Lu

Doctor of Philosophy

in

Physics

Stony Brook University

2011

Driving atoms from an initial to a final state of the same parity via an intermediate state of opposite parity is most efficiently done using STIRAP, because it does not populate the intermediate state. For optical transitions this requires appropriate pulses of light in the counter-intuitive order - first coupling the intermediate and final states.

We populate Rydberg states of helium ($n = 12 \sim 30$) in a beam of average velocity 1070 m/s by having the atoms cross two laser beams in a tunable dc electric field. The "red" light near $\lambda = 790 \sim 830$ nm connects the 3^3P states to the Rydberg states and the "blue" beam of $\lambda = 389$ nm connects the metastable 2^3S state atoms emitted by our source to the 3^3P states. By varying the relative position

of these beams we can vary both the order and the overlap encountered by the atoms. We vary either the dc electric field and fix the "red" laser frequency or vary the "red" laser frequency and fix the dc electric field to sweep across Stark states of the Rydberg manifolds.

Several mm downstream of the interaction region we apply the very strong bichromatic force on the $2^3S \rightarrow 2^3P$ transition at $\lambda = 1083$ nm. It deflects the remaining 2^3S atoms out of the beam and the ratio of this signal measured with STIRAP beam on and off provides an absolute measure of the fraction of the atoms remaining in the 2^3S state. Simple three-level models of STIRAP all predict 100% excitation probability, but our raw measurements are typically around half of this, and vary with both n and l of the Rydberg states selected for excitation by the laser frequency and electric field tuning on our Stark maps. For states with high enough Rabi frequency, after correction for the decay back to the metastable state before the deflection, the highest efficiencies are around 70%.

An ion detector readily detects the presence of Rydberg atoms. We believe that the observed signals are produced by black-body ionization at a very low rate, but sufficient to ionize about $0.5 \sim 1.0$ % of the atoms in a region viewed by our detector. Many measurements provide support for this hypothesis.

For my family and friends

Contents

List of Figures

List of Tables

Acknowledgements

I have spent enjoyable and exciting six years at Stony Brook. This work presented in this thesis would not have been possible without so many people's kind help. I am heartily thankful to everyone who has helped me in my journey and because of whom my graduate experience has been one that I will cherish forever.

First of all, I would like to express my deep and sincere gratitude to my advisor, Prof. Harold Metcalf. Without his inspirational guidance, I could never finish my doctoral work. His encouragement gave me confidence to overcome every difficulty I encountered. I have learned not only a lot of physics, but also, more importantly, the way to solve problems, which will benefit my whole life.

I would also like to thank my colleagues for making my life as a graduate student more enjoyable through collaboration and friendship. I want to thank Seung Hyun Lee and Andy Vernaleken for their previous work. Without their preliminary setup, I would not know where to start. I was lucky to have Jonathan Kaufman work together with me in the first two years. It was a tough time for me to take over the whole experiment at the beginning, but his passion in science and his optimism inspired me. I will never forget the days and nights that we worked together in the lab. I would also like to thank Yuan Sun for his help in the second half of my project. I can not imagine how I could manage to run the experiments on my own. I am sure he is going to do a great job in keeping the experiment running and

Chapter 1

Introduction

1.1 The Big Picture

Atom optics, which is a field of research exploring the possibilities of manipulating beams of atoms in the same way that conventional optics controls light beams, has become the subject of intense investigation in the last two decades. But the history actually started with Stern and Gerlach's experiments in the early 1920s [1] [2], followed by the atomic-diffraction experiments by Estermann [3] and others in the early 1930s . These demonstrated unambiguously that wave mechanics also applies to composite particles. These pioneering experiments were truly difficult to carry out due to the extremely short room-temperature atomic de Broglie wavelength ($\lambda_{dB} = h/Mv$, where v is the velocity of atoms), of the particles, of the order of a fraction of an Angstrom.

In the late 1970s, a renaissance in atom optics research took place when Hänsch and Schawlow proposed a method to cool atomic gases using laser radiation [4]. Experimental and theoretical extensions of this idea eventually led to the 1997 Nobel Prize for laser-cooling. With laser cooling, one can readily bring atomic samples down to temperatures of

the order of 10^{-6} K or less, so the atomic de Broglie wavelengths are on the order of microns or longer [5]. The creation of the first Bose-Einstein condensates in a dilute gas of alkali atoms [6] depended crucially on these achievements and was honored with a Nobel Prize in 2001. The new experimental tools, and the availability of widely tunable laser sources in particular, revolutionized atom optics, and it is hardly possible to overestimate their impact on contemporary atomic, optical, and molecular physics.

It has been shown extensively that atomic beams can be reflected [7], diffracted [8][9] and focussed [10][11][12][13], with laser beams tuned around atomic resonances. Besides using light (oscillating electric field) to steer atoms, one can also achieve useful focusing by adding a static electric field (or magnetic field) gradient on a beam of slow neutral atoms [14]. This focussing force arises from the interaction of the electric field gradient with the induced electric dipole moment of the atom. Kalnins et. al. [15] have used an electrostatic lens with three focusing elements in an alternating-gradient configuration to focus a fountain of cesium atoms in their ground state. Because no external magnetic fields are introduced, electric field gradient focusing is suitable for magnetic-field sensitive experiments such as atomic fountain clocks and electron electric dipole moment experiments.

Ground state neutral atoms are not affected greatly by electric fields as they don't have large electric dipole moments, so huge electric field amplitudes and long acceleration times are needed to get effective focusing, as in [15]. However, by exciting neutral atoms to high Rydberg states, their electric dipole moments are increased considerably. The goal of our work was to demonstrate the focusing effect of an inhomogeneous electrostatic field on neutral atoms by manipulating the trajectories of the Rydberg atoms. Although the original idea for this focussing was first introduced in 1981 [16], it took rather long time to develop the proper experimental techniques to realize it. In this thesis, we concentrate on the sufficient production of Rydberg atoms in helium via the STIRAP technique.

2

In our experiments, we excite He atoms to Rydberg States ($n = 12 \sim 30$) from a metastable (2^3S_1) atomic beam (He*). The atoms in the beam cross two laser beams in a tunable dc electric field. The "red" light near $\lambda = 790 \sim 830$ nm connects the 3^3P states to the Rydberg states and the "blue" beam of $\lambda = 389$ nm connects the metastable 2^3S state atoms emitted by our source to the 3^3P states. By varying the relative position of these beams we can vary both the order and the beam overlap encountered by the atoms. This two-step process allows a very high excitation efficiency when the atoms encounter the sequence of light pulses that corresponds to Stimulated Rapid Adiabatic Passage (STIRAP) [17][18].

Our interests in highly efficient production of Rydberg atoms stems from the use of inhomogeneous electrostatic fields to control atomic motion for use in atomic optics, but STIRAP itself is a very interesting and broad topic, and is a powerful way to coherently transfer population in a three-level system. Ideally, in the adiabatic limit almost 100% of the population can be transferred to the target state, whether in a Λ scheme, $\vee$ scheme or ladder scheme. It is not sensitive to moderate changes in pulse parameters such as pulse length, amplitude, or intermediate detuning (as along as two-photon resonance condition is satisfied). Efficient population transfer using STIRAP has been demonstrated experimentally as well [19] [20][21], but mostly in low-lying states. STIRAP excitation to high Rydberg states is also possible, but difficult due to the low oscillator strength of optical Rydberg transitions [22]. To better understand the STIRAP process, we want to investigate extensively the STIRAP excitation to different Rydberg states and measure the absolute efficiency of excitation.

One of the possible applications of this atom optic technique is neutral atom nanolithography [23]. The high internal energy of He* atoms could be exploited to create nanoscale structure through a resist assisted lithography mode [24]. Preliminary results showing the focusing effect of an electric hexapole lens on Rydberg atoms have been described in S-H.

Lee's thesis [25].

1.2 Rydberg Atoms

1.2.1 General Properties

Rydberg atoms are excited atoms with one or more electrons that have a very high principal quantum number [26]. Rydberg states of atoms have been attracting the interest of atomic physicists for more than one century. At the end of the 19th century, Balmer related a series of spectral lines of atomic hydrogen to the famous formula named after him [26]

$$\lambda = \frac{bn^2}{n^2 - 4} \tag{1.1}$$

with $b = 3645.6$ Å. It became clear that the series related energy differences between $n = 2$ and high energy states after Hartley [27] expressed Balmer's formula in terms of wave numbers instead of wavelength:

$$\nu = (\frac{1}{4b})(\frac{1}{4} - \frac{1}{n^2}) \tag{1.2}$$

High lying states are called Rydberg states because Rydberg was able to express the wavenumbers of different series of alkali atoms [28] with a single formula

$$\nu_l = \nu_{\infty l} - \frac{R_y}{(n - \delta_l)^2} \tag{1.3}$$

where $\nu_{\infty l}$ is the series limit, δ_l is the quantum defect and $R_y = 109721.6$ cm^{-1} is the universal Rydberg constant. Another great achievement of Rydberg was the discovery that the lines connecting series can be obtained by setting $\nu_{\infty l} = R_y/(n' - \delta_l)^2$. The physical meaning of the principal quantum number n and the Rydberg constant became clear after Bohr proposed

his model for the hydrogen atom in 1913. Then R_y could be written as

$$R_y = \frac{Z^2 e^4 m_e}{2(4\pi\epsilon_0\hbar)^2} = Z^2 \frac{mc^2\alpha^2}{2} \tag{1.4}$$

where ϵ_0 is the permittivity of free space, $\hbar$ is the Planck's constant, Z is the proton number, e is the electron charge and m_e is the electron mass.

Rydberg atoms can be generated by charge exchange or electron impact [26]. When a positive ion collides with a ground state atom, the ion captures one electron from the ground state atom and is left in a Rydberg state. If an electron beam hits ground state atoms, it could also possibly excite them to Rydberg states. Optical excitation became feasible with the advent of lasers. The big advantage of optical excitation over charge exchange and electron impact excitation is that individual Rydberg states can be accurately accessed through tuning of the photon energy.

These Rydberg atoms have a number of peculiar properties so that some of the effects impossible to detect in ground state atoms become obvious in Rydberg atoms. As listed in Table 1.1, the orbit radius of Rydberg atoms is much larger, $\propto n^2$. As a consequence, Rydberg atoms have very large dipole moments and polarizabilities which lead to a pronounced Stark effect [29] and van der Waals interaction between pairs of Rydberg atoms [30][31]. Neighboring states with different principal quantum numbers are close so that transition between Rydberg states can be driven by microwaves. Furthermore, Rydberg atoms are particularly sensitive to their local environment. Ambient blackbody radiation redistributes Rydberg atoms between neighbouring energy states and even leads to ionization and could significantly shorten the total lifetime of the Rydberg state. And with the production of cold Rydberg atoms, there has been renewed interest in low temperature Rydberg systems for applications such as studies of collective effects [32] and formation and recombination of

Property	Formula	n-dependence
Binding energy E_n	$-\frac{R_y}{(n-\delta_l)^2}$	n^{-2}
Energy spacing	$E_n - E_{n-1}$	n^{-3}
Orbital radius $\langle r \rangle$	$\simeq \frac{1}{2}(3(n-\delta_l)^2 - l(l+1))$	n^2
Geo. cross section	$\pi \langle r \rangle^2$	n^4
Dipole moment	$\langle nl|er|nl+1 \rangle$	n^2
Polarizability	$2e^2 \sum_{n=n',l,m} \frac{|\langle nlm|z|n'l'm'\rangle|^2}{E_{nlm}-E_{n'l'm'}}$	n^7
Radiative lifetime	$\left(\frac{e^2}{3\hbar c^3 \pi \epsilon_0} \sum_{n<n'}^{l=l\pm1} \frac{l_{max}}{2l'+1}\omega^3 |\langle n'l'|r|nl\rangle|^2\right)^{-1}$	n^{-3}
Blackbody transition	$\frac{1}{\tau_{nl}^{bb}} = \frac{4\alpha^3 kT}{3n^2}$	n^{-2}
Fine Structure		n^{-3}

Table 1.1: Selected properties of Rydberg atoms and their dependence on the principal quantum number [26].

ultracold Rydberg plasmas [33] and quantum computing [34]. In the following sections of this chapter, I am going to focus only on the important properties related to our experiments, the quantum defect and Stark effect on helium Rydberg states.

1.2.2 Quantum Defects

The energy levels of hydrogen can be easily calculated from the Schrödinger equation. These levels turn out to be only dependent on the principal quantum number n, $E_n = -\frac{R_y}{n^2}$, such that different l states are degenerate. In non-hydrogen atoms, the excited valence electron in a Rydberg state does not only interact with the nucleus but also with the core electrons. When the valence electron is far away from the nucleus, the many core electrons provide effective shielding from the electric field of the nucleus, so that the outer electron

generally "sees" a nucleus with only one proton and will behave much like the electron of a hydrogen atom. However, if orbits of electrons pass through the core of shielding electrons, then the electron will occasionally "see" the whole nucleus. Then the energy levels of non-hydrogen atoms will be depressed with respect to their hydrogen counterparts, and can be written as [35]

$$E_n = -\frac{R_y}{(n - \delta_l)^2} \tag{1.5}$$

where the quantum defect δ_l in general is a function of n and can be described by the Rydberg-Ritz formula [36]

$$\delta_l = a + bE_n + cE_n^2 + dE_n^3 + ... \tag{1.6}$$

where a, b, c, d,... are the Rydberg-Ritz coefficients and depend on the angular momentum l. Their values for triplet helium atoms are listed in Table 1.2. With low angular momentum states, the shielding effect breaks down a bit and the electron energy levels can not mimic those of hydrogen without the shielding, hence the quantum defect is higher. For S states, the quantum defect is relatively large since electrons with zero angular momentum essentially pass cleanly through the core of shielding electrons. For D states, having higher angular momentum, the quantum defect is a lot smaller, as their orbits will not pass through the core so deeply. Furthermore, even though the high - l Rydberg electrons do not penetrate the core, they do polarize it, and this also leads to non-zero quantum defects [37].

1.2.3 Stark Effect in Helium Atoms

Because the helium Rydberg states are hydrogenlike in many aspects, let's first look at the Stark structure of hydrogen. The Schrödinger equation in atomic units ($\hbar = e = m = 1$)

7

l - value	a	b	c	d
0	0.296609	-0.038840	0.004960	0.000000
1	0.068320	0.017870	-0.017190	0.000000
2	0.002869	0.006220	0.000000	0.000000
3	0.000240	-0.002090	0.000000	0.000000

Table 1.2: Rydberg-Ritz coefficients for the calculation of quantum defect of triplet Helium without considering spin-orbit splitting [38]

for the hydrogen atom in an external field is

$$(-\frac{1}{2}\nabla^2 - 1/r + Fz)\Psi(\vec{r}) = W\Psi(\vec{r}) \tag{1.7}$$

W is the energy and F is the magnitude of the electric field in atomic units, $5 \times 10^{11} V/m$, which is taken to lie along the z axis. Eqn. 1.7 may be separated in parabolic coordinates and can be solved analytically for zero electric field [26]. If the electric field is not zero, perturbation theory can be applied to evaluate the perturbed energies and the results are given as

$$W_0 = -1/2n^2$$
$$W_1 = \frac{3}{2}n(n_1 - n_2)F \tag{1.8}$$
$$W_2 = -\frac{1}{16}n^4[17n^2 - 3(n_1 - n_2)^2 - 9m^2 + 19]F^2$$

where the quantum numbers n and m label the principal and magnetic quantum numbers respectively, and n_1, n_2 are non-negative integers obeying

$$n_1 + n_2 + |m| + 1 = n \tag{1.9}$$

For atoms other than hydrogen, there are important differences due to the presence of the finite sized ionic core. The wavefunction is no longer separable in parabolic coordinates. The single-electron Hamiltonian in an external electric field reads

$$H = H_0 + Fz + H_{fs} \tag{1.10}$$

where H_0 is the unperturbed Hamiltonian and H_{fs} is the energy shift due to fine structure which is small in high n states of He and can be neglected. We are interested in the energies of the Stark states as a function of field strength, the so called Stark map. To calculate the eigenvalues of (1.10), we represent the Hamiltonian in the basis provided by the eigenvector $|nlm\rangle$ of the field free Hamiltonian in a spherical basis. As the eigenvalues of the field-free Hamiltonian are known, we only have to evaluate the off-diagonal matrix elements

$$\langle nlm|Fz|n'l'm'\rangle = F\langle nlm|r\cos\theta|n'l'm'\rangle \tag{1.11}$$

$$= \delta(m,m')\delta(l,l'\pm1)F\langle lm|\cos\theta|l'm'\rangle\langle nl|r|n'l'\rangle \tag{1.12}$$

The angular part of the matrix elements has well-known analytic solutions in a spherical basis. We can numerically evaluate the radial matrix elements of the Stark operator as described by Zimmerman et al.[29].

The resulting energy levels for He $n = 26$ are shown in Figure 1.1. The figure demonstrates several important properties: (1) the strong suppression of the s, p, d states due to their quantum defects; (2) the lifting of the zero-field degeneracy of the $|nl\rangle, l > 3$ states; (3) avoided crossings of appreciable size. Avoided crossings arise from the fact that a non-hydrogen core breaks the Coulomb symmetry and couples the Stark levels. The size of an avoided crossing is given by the strength of the coupling.
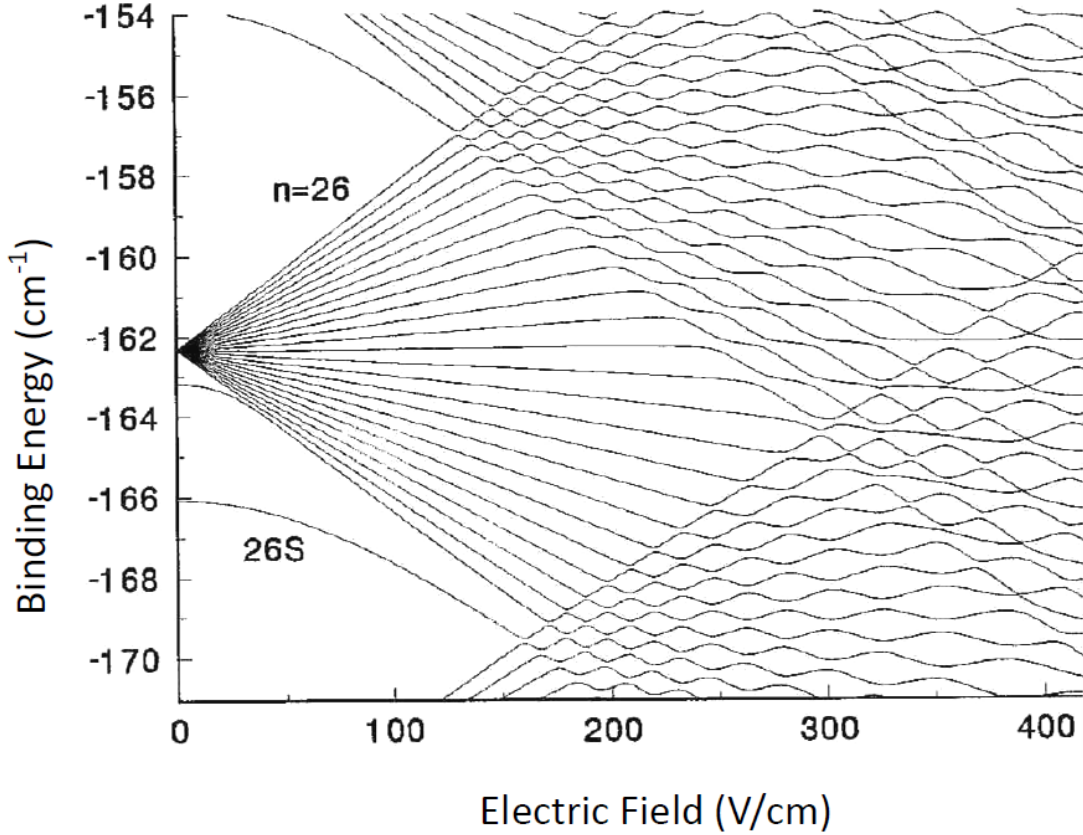
Figure 1.1: Stark Structure of Helium atom for $n = 26$ (without considering the fine structure) [38]

With an applied electric field, all the different l levels are mixed and l is not a good quantum number any more. We usually call the region with mixing l states the manifold, while the S states at low electric field are well separated and easily distinguished.

Meanwhile, at different electric fields, different Stark states have different oscillator strengths for transitions to other states. The oscillator strength from level nlm to level $n'l'm'$ is defined by

$$f_{n'l'm',nlm} = 2\frac{m}{\hbar}\omega_{n'l',nl}|\langle n'l'm'|z|nlm\rangle|^2 \tag{1.13}$$

For He Rydberg Stark states, these oscillator strengths can only be calculated by numerical
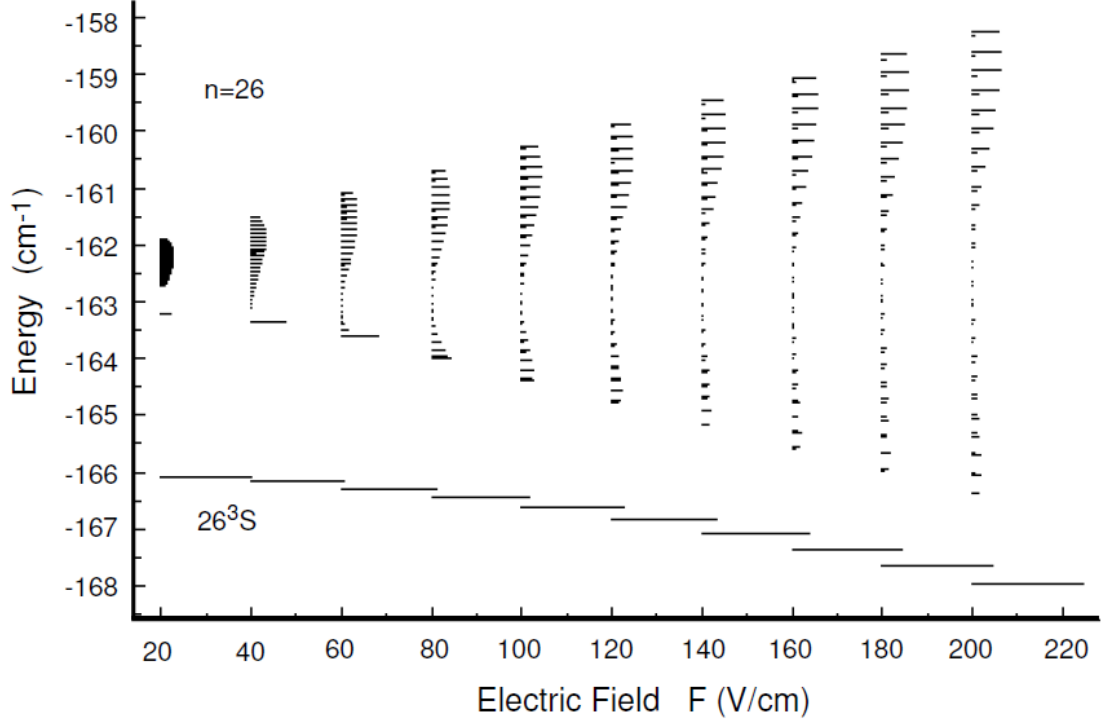
Figure 1.2: Relative Transition strength to $n = 26$ Stark map from 3^3P_2 for triplet Helium atom, which is given by the width of each line [38].

integration. The resulting transition intensity of the excitation of $n = 26$ Stark states from the 3^3P_2 state is shown in figure 1.2 [38]. This is qualitatively applicable to other n states. At zero field, the S and D states are directly dipole coupled to the P state, resulting in large transition probabilities. By increasing the electric field, there are dramatic changes in the distribution of the oscillator strength across the Stark manifold. The minimum near the center (~ 163 cm^{-1}) was attributed to the $S - D$ interference of the transition momentum between the 3^3P and final Stark states [39]. Before reaching the anti-crossing region, the coupling between the S state and other manifold states is very small due to the quantum defect, so the transition strength does not change much. These different transition strengths will lead to different Rabi frequencies and also different lifetimes.

11

1.3 Excitation of Helium to Rydberg States

The atomic energy level scheme for He is shown in Figure 1.3. He is a closed shell system like all rare gases. When one s-electron is excited from the core to a high lying metastable state, the atom behaves effectively like a single electron atom. However, metastable helium (He*) does not have a closed inner shell like alkali metals, but an open S-state core. The coupling between the core and excited electron spins results in either spin-opposed (singlet) or spin-parallel (triplet) states, causing the splitting within the triplet P states shown in Figure 1.3. However, the level structure is simplified by the fact that there is no nuclear spin, so there is no hyperfine structure.

Neither the singlet nor triplet S states can decay to the ground 1^1S_0 state via an electric dipole transition due to the $\Delta L = \pm 1$ selection rule (L being the orbital angular momentum quantum number which is zero for S states). Consequently the singlet and triplet S states are metastable, with the 2^1S_0 state having a lifetime of ~ 19 ms. However, decay of the 2^3S_1 state is doubly forbidden because a transition to the ground state also requires that one of the electron spins has to flip to create a ground singlet state. This gives rise to the extremely long metastable lifetime, predicted to be 8000 s [40], so that the metastable state can essentially be regarded as the effective ground state. The He* 2^3S_1 state is the longest lived of any atomic or molecular species and decays via a single-photon magnetic dipole transition at 62.5 nm rather than via a two-photon process [41]. Meanwhile, the stored metastable energy (19.82 eV) is the highest for any metastable species, enabling detection of single atoms using charged particle detectors, electron multipliers, or microchannel plates (MCPs) with near unity detection efficiency [42]. Similarly, the large stored energy in He* allows for efficient damage of photoresist-coated surfaces for applications in atom lithography.

Since we can not excite the ground state He to metastable states by any optical transition,
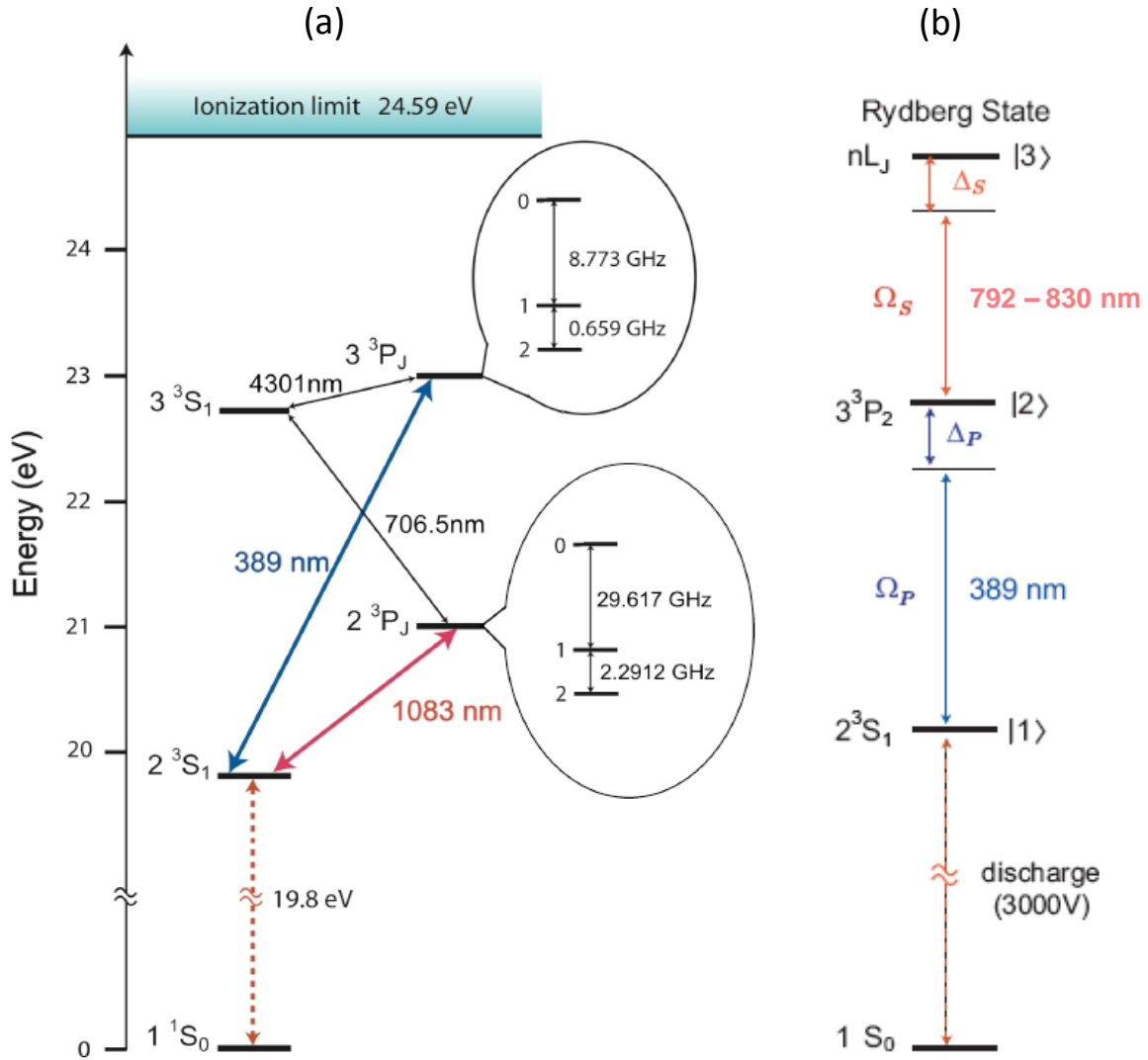
Figure 1.3: Energy level diagram for the triplet states of Helium (a) and the transition scheme to the Rydberg states (b). Ω_S and Ω_P are the Rabi frequencies of the Stokes and the Pump lasers, respectively. Δ_S and Δ_P are their detunings, which will be discussed in more detail in Chapter 4.

as a first step of excitation, the He* atoms are produced in a reverse flow dc discharge source. The source output is about 10^{14} He* atoms/sr·s, a few parts in 10^6 of the total He flux. The ground state atoms are effectively lost as they cannot be detected and collisions of He* on ground state He have negligible effect on the populations. Chapter 2 gives a detailed description of the source, as well as the interaction region and the available detection systems in the vacuum system.

The three-level excitation scheme used in this experiment is illustrated in Figure 1.3(b). After the dc discharge brings 10^{-5} of the total He atoms to the 2^3S_1 metastable state, a frequency-doubled Ti:Sapphire laser of $\lambda = 389$ nm ("blue") connects the metastable 2^3S_1 state ($|1\rangle$) atoms emitted by our source to the 3^3P_2 ($|2\rangle$) state. Another independent Ti:Sapphire laser, which could be adjusted in its wavelength from $780 \sim 830$ nm ("red") is used to drive the excitation from the intermediate state 3^3P_2 to selected Rydberg states ($|3\rangle$). We always keep the "blue" light locked on $|1\rangle \to |2\rangle$ resonance, and then, either vary the dc electric field and fix the "red" laser frequency or vary the "red" laser frequency and fix the dc electric field to sweep across the Stark states of the Rydberg manifolds. Details of the laser systems will be covered in Chapter 3.

The short lifetime of the intermediate 3^3P_2 state (~ 94.8 ns [5]) introduces the main loss during the excitation process due to its spontaneous emission to 2^3S_1 and 3^3S_1 states. Instead of doing the excitation in the intuitive order, we employ the Stimulated Raman Adiabatic Passage (STIRAP) technique by first coupling the intermediate and final states, which allows us to achieve much higher transfer efficiency, as will be described in detail in Chapter 4.

The third laser at $\lambda = 1083$ nm coupling the 2^3S_1 and 2^3P_2 states is not used for excitation, but as a tool to separate the remaining metastable He* from the other Rydberg state atoms for excitation rate measurements. Several mm downstream of the interaction region, we

apply the very strong bichromatic force [43] on the $2^3S_1 \rightarrow 2^3P_2$ transition. It deflects the remaining 2^3S_1 atoms out of the beam and the ratio of this signal measured with the STIRAP beams on and off provides an absolute measure of the fraction of the atoms remaining in the 2^3S_1 state. The setup of absolute efficiency measurement followed by the experimental results will be discussed in Chapter 5.

After He atoms are excited to Rydberg states, they are easily ionized and then collected by our ion detector. We believe that the observed signals are produced by black-body ionization at a very low rate, but sufficient to ionize about $0.5 \sim 1$ % of the atoms in a region viewed by our detector. Many measurements provide support for this hypothesis. Details are provided in Chapter 6 followed by a summary and outlook in Chapter 7.

Chapter 2

Vacuum System

In earlier experiments, we used an old vacuum system pumped by three diffusion pumps backed by two big mechanical pumps, which has been described very well in S-H. Lee's and A. Vernaleken's theses [25][44]. But that vacuum system was all O-ring sealed and it leaked here and there from time to time. And with some oil contamination, the pressure was about $\sim 10^{-5}$ Torr in the source chamber, $\sim 2 \times 10^{-6}$ Torr in the interaction chamber and $\sim 8 \times 10^{-7}$ Torr in the detection chamber, and not very stable. When the booster pump finally stopped working, we started to take apart the old vacuum system and build a new one in early 2007. Here, I am just going to talk about the new system in which my experiments were done.

2.1   The Whole System

The vacuum system is primarily made of stainless steel with conflat flanges sealed with copper gaskets. It consists of three main parts: the source chamber where the metastable helium atoms are created, the interaction chamber where we do STIRAP to excite the atoms

to the Rydberg states and the detection chamber where the atomic distribution is measured after a long beam line. The layout of the system is shown in Figure 2.1.

The source chamber and the interaction chamber are separated by a wall with a 5 mm aperture so that they are differentially pumped. The source chamber is pumped by a Pfeiffer TPH330 Turbo pump (330 L/s) backed by a Welch Duo-Seal mechanical pump 1397 and the source outlet is pumped by a Welch Duo-seal pump 1402. The interaction chamber is pumped by a Pfeiffer TPH 270 Turbo pump (270 L/s) with a Welch 1376 mechanical pump acting as a backing pump. The bellows between the chambers and Turbo pumps serve as vibration dampers. Although the TPH330 Turbo only pumps the source chamber, which is a much smaller volume, it has to handle the large influx of helium gas when the source is running (as described in the following section). During operation, the detection chamber and the interaction chamber are usually connected, but we have another ion pump on the detection chamber, so the detection chamber pressure is typically a little lower. Typical pressure in our vacuum system (without gas flow to the source) is 3.2×10^{-7} Torr in the source chamber, 3.6×10^{-7} Torr in the interaction chamber and 2.5×10^{-7} Torr in the detection chamber. With source running, the pressure in the interaction chamber is about 10^{-6} Torr.

The vacuum system is constructed such that the chambers can be vented to atmosphere pressure with the Turbo pumps on. In order to do so, the two six inch O-ring sealed gate valves inserted between the chamber and turbo pumps in the source region and the interaction region are closed. Afterwards, when we want to return to high vacuum, we close the foreline valves FS and IS in Figure 2.1, and open the roughing valves RS and RI. It takes a few minutes to pump the chamber below 100 mTorr, then we close the RS and RI, open FS, IS and two gate valves to let the Turbo pumps work on the chambers as usual. An additional gate valve isolates the detection chamber from the rest of the vacuum system

Liquid N$_2$ reservoir

26cm 140cm

Interaction chamber

Detection chamber

Source

Gate valve

Ion Pump

He out He in

Gate valve

Welch Duo 1402

RS valve

to Sorption pumps

Vibration damper

RI valve

Gate valve

roughing line

TPH 330

Vibration damper

roughing line

TPH 270

Safety valve

foreline

FS valve

RI valve

foreline

Safety valve

Welch Duo 1397

RI valve

Welch Duo 1376
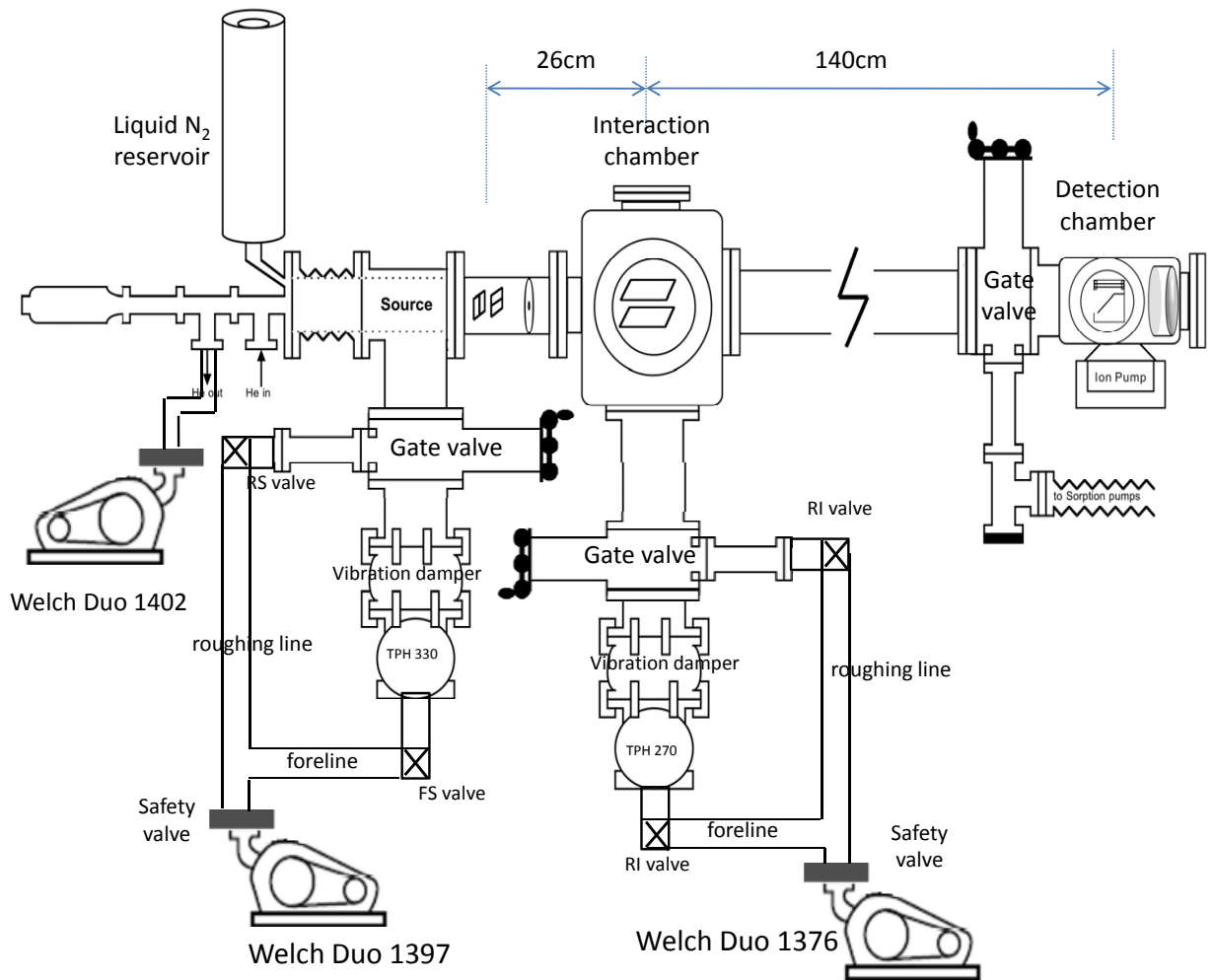
Figure 2.1: Vacuum system layout. It has three main chambers: source chamber, interaction chamber and detection chamber

18

and the detection chamber can be roughly pumped by two cryogenic sorption pumps with molecular sieve material inside.

To prevent oil from back-streaming into the system from mechanical pumps in an emergency, such as power outage, we put pneumatic safety valves on all three mechanical pumps. The valves remain open if power is on and the pressure on the mechanical pumps side is lower than the foreline side. If the power is off or something is wrong with the mechanical pumps, the valves would shut themselves off immediately so that the mechanical pumps are isolated from the rest of the system. For further protection from oil contamination, we have coaxial copper sieve foreline traps on both Turbo backing pipes.

2.2   Source Chamber

Since the energy gap between the 2^3S_1 and the 1^1S_1 state is about 19.8 eV and the transition itself is doubly forbidden, we can not excite the ground state He to the metastable state by any optical transition. Instead a metastable helium beam is created by a dc discharge in moderate pressure He gas. The gas then freely expands to a lower pressure region through a small aperture.

The source we are using is based on the reverse flow design developed by Kawanaka et al. [45], slightly modified by Mastwijk et al. [46], and fabricated at Utrecht University in the Netherlands. It was first assembled in July 2007 and started to produce a stable metastable helium beam in Oct. 2007.

As shown in Figure 2.2, there is a 1 cm diameter pyrex glass in the center, held by a Teflon piece at the narrow end and by an O-ring at the other end, inside a 3 cm stainless steel coaxial jacket which is cooled by liquid nitrogen to 77 K. Helium gas flows into the chamber between the gas tube and the cooled jacket. The Teflon spacer further narrows
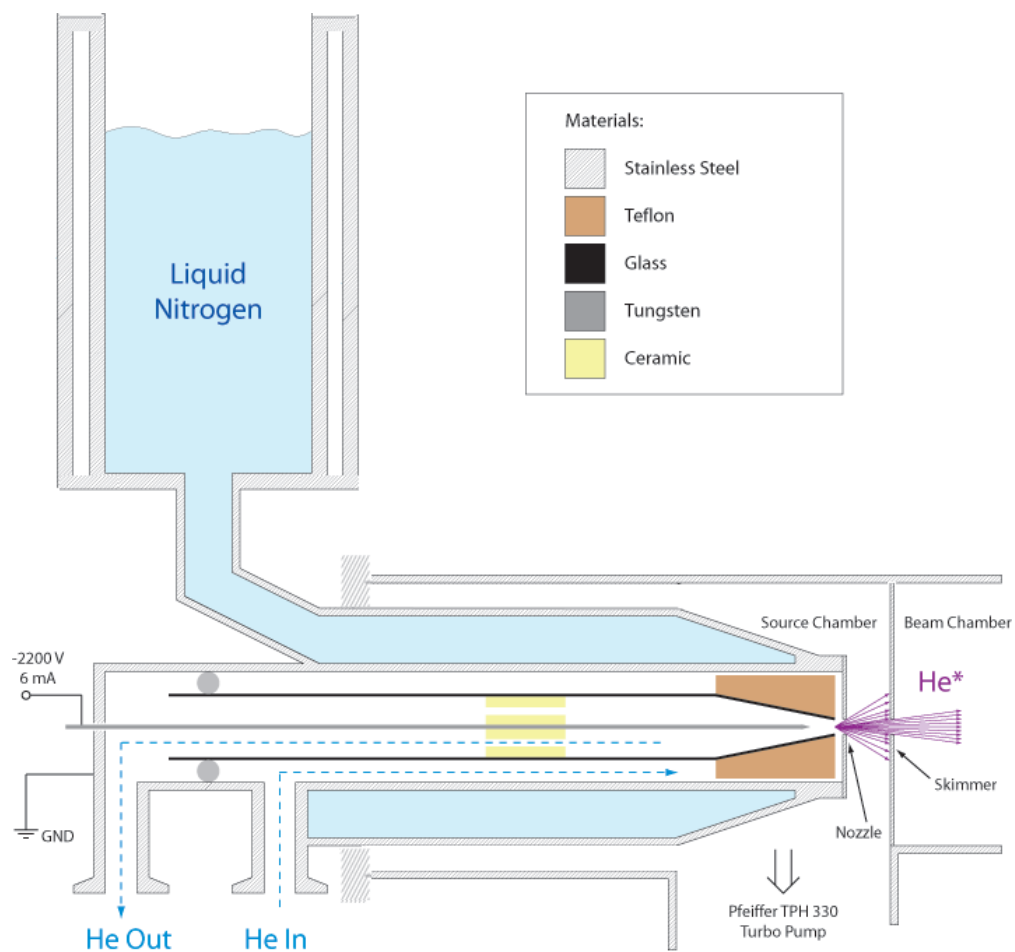
Figure 2.2: Metastable helium source with the reverse flow design [47]

the spacing and enhances the contact between the helium atoms and cold wall, so that the atoms are considerably cold when they reach the tip of the glass tube, i.e. the discharge region. Then most of the atoms are pumped out through the glass tube by the Welch 1402 mechanical pump. Inside the glass tube, there is a 1 mm diameter tungsten rod with one end sharpened to a needle-like point, centered in place by a ceramic spacer. The spacer has several channels cut into it to allow appropriate flow of helium gas. At the end of the steel jacket housing, in front of the glass tube, a piece of aluminum plate with a 0.5 mm aperture serves as a nozzle plate. The tungsten needle is mounted on a linear motion feedthrough (range of motion: 1 inch) so that we can adjust the distance between the tip of the needle and the nozzle plate. The Tungsten needle and the nozzle serve as cathode and anode for the dc discharge, respectively. To start the discharge source, -2200 V are supplied to the needle while the nozzle plate is held at ground potential.

In the high field region, the background gas gets field ionized and forms a discharge plasma consisting of He ions, metastable He (He*) and other excited states of He. Unfortunately, most of the metastable atoms are quenched by collisions in the high pressure dense region. But outside the discharge region, after the nozzle plate, the density is lower and collisions are less likely. Therefore, a fraction of the He atoms are excited again to the metastable state by collisions with secondary electrons. Overall, the metastable state only makes up a small fraction ($10^{-4} \sim 10^{-5}$) of the total number of He atoms in the beam. After the nozzle plate, there is a 3 mm aperture, called a skimmer plate, attached to the wall separating the source chamber and the interaction chamber. The metastable He atoms fly through the skimmer plate into the interaction chamber together with charged particles, visible light, UV light and ground state He. To allow for alignment of the nozzle aperture to the skimmer aperture, the source is attached to the chamber by a bellows piece.

To make the He* source work properly, the following parameters must be optimized,

mostly by trial and error. Flow pressure, distance from the needle to the nozzle plate, and the discharge current are all important. It was found that the cleanliness of the glass tube, the sharpness of the tungsten needle, whether the needle is centered inside the glass tube, and the quality of the nozzle plate surface are also important.

In our setup, we have a needle valve in the He inlet line to control the flow. However, we measure the outlet pressure instead of the inlet pressure by a digital Granville-Phillips Convectron gauge. The source could run steadily from about 1.8 Torr to 4 Torr. But higher outlet pressure leads to fewer metastable He atoms. The absolute amount of helium atoms at 4 Torr is only about 55% of what it is at 2 Torr (see Figure 5.10). Running at lower pressures also causes the discharge to become unstable. To get a stable intense metastable beam, we usually run the source at about 2.2 Torr.

A high voltage on the needle tip is required to create a high electric field to start the source. But the higher the current, the higher is the velocity of the He* in the beam. Since running the discharge at high currents dramatically shortens the source lifetime, we run our source in a current limiting mode. We put a 100 MΩ power resistor in series with the source circuit. Although the discharge could run from about 2.5 mA to 12 mA, we typically run the source at about $7 \sim 8$ mA with -2200 V at the needle as a trade-off among metastable productivity, longitudinal velocity and source lifetime.

Sometimes, if the source doesn't start immediately after we turn on the voltage, we might need to adjust the needle position slightly. As long as the source is lit, the needle position doesn't matter that much. We have a 2-3/4" Conflat window around the skimmer plate region so that we can see if the source if working properly or not. When it is working correctly, the source glows a blueish color and is very bright. If there is only a very weak yellow spot around the skimmer aperture, there is probably a discharge inside the glass tube. And occasionally, when the glow is much dimmer, it is just not the right state of discharge.

With source gas flowing, the pressures in the source and the interaction chamber are about 10^{-5} Torr and 10^{-6} Torr respectively as measured by ion gauge respectively. The source turbo pump backing pressure reads about 100 mTorr and the interaction chamber turbo pump backing pressure rises up to 50 mTorr. Under steady running conditions, our source yields $\sim 0.5 \times 10^{14}$ He* atoms/(sr·s) with a average longitudinal velocity about 1070 m/s and full width at half maximum of about 480 m/s.

2.2.1 Time of Flight Measurement

The longitudinal velocity distribution of the atomic beam was characterized by a time-of-flight (TOF) measurement. A mechanical chopper was put in the interaction region with a linear motion feedthrough. Then we used the SSD detector as described in Section 2.4.2 to detect the beam about 1.4 meters downstream in the detection region. Measuring the arrival times of the light and atoms yields the longitudinal velocity distribution of the atomic beam.

The chopper moves a resonant frequency of about 175.9 Hz with a small slit about 300 microns wide glued on it. Figure 2.3 shows a typical signal of the TOF measurement. The first peak corresponds to UV photons from the source discharge and the second peak originates from the metastable atoms. The delay time from the first peak is the time it takes for the atoms to travel from the chopper to the detector. So from the curve, we get an average longitudinal velocity of 1070 m/s and velocity spread of about ± 240 m/s. The data was taken with flow pressure at about 1.8 Torr and needle voltage of 2.3 kV voltage with 8 mA current.

$V_{longitudinal} = 1070 \pm 240$ m/s
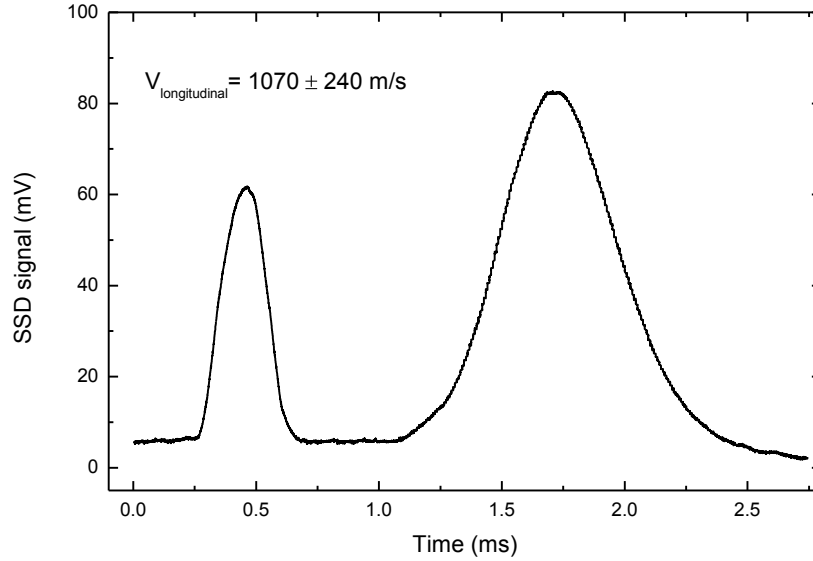
Figure 2.3: Longitudinal velocity distribution of He* atoms determined in a time-of-flight (TOF) measurement

2.3 Interaction Chamber

The atoms entering the interaction region are collimated by the slits about 23 cm downstream from the skimmer plate. A horizontal slit about 0.3 mm wide is mounted on a vertical motion feedthrough and a vertical slit about 0.5 mm high is mounted on a horizontal feedthrough so that we can independently move the slits vertically and horizontally . Then, at an additional 5 cm downstream before the interaction chamber, we have another round stainless steel plate with a 2 cm diameter hole in the center, making good contact with the inside wall, to block all other particles flying around in the chamber.

Figure 2.4(a) shows the inside of the interaction chamber. Two electric field plates made of brass whose dimensions are shown in Figure 2.4(b) are located at the center of the chamber with their short side aligned approximately parallel to the atomic beam. On both sides of the interaction chamber, we have 4.5" diameter windows on 6" conflat flanges, antireflection

24
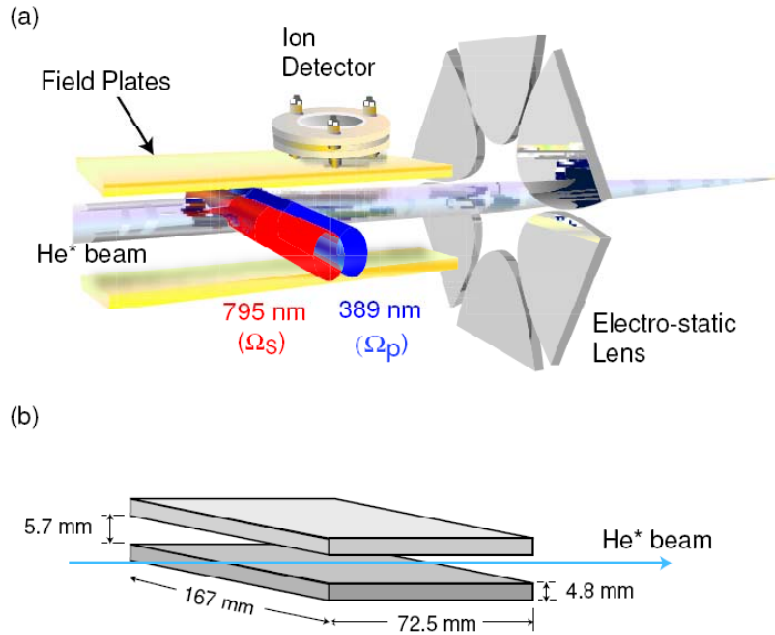
Figure 2.4: Interaction region : (a) configuration of atomic beam, laser beams, field plates and electrostatic lens (b) dimension of field plates [25]

coated for 389 nm, 796 nm and 1083 nm. Thus our laser beams used for the STIRAP excitation process and the detection process can enter the chamber perpendicularly to the atomic beam with less than 1% reflection loss. A few 2-3/4" flanges with BNC feedthroughs, with 0.094 inch diameter pins on the vacuum side, are mounted on the chamber. The voltages for field plates and ion detector are supplied by single-strand Kapton wires (from MDC, diameter: 0.61 mm) and push-on connectors connected to the pins on the feedthroughs.

2.3.1 Ion Detector

The ion detector for ionized Rydberg atom detection is placed in the interaction chamber. It sits close to the downstream edge of the upper field plate supported by insulated screws
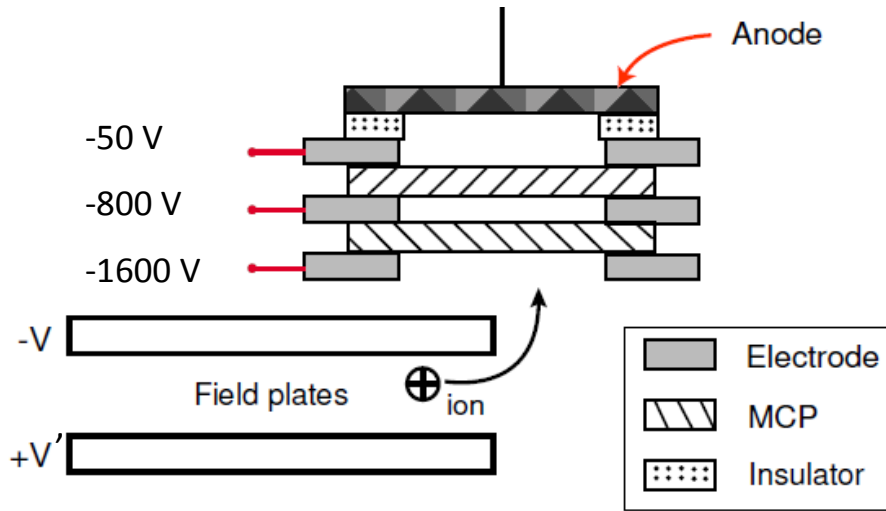
Figure 2.5: Ion detector schematic

to monitor the ionized Rydberg atoms produced during the experiment. The ion detector includes two microchannel plates (MCP) in the Chevron configuration as shown in Figure 2.5.

The microchannel plate consists of thousands of very thin, tiny conductive glass capillaries (microchannels) fused together and sliced into a thin plate. Each microchannel is a continuous dynode electron multiplier, in which the multiplication takes place under the presence of a strong electric field. A particle or photon that enters one of the channels through a small orifice is guaranteed to hit the wall of the channel due to the channel being at an angle to the plate. The incident particle frees an electron from the channel wall. Then, with an electron-accelerating potential difference applied across the length of the channel, the initial electron strikes the adjacent wall, freeing several electrons via "secondary emission". These electrons will be accelerated along the channel until they in turn strike the channel surface, giving rise to more electrons. Eventually this cascade process amplifies the

original signal by several orders of magnitude depending on the electric field strength and the geometry of the microchannel plate. There is a nice review article of MCPs by Wiza [48].

The MCPs in use were purchased from Burle Electro-Optics. The Channel diameters are 10 microns with a center to center spacing of 12 microns. They have a bias angle of $12°$ and a length to diameter ratio of 40:1. The gain of the MCPs is about 10^3 at 750 V bias voltage and 2×10^3 at 800 V. As shown on Figure 2.5, an acceleration voltage of -1600 V attracts ions created from Rydberg atoms to the first MCP, where they are amplified twice (total gain about 2×10^6), then a metal anode after the second MCP collects the electrons. The resulting current is converted to voltage signal that can be observed with an oscilloscope if there is any Rydberg production during scanning the electric field or the red light frequency.

2.4   Detection Chamber

2.4.1   Phosphor Screen Detector

The basic principle of our MCP/Phosphor Imaging Detectors is a conversion of initial radiation into an "electron image", which is amplified by microchannel plates, then converted to a visible image registered by a CCD camera. Our metastable helium atoms incident on the MCP produce an electron shower due to their high internal energy (19.8eV). Charged particles and uv photons also contribute. The electrons cause light emission from the phosphor screen in the visible range, so a real image of the atomic beam distribution can be monitored by a CCD camera outside the vacuum system through a flanged viewport.

Our phosphor screen (Lexel Imaging System) consists of a glass substrate coated with Indium Tin Oxide (ITO), covered by P43 phosphor. The thin ITO layer provides the conduc-
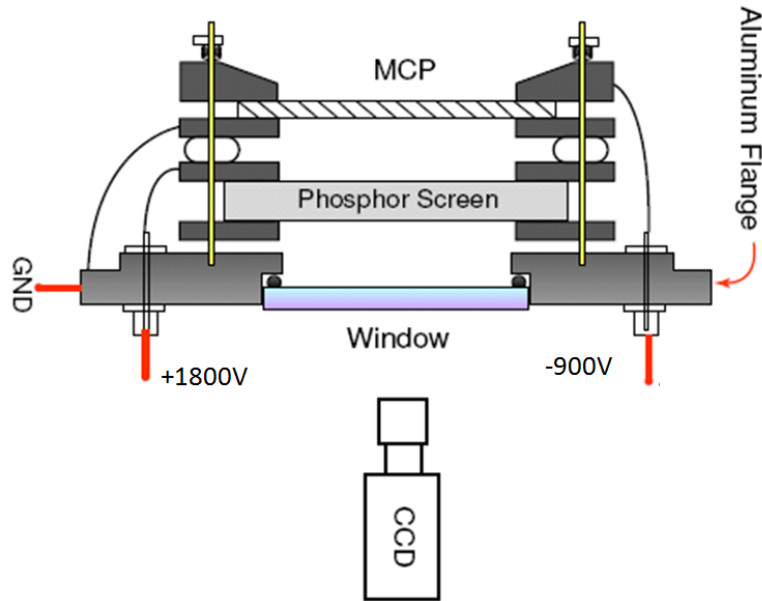
Figure 2.6: MCP/Phosphor screen detector used to take the atomic beam image

tive base needed to minimize the electrostatic effects of charged particles. An extra layer of aluminum is deposited in a ring on the outer diameter of the phosphor screens, to help in the reduction of charge build-up and to allow for electrical contact to the phosphor screen using optionally available metal contact rings. The emitted light wavelength from P43 phosphor is from yellow to green, well in the visible region, with peak typically at 545 nm.

The MCP phosphor screen assembly is mounted at the end of the vacuum system facing the source. As shown in Figure 2.6, the front of the MCP is held at about -800 to -900V and the back side is grounded outside the vacuum system. Then a positive voltage of about +1800V is supplied to the front of the phosphor screen to accelerate the electrons and drain them off after fluorescence. The CCD camera sits a few centimeters from the phosphor screen and the images are sent to the computer via a Winnov video card so that we can monitor

the atomic distribution and take snapshots if necessary.

The drawback of the MCP/Phosphor screen detector is that its sensitivity is not very linear or uniform. It tends to gradually lose efficiency over time after exposure. So quantitative measurements cannot be based on the brightness of image. Our phosphor screen has a decay time of about 1 ms, which in some cases might be an issue. However, this detector is a very important tool for use in aligning the atomic beam and also the laser beams. From the images of the detector, we can easily tell how good the alignments are and if the lasers are frequency locked or not.

2.4.2   Stainless Steel Detector

As we discussed above, the MCP/Phosphor screen detector is not a good candidate to do quantitative measurements. Instead, we use the Stainless Steel detector. Figure 2.7 shows a schematic diagram. It consists of an assembly of a metal front plate with a small aperture in it and a stainless steel back plate. Metastable helium atoms passing through the aperture in the front plate hit the back stainless steel plate and release their high internal energy (19.8 eV). On the other hand, the work function of stainless steel is only about $4.7 - 5.6$ eV, so electrons are liberated. Since the front of the MCP plates sits at a comparatively positive potential, the electrons are drawn towards the first MCP and beyond that to the second MCP, inducing a current to the anode after being amplified twice. The two-plate MCP assembly is exactly the same as the one on the ion detector, called the Chevron configuration. It is known that the efficiency for the liberation of electrons from the stainless steel detector when a metastable atom hits it is 70% [49]. Then the current signal from the anode is proportional to the He* flux integrated over the aperture. To know the exact number of He* atoms, we just need to know the gain on the MCP or we can use a counter to count the number of

29

pulses.
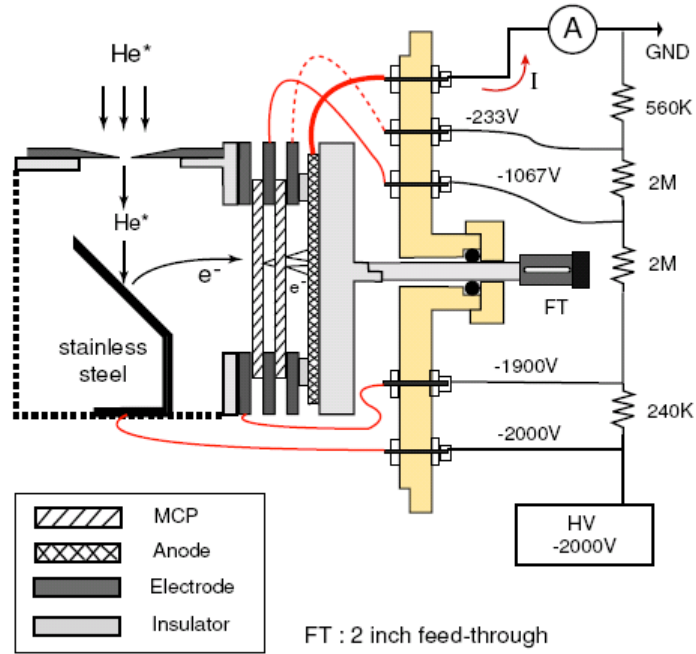
Figure 2.7: Schematic of the stainless steel detector

The complete detector is mounted on a Huntington Mechanical Laboratories, Inc. 2-inch linear motion feedthrough and attached to one of the side flanges on the 6-way cross, so that it can move horizontally in the direction perpendicular to the atomic beam. We can retract the SSD detector all the way out to look at the entire image on the phosphor screen, or we can scan the SSD position to get quantitative measurements of the horizontal distribution of the atomic beam. The slit in front of the SSD is about 2 mm for the STIRAP efficiency measurements, for which we fix the position of the SSD detector and compare the optically detected metastable He* atom flux with and without STIRAP beams, as will be explained later in Section 5.2.

Chapter 3

Laser Systems

3.1 Introduction

To excite helium atoms from the 2^3S_1 metastable state to higher lying Rydberg states, we require two different laser wavelengths, one at $\lambda = 389$ nm which we call the blue light and the second at $\lambda = 770 \sim 837$ nm which we call the red light. We use two independent Titanium-doped Sapphire (Ti:Sapphire) laser systems, the Schwartz Electro-Optics (SEO) Ti:Sapphire and the TekhnoScan Ti:Sapphire laser (Model TIS-SF-07e). Both are pumped by diode-pumped, frequency-doubled $Nd:YVO_4$ lasers (Coherent Model Verdi V10). The SEO Ti:Sapphire laser outputs 778 nm light, which after passing through a frequency doubling cavity (Coherent Model MBD 200), yields the 389 nm blue light. The red light is directly from the Tekhnoscan Ti:Sapphire laser, whose wavelength is tunable over a wide range so that we can excite to different Rydberg states. To stabilize the laser frequencies, three different locking techniques are used. First, both Ti:Sapphires are locked to their own reference Fabry-Perot cavities using the Pound-Drever-Hall (PDH) technique [50][51]. Then to stabilize the frequency doubling cavity, the Hänsch-Couillaud (HC) technique [52] is employed. Finally,

to get rid of long-term drifts, the 389 nm light is locked with the Saturation Absorption Spectroscopy (SAS) [53][54] and the feedback is sent to the PDH cavity. In addition, for the STIRAP efficiency measurements, a laser-diode-seeded fiber amplifier system at 1083 nm is used to generate a bichromatic force to deflect the remaining metastable atoms out of the main atomic beam.

3.2 Blue Light System

The optical scheme of the blue laser system is shown in Figure 3.1. The Verdi V10 laser, used to pump the SEO Ti:Sapphire, outputs a maximum power of 10.5 W at 532 nm. But as the diodes get older and older, more diode current is needed to produce the same 532 nm power. When the diode current exceeds a preset upper limit, the Verdi starts beeping and finally turns itself off. For this reason, we maintain the Verdi at 9 W to keep the diode current a little away from the upper limit. This provides 2.3 W of single longitudinal mode TEM_{00} light out from the SEO Ti:Sapphire at 777.951 nm.

Our SEO Ti:Sapphire laser is set in a ring configuration to avoid the spatial hole burning effect, and an optical diode is placed in the cavity to enforce uni-directional operation. The "bowtie" lasing cavity consists of two curved mirrors and two flat mirrors. The lens L_1 before the input coupler is used to focus the pump light into the Ti:Sapphire crystal and the half-wave plate is used to make sure the pump light polarization is aligned with the Ti:Sapphire crystal optical axis. Since the Ti:Sapphire gain curve is very broad and we need to be able to tune the output and narrow its linewidth, two mode selective elements are used, namely a birefringent filter (BF) and an etalon (E). The etalon provides a relatively small range of tuning, ~ 500 MHz, $\sim 10^{-3}$ nm, with central wavelength at about 778 nm. If a larger tuning range is needed, we operate the birefringent filter. For typical power optimization,

the two flat mirrors in the cavity (the one with the PZT and the output mirror) are adjusted. When the Ti:sapphire laser is well aligned, the output beam is in the TEM_{00} mode and has a divergence on the order of 1 mrad.

The Ti:Sapphire laser beam is tramsmitted through an optical Faraday Isolator (OI) to prevent reflections back into the laser cavity. It is then split into three beams by a glass plate. The transmitted beam (about 80% of the light) goes to the frequency doubling cavity for blue light production. The beam reflected from the front surface of the glass plate goes through a half-wave plate (HWP2) to a Fabry-Perot cavity for Pound-Drever-Hall (PDH) locking, and the one reflected from the glass plate back surface goes in part to a reference cavity for mode monitoring and the remainder is coupled into a fiber and sent to the wavemeter.

The frequency doubling cavity is kept on resonance by the Hänsch-Couillaud (HC) locking technique. After the frequency doubling cavity, the blue light is sent through a single mode fiber to our interaction chamber for the experiment. Part of the blue light is split off the main beam at the PBS for Doppler-free saturation spectroscopy which provides a good atomic reference frequency to which the PDH cavity is locked.

In the following sections, I will describe the different locking techniques in more detail.

3.2.1 Coherent MBD and Hänsch-Couillaud Locking

The second harmonic power $P_{2\omega}$ generated by a single pass through a nonlinear crystal is given by $\gamma_{SHG}P_\omega^2$, where γ_{SHG} is a combination of the crystal's properties and the fundamental beam parameter and P_ω is the fundamental power. With γ_{SHG} on the order of 10^{-4} W^{-1}, not enough power is provided for our STIRAP experiment. To achieve higher second harmonic power, a significantly higher fundamental power is needed. One way to increase the available fundamental power is to use an external resonant enhancement cavity.

389 nm for Exp.

Optical Fiber

SEO - Ti:sapph.

HWP1 L1   TC

Verdi V10

BF

E   OD

PZT1

C.L

C.L

O.I

O.I

PDH stabilization
Electronics

PD1

PD2   PZT2

F-P

PBS   EOM   HWP2

GP

He-cell

SAS stabilization
Electronics

F-P

GP   F

PD4

MBD-E200HV
Controller/HC lock

To wavemeter

BS

PBS

HWP4

Coherent MBD-200
Resonant Frequency
Doubling Unit

L2   HWP3
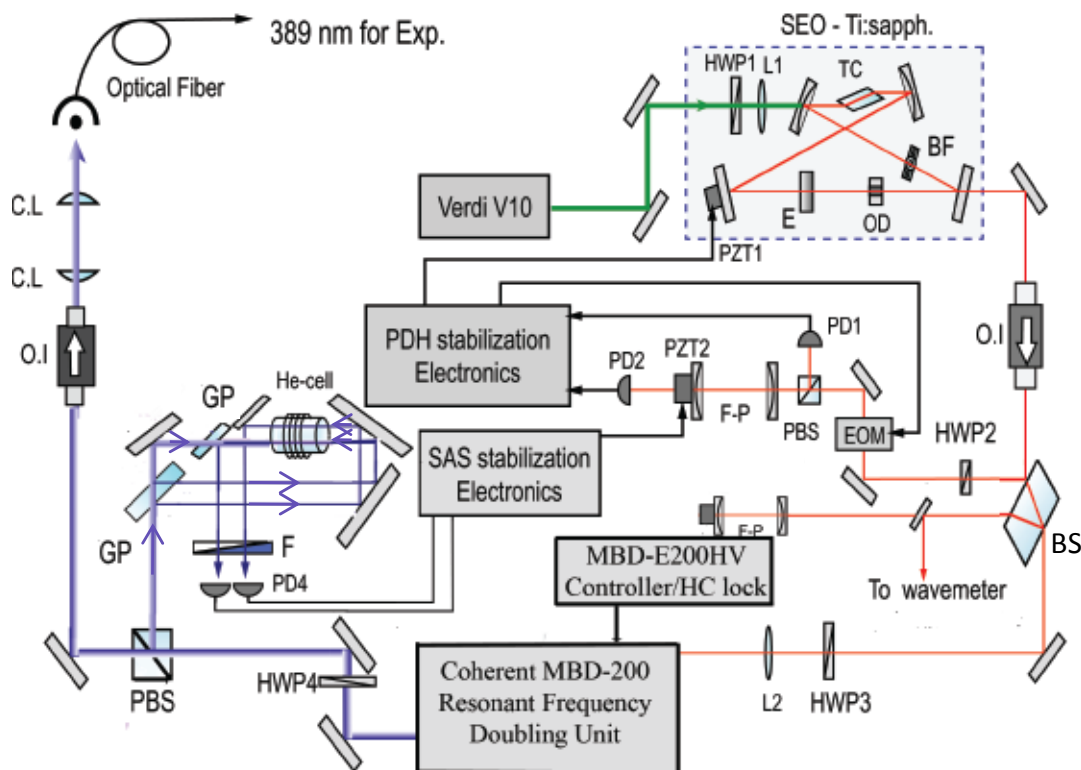
CL : Cylindrical lens   O.I : Optical Isolator   BS : Beam splitter   F : Density Filter
PBS : Polarization beam splitter   GP : Glass plate   PZT : Piezo-electric transducer
PD : Photo diode detector   F-P : Fabry-Perot cavity   HWP : Half-wave plate
OD : Optical diode   TC : Ti-sapphire crystal   BF : Birefringent filter
EOM : Electro-optic modulator   SAS : Saturation absorption spectroscopy
PDH : Pound-Drever-Hall   H-C : Hansch-Couillaud   L : Lens   E : Etalon

Figure 3.1: Optical scheme of the blue laser system

The Coherent MBD-200 is a commercially purchased frequency doubling system, which was used to replace our previous homemade frequency doubling cavity [25]. It came with a doubler head containing a resonant cavity and an electronic unit for system monitoring and control. It has been engineered to be very efficient and stable against normal environmental fluctuations. This system doubles the Ti:Sapphire laser frequency and gives the desired frequency of blue light for the $2^3S_1 \rightarrow 3^2P_2$ transition.

The optical setup of the doubler head is shown in Figure 3.2. It is a well-sealed system which ensures minimal cleaning. The pump laser goes through an input window which is anti-reflection coated. After the input window, the pump light passes a half-wave plate, mode matching lens, and two steering mirrors before entering into the frequency doubling cavity. The half-wave plate is used to set the polarization of the incoming beam precisely and the lens is used to match the mode from the pump laser into the doubling cavity. The two highly reflecting mirrors allow the input beam to be steered accurately into the doubling cavity, and their adjusting mounts are accessible from outside the cavity housing. Leaving the doubling cavity, the UV light passes through the output window, which is highly transmitting at the doubled frequency but is highly reflecting at the fundamental light wavelength, thereby acting as a filter to remove unwanted radiation at the fundamental laser wavelength.

Inside the doubling cavity, there are two flat mirrors M1, M2 and two curved focussing mirrors M3 and M4, aligned in a ring configuration. M2 is mounted on a piezoelectric transducer for cavity scan or locking feedback. A nonlinear Lithium Triborate (LBO) crystal, whose dimensions are 4 mm by 3 mm by 12 mm, is positioned at the intracavity focus, increasing the fundamental intensity to provide efficient nonlinear conversion to the second harmonic. The crystal can be moved both horizontally and vertically to allow us to access the best path through it and to avoid damaged sites, and there is an angle adjustment used to set the phase matching angle. A heater is used to temperature-control the crystal mount,
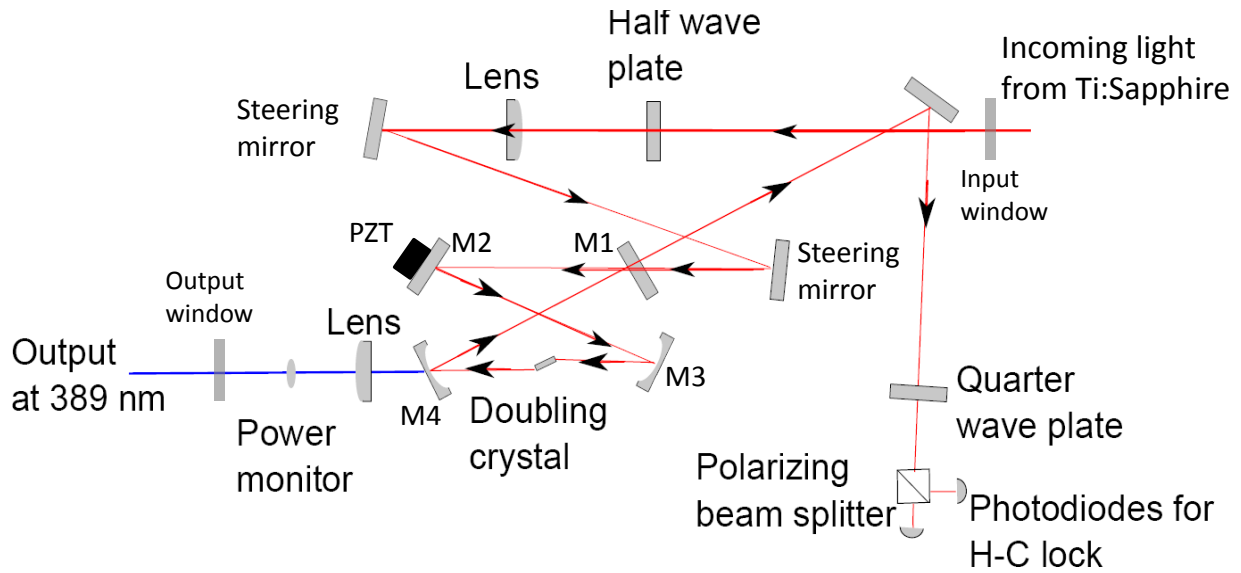
Figure 3.2: The optical path through the Coherent MBD doubling cavity

which is active as long as the MBD controller is switched on and connected to the MBD unit.

To keep the cavity on resonance, a feedback signal is needed to lock the cavity. The technique used for the MBD locking was first developed by Hänsch and Couillaud based on the polarization spectroscopy [52], which is commonly referred to as Hänsch-Couillaud (HC) method. A brief discussion of this technique follows.

Since the efficiency of the nonlinear crystal is highly polarization dependent, and only the horizontally polarized light (along the optical axis of the crystal) participates in the frequency doubling process, any vertically polarized light is simply reflected back by the input coupler. To ensure a high efficiency of the frequency doubling cavity, the polarization of the incident light is set very close to the horizontal. So now if the polarization of the incident beam of the cavity forms a small angle to the horizontal direction, we should consider the total reflected beam from the cavity as the coherent sum of the vertically polarized beam and the reflected

horizontal component. The horizontal polarization sees a low-loss cavity and the reflected beam experiences a frequency dependent phase shift. If the cavity is on resonance, there is no reflection of the horizontally polarized component, thus the total reflected beam is vertically linearly polarized. However, if the cavity is slightly shorter (longer), the reflected light in the horizontal polarization will experience a positive (negative) phase shift compared to the vertical component directly reflected by the input coupler. So the total reflected beam ends up elliptically polarized, where the handedness of the ellipticity depends on whether the cavity is too long or too short.

A polarization sensitive analyzer assembly is used to extract the cavity length information. A quarter-wave plate is set to create circularly polarized light when the cavity is on resonance. In this condition, after passing through a polarizing beam splitter, the two photodetectors sampling the split beams will see the same light intensities. But for an elliptically polarized light, the relative intensity on the two photodetectors will not be equal and their difference will be given by

$$I_1 - I_2 = 2I \cos\theta \sin\theta \frac{T_1 R \sin\delta}{(1-R)^2 + 4R\sin^2(\delta/2)} \tag{3.1}$$

where I is the intensity of the incident beam, I_1 and I_2 are the intensities measured by the two photodiodes (PD) independently, R (< 1) is the effective loss of the cavity and T_1 is the transmissivity of the input coupler [52]. This signal tells us in which direction the cavity has moved and serves as the error signal.

The electronics used for feedback is contained in the control unit. The offset adjust knob on the front panel is used to adjust the DC offset on the HC error signal to peak the second harmonic output. A switch is used to switch between the scanning mode and locking mode of the cavity. The error signal is adjusted to be symmetric and $0.5 \sim 1$ Volts peak-to-peak
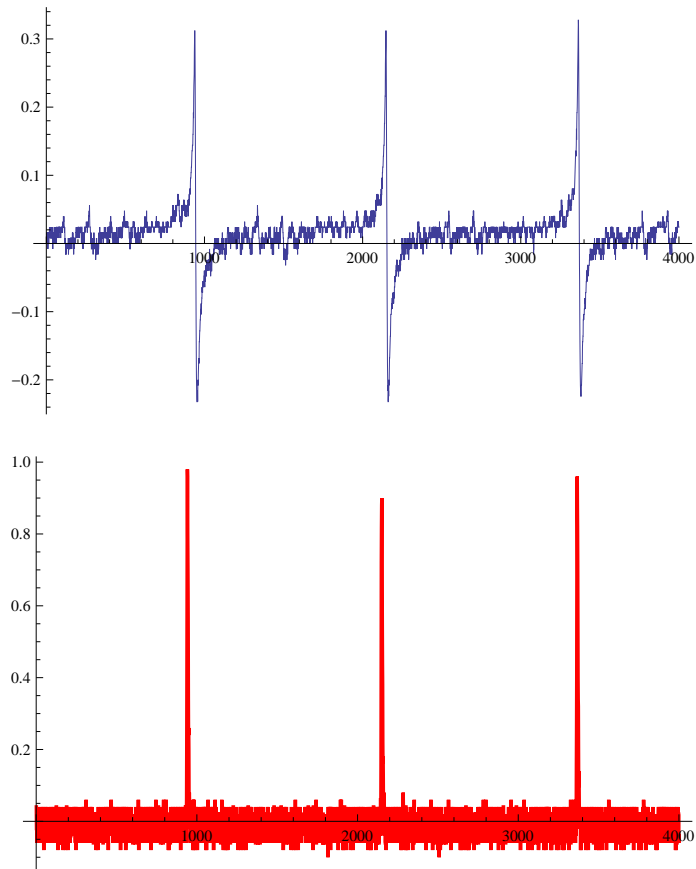
Figure 3.3: The top is the error signal: a trace of the signal after the photodiode subtraction. The lower graph is the power monitor signal [55].

by changing both the half wave plate and quarter wave plate in the MBD-200 box. Once the error signal appears as in Figure (3.3), the locking switch is ready to be turned on. Locking the cavity increases the second harmonic power from about ∼1.5 mW passive transmission to near 500 mW when being pumped with ∼1.6 Watts from the Ti:Sapphire laser. A small amount of the output second harmonic light is directed to a photodiode by the beam splitter. The power at the photodiode can be monitored at the BNC connection on the rear control panel (see Figure 3.3). When the cavity is in the scan mode, this allows optimization of the signal in the final alignment and when the cavity is locked, the whole level of this signal

38

jumps up to the original scanning peak height, which serves as a good reference signal.

3.2.2 Pound-Drever-Hall Locking Technique

The Pound-Drever-Hall (PDH) locking technique was firstly invented by Pound [50] to lock microwave oscillators to a stable reference cavity and later transferred to the optical regime by Drever and Hall [51]. The idea behind the PDH method is simple in principle: A laser's frequency is measured with a Fabry-Perot cavity, and this measurement is fed back to the laser to suppress frequency fluctuations. The measurement is made using a form of nulled lock-in detection, which decouples the frequency measurement from the laser's intensity [56].

For a Fabry-Perot cavity, the intensity of the reflected (or transmitted) beam is symmetric about resonance. If the laser frequency drifts out of resonance, we can't tell just by looking at the reflected intensity whether the frequency needs to be increased or decreased to bring it back onto resonance. The derivative of the reflected intensity, which contains the "phase" information, however, is antisymmetric about resonance. If we were to measure this derivative, we would have an error signal that we can use to lock the laser. Fortunately, this is not too hard to do; we can just vary the frequency a little bit and see how the reflected beam responds. The purpose of the PDH method is to do just this.

As shown in figure 3.5, the PDH scheme employs a electro-optic modulator (EOM), which is driven by a RF oscillator at frequency Ω (= 64 MHz) via a RF (radio frequency) amplifier, to modulate the phase of the central carrier frequency ω_c. The modulated beam is sent to a Fabry-Perot cavity. Two photodiodes are used to measure transmitted light and the reflected light from the cavity. The reflected beam is picked off with an optical isolator (a polarizing beam splitter and a quarter-wave plate makes a good isolator) and sent to a photodiode (PD1). The output signal from the photodiode passes through an RF amplifier

39

(Mini-Circuits ZFL500LN) and is compared in frequency with the same RF oscillator used to modulate the EOM via a mixer (Mini-circuits ZEM2B). We can think of a mixer as a device whose output is the product of its inputs, so this output will contain signals at both very low frequency and twice the modulation frequency. It is the low frequency signal that we are interested in, since that will tell us the phase of the reflected intensity. A low-pass filter on the output of the mixer isolates this low frequency signal, which then goes through a pre-amplifier and some PID control and is fed back to the PZT in the Ti:Sapphire laser cavity.

Let's take a closer look at how it really works. First, the EOM modulates the incident light at carrier frequency with RF frequency Ω

$$F_\omega = E_0 e^{i(\omega_c t + \beta \sin \Omega t)} \tag{3.2}$$

which can be expanded in a Bessel function series

$$F_{inc} = E_0 e^{i\omega_c t} \sum_{n=-\infty}^{\infty} J_n(\beta) e^{in\Omega t} \tag{3.3}$$

$$\approx E_0 [J_0(\beta) e^{i(\omega_c)t} + J_1(\beta) e^{i(\omega_c + \Omega)t} - J_1(\beta) e^{i(\omega_c - \Omega)t}] \tag{3.4}$$

Here β is known as the modulation depth, and $J_n(\beta)$ are the Bessel functions. For $\beta \ll 1$, all the terms except n$= -1$, 0, 1 can be neglected. Thus there are actually three different beams incident on the cavity: a carrier, with frequency ω_c and two sidebands with frequencies $\omega_c \pm \Omega$, which you can see in Figure 3.4. Interfering the sidebands with the reflected beam will produce a beat pattern at the modulation frequency, from which the

phase can be determined.

$$F_{ref} = E_0[F(\omega_c)J_0(\beta)e^{i\omega_c t} + F(\omega_c + \Omega)J_1(\beta)e^{i(\omega_c + \Omega)t} - F(\omega_c - \Omega)J_{-1}(\beta)e^{i(\omega_c - \Omega)t}] \quad (3.5)$$

where $F(\omega_c)$ is the reflection coefficient for a Fabry-Perot cavity with lossy mirrors at frequency ω_c. Instead of the amplitude, the intensity is measured by a photodiode, which is given by $P_{ref} = |E_{ref}|^2$, and after some algebra [56]

$$\begin{aligned} P_{ref} = {} & P_c|F(\omega_c)|^2 + P_s[|F(\omega_c + \Omega)|^2 + |F(\omega_c - \Omega)|^2] \\ & + 2\sqrt{P_c P_s}Re[F(\omega_c)F^*(\omega_c + \Omega) - F^*(\omega_c)F(\omega_c - \Omega)]\cos(\Omega t) \\ & + Im[F(\omega_c)F^*(\omega_c + \Omega) - F^*(\omega_c)F(\omega_c - \Omega)]\sin(\Omega t) \\ & + (2\Omega \; terms) \end{aligned} \quad (3.6)$$

The Ω term in (3.6) comes from the interference between the carrier and the sidebands and thus contains the phase information. Depending on the modulation frequency Ω, either the sine or the cosine term always vanishes [56], and the remaining one is used for the error signal. Then the phase term is extracted by a mixer, a phase shifter and a low-pass filter. The mixer multiplies its two inputs and only when the two inputs have the same frequency components, it produces some DC (very low frequency) signal. In our case, the DC signal only comes from the Ω term in (3.6) and this can be easily isolated from the other high frequency terms with a low-pass filter. The phase shifter is necessary to compensate for possible phase delay due to different signal paths.

The error signal as shown in Figure 3.4 is fed to a low-noise amplifier, and the gain and the cut-off frequency are optimized. After choosing the correct parity and DC offset, the signal is separately fed to a two-stage integrator (f3dB = 2 Hz and f3dB = 0.5 Hz)

41
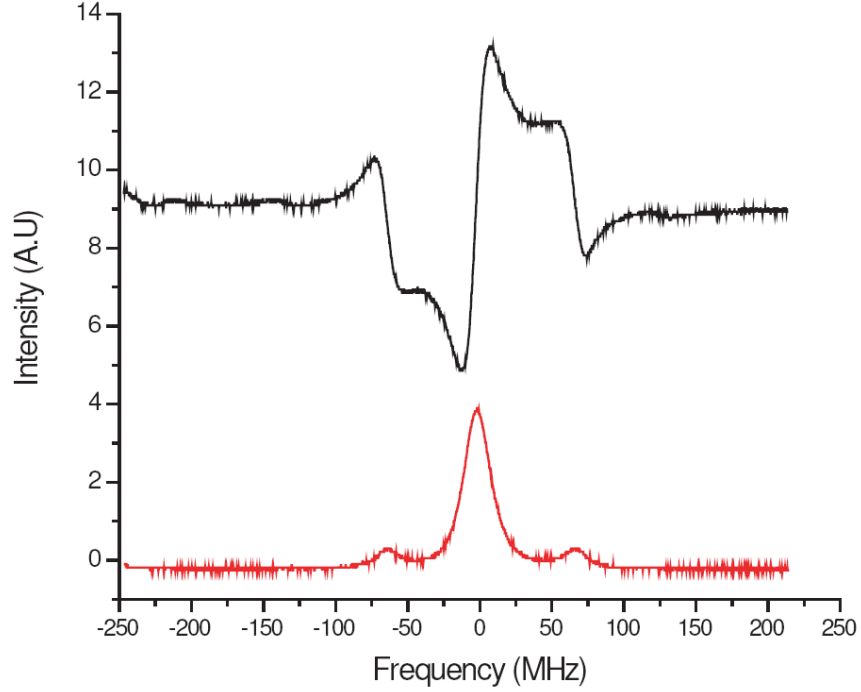
Figure 3.4: Pound-Drever-Hall error signal (top) and transmission signal (bottom) [25]

and a proportional loop whose outputs are subsequently recombined in a summing junction. Passing through a high voltage amplifier, the PDH error signal is applied to PZT1 (in Figure 3.1 and 3.5) inside the Ti:Sapphire laser cavity.

The detailed procedures for locking the Ti:Sapphire to the PDH cavity are the following: First, stop scanning the Fabry-Perot cavity by switching off the function generater (FG) in the summing box Σ_2 (Figure 3.5). Second, adjust the DC offset in summing box Σ_2 so that the transmission of PD2 rises up close to the original height of the transmission peaks on the scope indicating that the cavity is close to resonance. Third, switch on S1 and S2, then adjust simultaneously the gain of the two integration stages to smooth the locking signal and minimize the deviation of the locking signal from the resonance peak (zero on the error signal). Sometimes, if the transmission signal jumps up and down, it might indicate mode
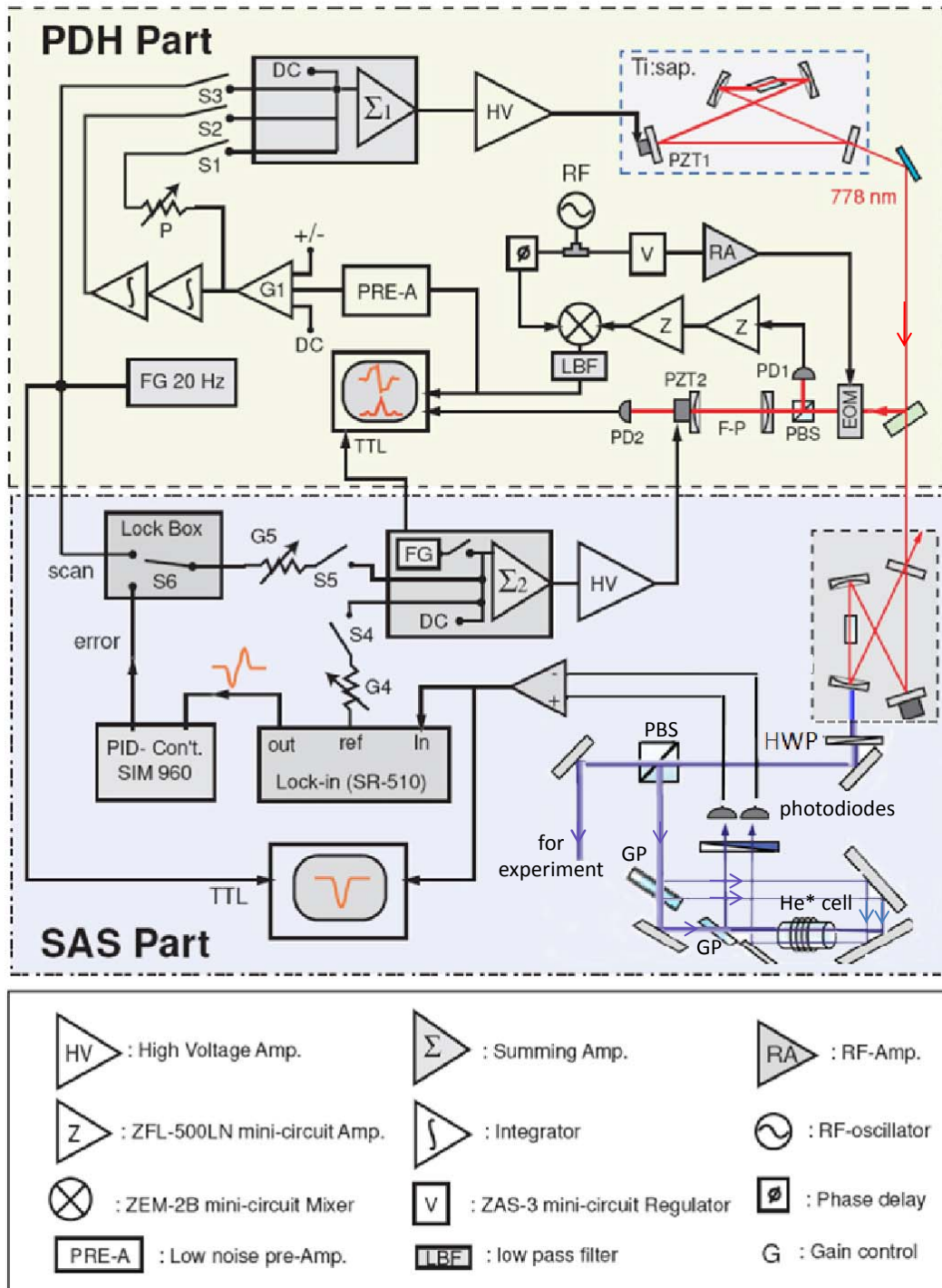
Figure 3.5: Stabilization electronics for the blue laser system [25][44]

hopping in the Ti:Sapphire laser, which can be confirmed by looking at the transmission signal of the reference Fabry-Perot cavity. To get rid of the extra mode, we might need to turn off the PDH lock, and adjust the etalon and the DC offset on the Ti:Sapphire PZT.

3.2.3   Saturation Absorption Spectroscopy

The PDH setup serves to stabilize the Ti:Sapphire laser on a short time scale, but can't compensate for slow frequency drifts due to ambient temperature changes. To keep the blue light on resonance, we need a standard frequency reference which is immune to environmental drift. Since we want to drive the $2^3S_1 \rightarrow 3^3P_2$ transition using blue light, this transition itself is a good reference. Therefore, we use Saturation Absorption Spectroscopy (SAS), which is a commonly used technique for this purpose [53][54], to lock the PDH cavity while using the PDH cavity to lock the Ti:Sapphire laser.

When a weak laser beam passes through a cell filled with a gas of low density, it will be partially absorbed and scattered if the laser frequency is on resonance with a electronic transition. So if we scan the frequency of the laser across the transition, it leads to a dip in the transmission signal. However, because the atoms are moving with different velocities, the dip is Doppler broadened, which makes the width much bigger than the natural linewidth (see Figure 3.6(a)).

For a highly saturated pump beam (with intensity a lot higher than the saturation intensity $I_s = 3.31~mW/cm^2$), due to power broadening, the spectral width of the absorption signal is $\triangle\omega_{sat} = \Gamma(1+s)^{1/2}$, which is determined by the natural width Γ and the saturation parameter $s = I/I_{sat}$, where $I_{sat} = \frac{\pi hc}{3\lambda^3\tau}$ [5] is the specific saturation intensity of the atoms (h: Planck's constant, c: speed of light, τ: atomic lifetime). If there is another weak, counter-propagating beam with the same frequency ω, which equals the atomic resonant
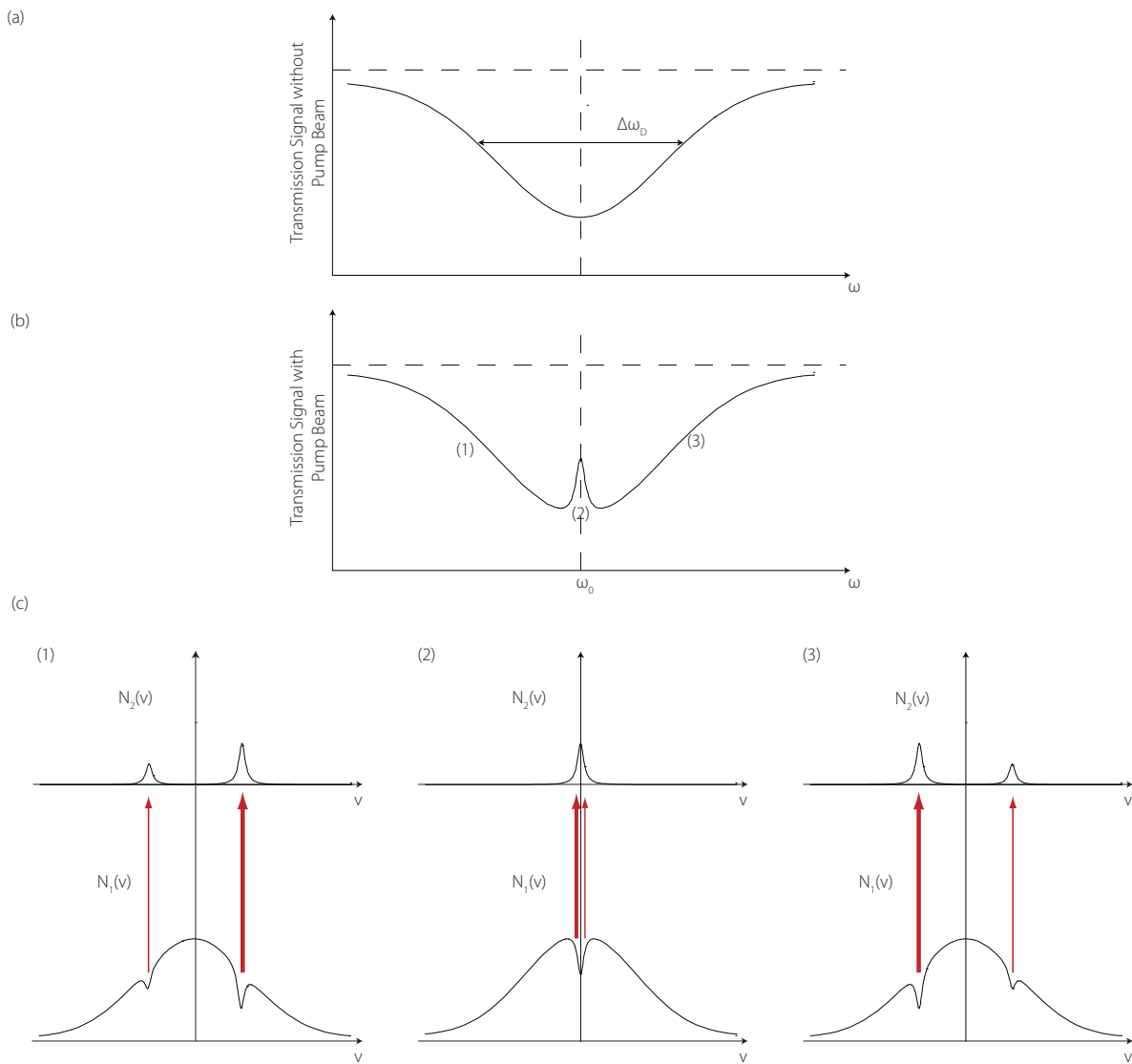
Figure 3.6: (a)The transmission signal of the probe beam is Doppler broadened when the pump beam is not present. (b)The transmission of the the probe beam in the presence of the pump beam. Note here is a small Doppler free signal on top of the broad dip. (c) If the laser is off-resonance, the probe and the pump beams are interacting with different velocity group and the transmission signal is the same as without the pump beam as shown in (1) and (3). The dip occurs only when the laser beam is on resonance and both beams interact with the same velocity group, v=0 as in (2).

frequency ω_0, both beams interact with the same velocity group. Then the saturation of the transition by the strong pump beam results in a reduced absorption (enhanced transmission) of the weak beam, which you can see as a small Doppler-free signal (called "Lamb dip") on top of the broad dip as shown on Figure 3.6 (b). After subtracting the transmission signal with and without the strong pump beam, only the Doppler-free Lamb dip remains, whose width is on the order of the natural linewidth. If the two beams are off-resonance ($\omega \neq \omega_0$), the probe and the pump beams are interacting with different velocity groups and the transmission signal is the same as without the pump beam as shown in Figure 3.6 (1) and (3).

In our setup for the experiment, we have a Helium cell with a discharge driven by an HP3200B oscillator at 57 MHz whose output is amplified by a RF Power Labs Inc model FK 250-10C wideband RF Amplifier to 10W. This RF power is high enough to create He metastables. A small part of the blue light from the frequency doubling cavity is split off by a polarization beam splitter (PBS) for the SAS. And the beam is split again into two weak beams (probe and reference) and one strong counter-propagating beam (pump). The pump beam overlaps with the probe beam, so that the probe beam is weakly absorbed. Transmitted beams of the probe and the reference are collected by two separate photodetectors (in Figure 3.1 and 3.5). Comparing the two signals out of the photodetectors ends up with a Lamb dip on the scope while we scan the laser frequency. Our saturation parameter s ($s = I/I_s$) for the pump beam is about 15 ($I_s = 3.31 \ mW/cm^2$) while for the probe beam and the references it is about 1. The balance of the two photodetector signals is done by adding a variable filter (F) to change the relative intensities of the probe and the reference beam.

The remainder signal after subtraction of the two photodetector signals is sent to a lock-in amplifier (SRS Model 510) and modulated by a 800 Hz reference signal from a function generator (Model 124A EG&G). The mechanism of generating an error signal is the same as
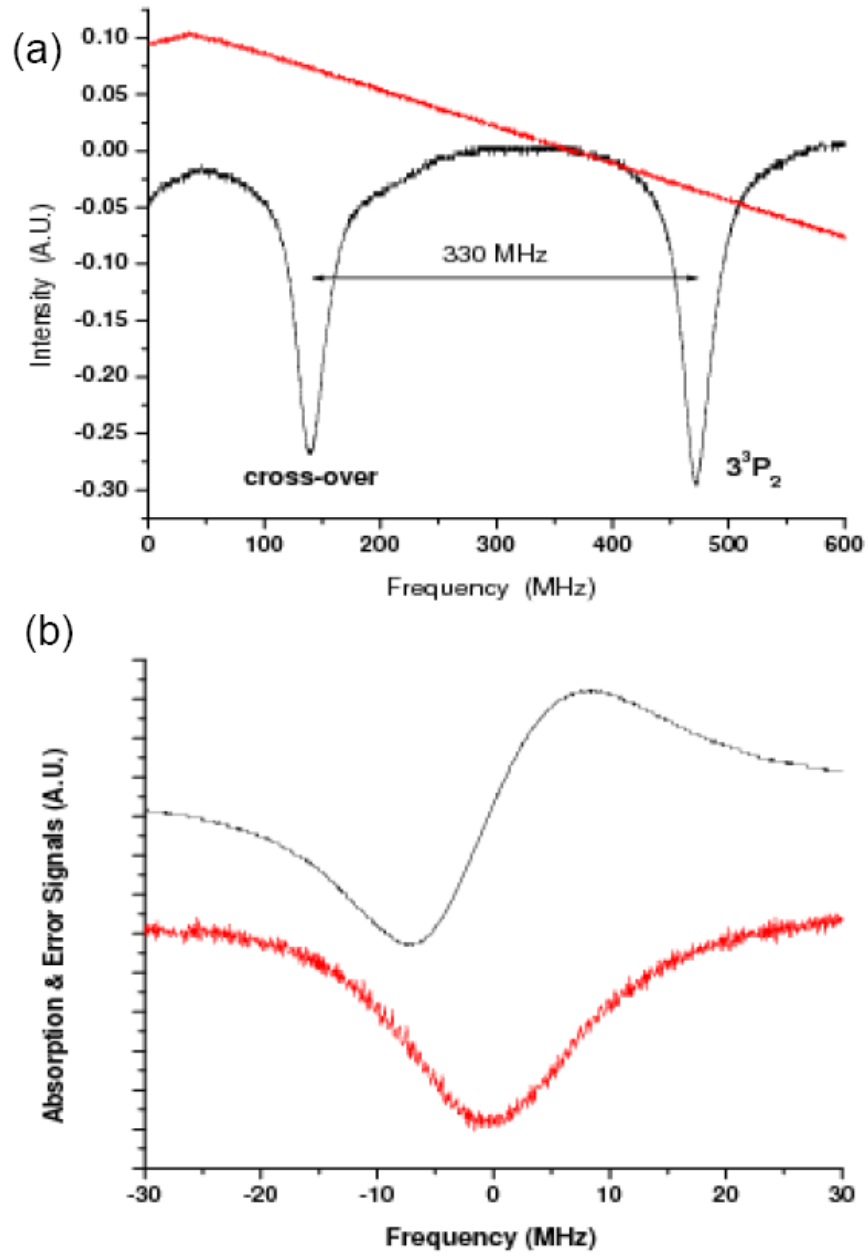
Figure 3.7: SAS signals for: (a) $2^3S_1 \rightarrow 3^3P_2$ transition and crossover between 3^3P_2 and 3^3P_1 (b) $2^3S_1 \rightarrow 3^3P_2$ transition (bottom) and resulting error signal (top) [25]

47

in the PDH locking technique, as explained in the previous section. Through the summing box when the switch S4 is closed, the reference signal also modulates the PDH cavity, thereby modulates the Ti:Sapphire laser as well as the blue light out from the frequency doubling cavity when the Ti:Sapphire laser is locked to the PDH cavity. The SAS absorption and the error signal are shown in Figure 3.7, in which the horizontal axis is converted to frequency with the separation between the real peak and the crossover peak.

In the case of multiple atomic levels, so-called cross-over peaks are observed. These lie exactly halfway between two accessible transitions that have a frequency separation less than the Doppler broadened linewidth $\triangle \omega_D$. Figure 3.7 shows the $2^3S_1 \rightarrow 3^3P_2$ transition and crossover between 3^3P_2 and 3^3P_1. This is caused by the velocity distribution bringing one level to resonance in the probe beam and a different level to resonance in the pump beam at the same time .

To really lock the blue light on atomic resonance, we first need to find the correct SAS absorption peak. In order to do this, we first make sure the wavemeter (Burleigh WA 1500) reads about $777.951 \sim 777.952$ nm and close the Switch S3 to scan the Ti:Sapphire cavity with the function generator at 20 Hz (Figure 3.5). Then with blue light locking on, adjust the DC offset in the summing box Σ_1 until the absorption peak appears as shown in Figure 3.7. Keep tuning the DC offset towards higher wavelength to make sure there are no more peaks at higher wavelength, because the energy level of 3^2P_2 is the lowest among all different J levels. After we find the right peak, we turn off S3 and lock the Ti:Sapphire to the PDH cavity (see Section 3.2.2). The next step is to lock the PDH cavity to the atomic transition. The switch S6 is set to scan and we turn on the switch S5 (Figure 3.5), then we change the DC offset of the summing box Σ_2 until we can see the absorption signal as shown in Figure 3.7(b) again. The size of the absorption signal depends on the gain G5. If G5 is increased, the crossover peak, which is exactly half way between two real transitions ($2^3S_1 \rightarrow 3^2P_2$ and

$2^3S_1 \rightarrow 3^2P_1$), can be seen together with a real peak as shown in Figure 3.7(a), separated by 330 MHz. Afterwards, switch on S4 and turn up G4 a little bit so that we can see the error signal. If G4 and G5 are turned up too much, the PDH transmission and error signal will become very noisy. After everything is set correctly, finally switch S6 from scan to lock, then the laser should be locked.

3.3   Red Light System

The red laser system is much simpler than the blue laser system. It is also based on a Ti:Sapphire laser, the Tekhnoscan Model TIS-SF-07e. In the past, it was pumped by an Argon-Ion laser (Coherent Innova 310) and the output power was around 1 W at a pump power of 10W [25]. But after several years, the best the Argon-Ion laser could produce was around 7 W, and we could only get $500 \sim 600$ mW out. In Oct. 2008, we replaced the Argon-Ion laser with a new Verdi V10 laser, the same model as the one used for pumping the SEO Ti:Sapphire. After careful alignment, we reached an output power of 1.3 W, horizontally polarized and with linewidth < 3 MHz, with 9 W 532 nm pump light. Compared with the SEO Ti:Sapphire which is pumped by the same amount of 532 nm light, the Tekhnoscan has a relatively lower pumping efficiency. This is probably caused by several factors: first, the quality of the Ti: Sapphire crystal is not as good as the one in the SEO laser. Second, as shown in Figure 3.8 [25], the ring geometry is different, as the Tekhnoscan contains more mirrors and more mode-selective components and lastly, the coatings on the components may be inferior.

The laser cavity is comprised of six mirrors, two of which are spherical (M_1 and M_2) used to focus the light onto the Ti:Sapphire crystal and the others are planar. A Faraday rotator together with an out-of-plane mirror (M_5) ensures a unidirectional running wave in
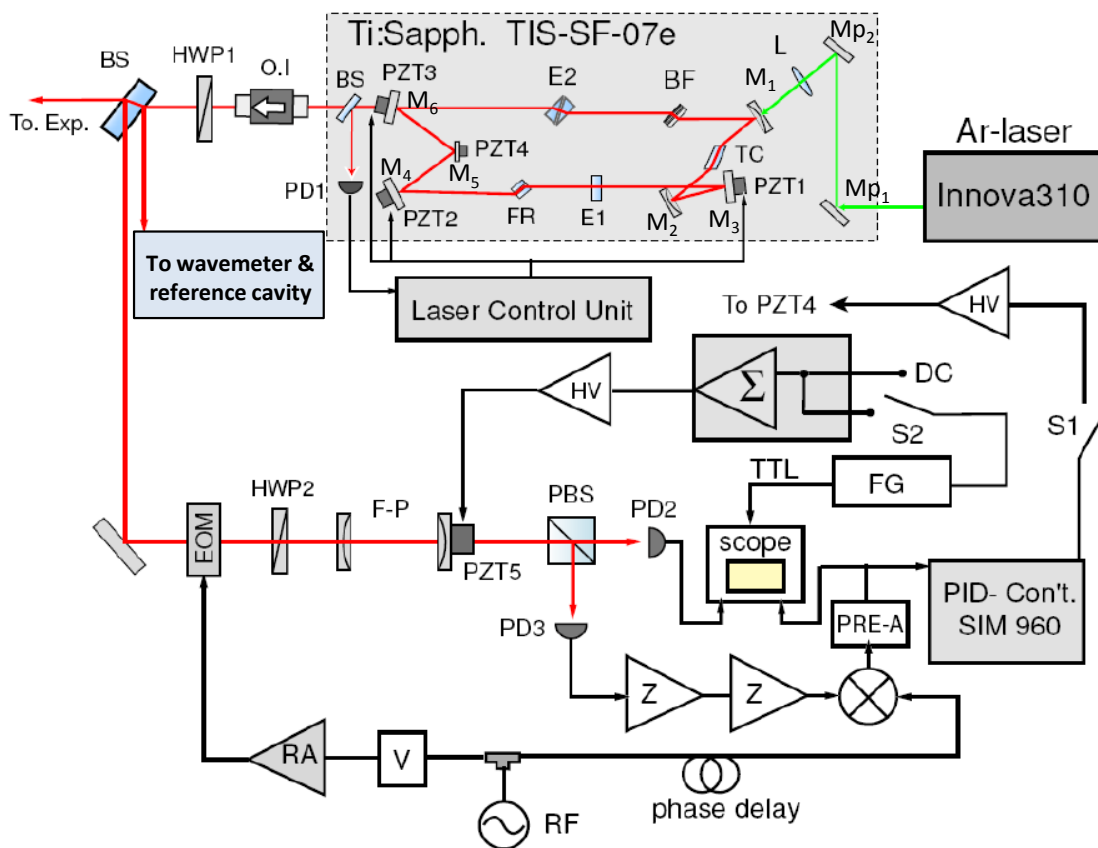
BF : birefringent filter   E1 : thin-etalon   E2: thick-etalon   FR : Faraday-rotator
EOM : Electro-optic modulator   O.I : Optical Isolator   HWP : Half-wave plate
PBS : Polarization beam splitter   BS : Beam splitter   F-P : Fabry-Perot cavity
PZT : Piezo-electric transducer   TC : Ti-sapphire crystal   PD : Photo diode

HV : High Voltage Amp.   Σ : Summing Amp.   V : ZAS-3 mini-circuit Regulator
PRE-A : Low noise pre-Amp.   ⊗ : ZEM-2B mini-circuit Mixer   : RF-oscillator
Z : ZFL-500LN mini-circuit Amp.   FG : Function generator   RA : RF-Amp.
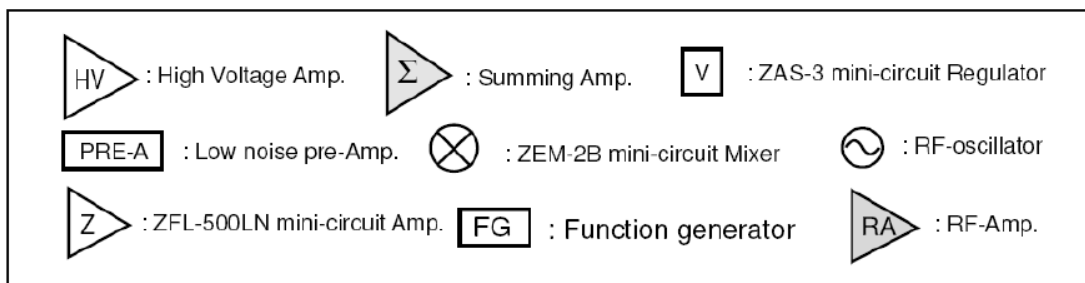
Figure 3.8: Optical scheme of the red laser system

the cavity. For the first alignment from scratch, it is much easier to start in the standing wave mode, with mirror M_4 and M_6 reflecting beams back along their original path. Then we can even take out more elements from the cavity: the birefringent filter, the thin etalon, the Faraday rotator and the thick etalon assembly. Try to get it to lasing and use a fast power meter to peak the laser alignment for maximum power. Next, put the birefringent filter, thick etalon and Faraday rotator back, one at a time in this order. Since the birefringent filter and the thick etalon shift the beam horizontally a lot, the beam passing through them might not hit M_6 anymore. It is better to put a bigger auxiliary mirror there first, otherwise, we will just have to move the M_6 mirror base and redo part of the alignment. After we got a decent amount of light, say higher than 600 mW, in the standing wave mode, we can switch back to the ring configuration by using horizontal and vertical controls of M_4 and M_6 to reflect the fluorescent spot onto M_5, and to reach coincidence. Finally, we can put the thin etalon back in the beam, which should not cause much loss. Always adjust in turn mirrors M_4, M_6 and Mp_2 for maximum power.

One advantage of this Ti:Sapphire laser is that it comes with an electronic control unit. The control unit is able to allow adjustment of the mode selective elements inside the cavity to tune or scan the frequency and also automatically maintain the single frequency generation mode [57].

We can tune the wavelength over a very wide range: $770 \sim 837$ nm, which makes it possible for us to excite helium atoms to all different n states (from $n = 12$ to 30 and higher). This is done with a birefringent (BF) filter, a thin etalon and a thick etalon. The wavelength is coarsely selected with a 3-stage BF filter which consists of three parallel crystalline quartz plates placed at Brewster's angle. Within a given spectral range, the filter provides minimal loss for the radiation since it doesn't change the polarization of the light upon passing through each of the filter plates. For other wavelengths, the losses suffered at each Brewster-angle

surface within the cavity due to the polarization change make these wavelengths fail to reach the lasing threshold. The wavelength of minimum loss can be shifted by modifying the tilt angle of the birefringent filter via a micrometer screw. The thin etalon is made of a 0.5 mm thick uncoated fused silica plate, which allows tuning wavelength radiation within a 207 GHz range that corresponds to the thin etalon free spectral range. A electro-mechanical drive is used for the thin etalon tuning, which can be accessed by the "etalon" knob on the control unit. And an air spaced thick etalon made with two Littrow prisms with thickness of 8 mm has a free spectral range of 18.75 GHz. The spectral position of the thick etalon transmission peak is adjusted with the help of a piezoelectric transducer (PZT). So rotate the "Selector" knob to change the PZT voltage for the setting of wavelength with the 18.75 GHz thick etalon. Furthermore, the optical length of the cavity can be dynamically adjusted by moving three mirrors, mounted on large PZTs, which are controlled by the "resonator" knob on the control unit. This allows smooth tuning of the radiation wavelength within the 5 GHz range. By adding a ramp signal on the PZTs, we can scan the laser frequency smoothly in a range of ~ 5 GHz. The wavelength of the light is monitored by the Burleigh WA-1500 wavemeter. In addition, a small amount of light is split off the main beam and sent to a scanning Fabry-Perot interferometer to make sure the laser runs in the single frequency regime.

Automatic adjustment of the single frequency mode of the laser is done by locking of the thick etalon transmission peak. The way the frequency lock-in system works is pretty similar to the PDH locking: the thick etalon PZT receives a small AC voltage at 1 kHz. This modulation leads to a slight modulation in the output power at the same frequency that is monitored by a photo-detector. (A beam split from the main beam is directed to the photo-detector.) Further on, the photo-detector signal passes through a 1 kHz filter, then gets synchronously detected and fed from an integrator into a high-voltage amplifier, which

drives the PZT of the thick etalon [57].

The out-of-plane mirror (M_5) is attached to a fast PZT, which could be used for external control. So we also set up our PDH locking system to keep it more stable, although the frequency stability of the red light is not as critical as the blue light because we scan the Stark energy level through resonances during the experiment. While most of the beam goes to the experiment, a small amount is sent to a scanning Fabry-Perot interferometer to make sure the laser runs in the single-frequency regime.

3.4   1083 nm Light

The light at $\lambda = 1083.33$ nm used for the $2^3S_1 \rightarrow 2^3P_2$ transition is provided by a Spectra Diode Labs (SDL) model SDL-6702-H1 distributed Bragg reflector (DBR) diode laser. This diode is packaged in an 8 pin TO-3 window mount with a thermistor and a thermoelectric cooler. The temperature of the diode is kept stable at 21.9 ± 0.1^oC by an ILX Lightwave LDT-590 temperature controller and the current of the laser diode is set with a Thorlabs LDC 500 laser diode controller. The dependence of the laser diode wavelength and output power on its current has been examined very carefully in previous theses [58][47][55].

The linewidth of the diode is about 3 MHz, which is larger than the 1.6 MHz natural linewidth of the $2^3S_1 \rightarrow 2^3P_2$ transition. To narrow the linewidth of the diode laser, an extended cavity is used, as seen in Figure 3.9. 30% of the diode output is picked off by a plane beamsplitter and sent to a retro-reflecting mirror, which is mounted on a piezoelectric transducer (PZT). This controlled feedback increases the lifetime of the photons in the cavity and narrows the linewidth to approximately 125 kHz [59]. For shielding against external temperature fluctuation and vibration, the diode and the extended cavity set-up are placed on a 305 mm x 710 mm x 76 mm Aluminum slab and inside a box constructed
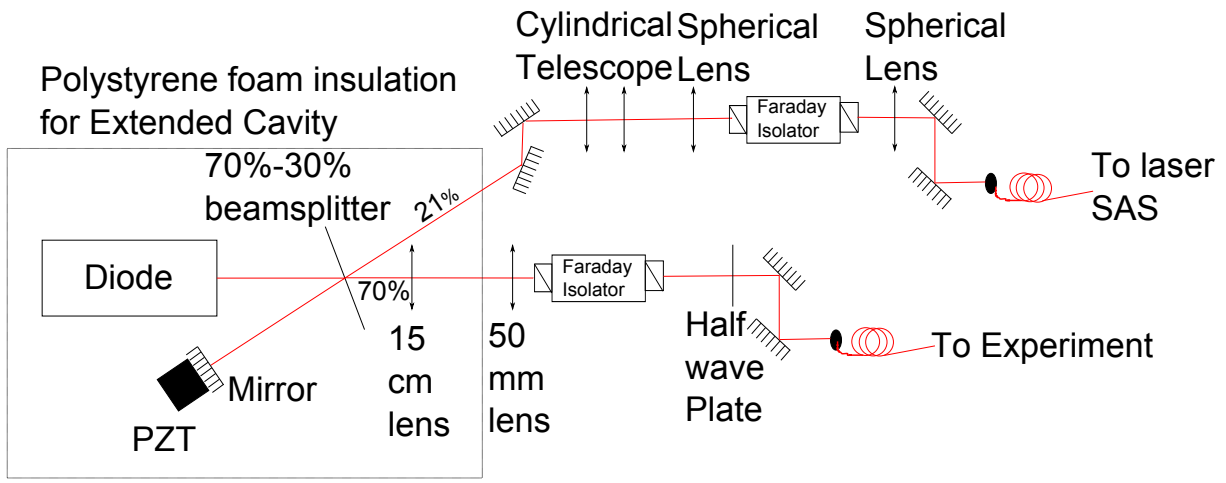
Figure 3.9: Schematic of the diode laser setup [55]

of polystyrene foam insulation. Although there are long-term temperature drifts over the course of a day, the temperature inside the box is stable to better than 0.5 ^{o}C/hr in a short term [55]. In addition to narrowing the bandwidth, the extended cavity also serves as the diode's fine frequency tuning knob.

As a result of the external cavity setup, the diode produces two beams: a main beam (70% of full power) and a leakage beam (21% of the full power). To prevent disruptive feedback to the extended cavity, optical isolators are placed in both beams. After collimation, these beams are launched into single mode optical fibers. The main beam is used for the four frequency setup to feed the Fiber amplifiers and the leakage beam is used for Saturated Absorption Spectroscopy (SAS) to lock the laser frequency to an atomic transition in He.
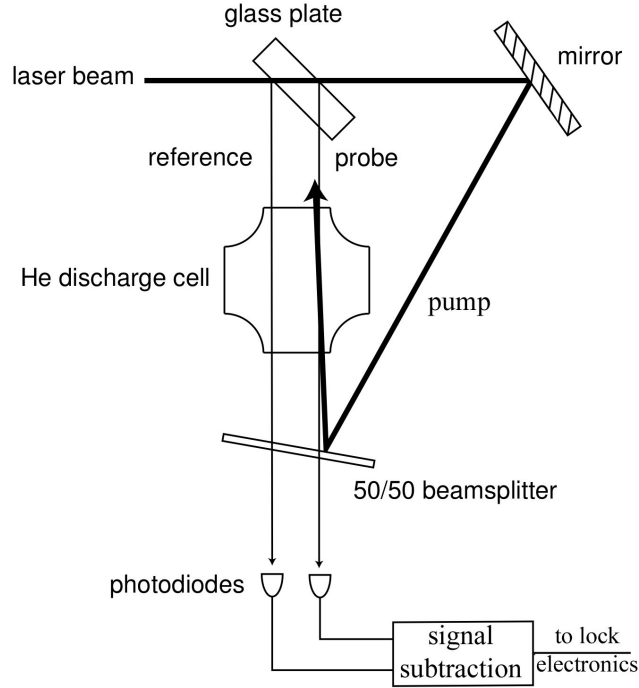
Figure 3.10: Schematic of the SAS setup for the 1083 nm light [55]

3.4.1 Frequency Locking

SAS locking has been described in detail in the blue light section. Figure 3.10 and 3.11 show how it is implemented. A thick glass plate reflecting 4% from each surface is used to produce the probe beam and the reference beam. These two beams are directed through a Helium discharge cell and transmitted through a 50/50 beam splitter and detected on the two photodiodes. The transmitted beam through the thick glass plate is directed to a mirror and then the 50/50 splitter. Its reflection off the beam splitter is directed to counter-propagate against the probe beam. The reference signal is subtracted from the probe signal to obtain a Doppler-free spectrum.

The SAS absorption signal is first amplified with a Stanford Research System (SRS) SR560 low-noise preamplifier and then fed into an EG&G Princeton Applied Research lock-
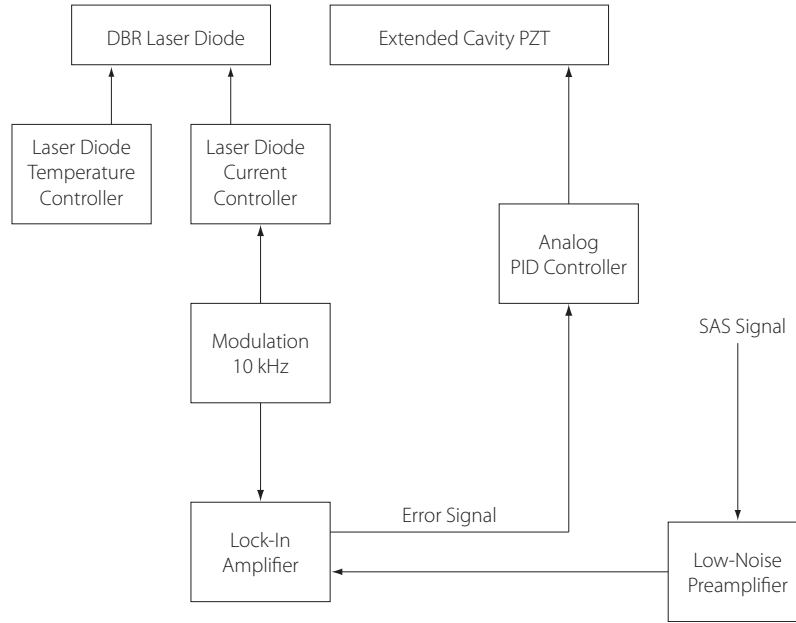
Figure 3.11: Schematic of the SAS locking electronics for the 1083 nm light [47][55]

in amplifier (model 5104). To generate an error signal, a modulation signal must be applied to the laser frequency. This modulation signal also serves as the reference signal for the lock-in amplifier. The 10 kHz reference signal is provided by an SRS DS345 30 MHz synthesized function generator. It modulates the current driving the laser diode and therefore modulates the laser frequency. The error signal is sent to an SRS SIM960 analog proportional-integral-derivative PID controller, whose output goes to a high voltage amplifier and then feeds back to the PZT in the extended cavity to force the laser frequency to remain on the atomic transition.

3.4.2 Bichromatic Light

As the name suggests, bichromatic light consists of light at two frequencies, $\omega_0 \pm \delta$. This is produced by double passing the light from the diode laser through an acousto-optic

56

modulator (AOM) driven at a frequency $\delta/2\pi$ [60], as shown in Figure 3.12. The resulting two beams have the spectral components $(\omega_0, \omega_0 + 2\delta)$ and $(\omega_0 + \delta, \omega_0 - \delta)$ respectively. Both beams are used for bichromatic collimation in the lithography experiment [47][55], but to push the metastable He atoms out of the beam here, we only use the $(\omega_0 + \delta, \omega_0 - \delta)$ beam. Since the bichromatic light setup is in an adjacent laboratory, we pick off the beam we need with a flip mirror and send to our room with a polarization maintaining (PM) fiber. A power of 1 mW exits from the fiber. To make sure that the two frequencies have the same intensity, a mating sleeve and an extra single mode fiber are used to transport the beam to a Fabry-Perot cavity. Monitoring the Fabry-Perot transmission signal allows the intensities of the two frequencies to be balanced by adjusting the Bragg angle of the AOM.

The AOM is driven at 60 MHz ($\delta/2\pi = 60$ MHz) by an HP 3200B which is amplified by a MiniCircuits ZHL-1-2W RF amplifier. For the bichromatic force to work at this detuning, the beam needs an intensity of $\sim 4000 s_0$ (s_0 is the saturation intensity for the $2^3 S_1 \rightarrow 2^3 P_2$ transition, 0.17 mW/cm^2) [58][47]. This is accomplished by sending the modulated light to a Keopsys Ytterbium (Yb) - doped fiber amplifier (model KPS-CUS-BT-YFA-36-SLM-PM-LIP-121-FA-FA) to get amplified. The pump light from internal diode lasers is injected through a V-groove of the Yb-doped fiber to invert the population inside the fiber and thus lead to amplification. The Keopsys fiber amplifier has three amplification stages which are separated by optical isolators to prevent light back-reflection. It begins with a pre-amp stage, which is supposed to saturate the input for the next two amplification stages. The next two stages are pumped by diode lasers and we can turn up the diode's current to get output power of the fiber amplifier up to 5 W. In addition, this amplifier offers two different modes: Automatic Current Control (ACC) and Automatic Power Control (APC). In ACC mode, the amplifier is running in order to maintain a constant set current through the pump diodes. A variation of the input power might induce a variation of the output power. In APC mode,
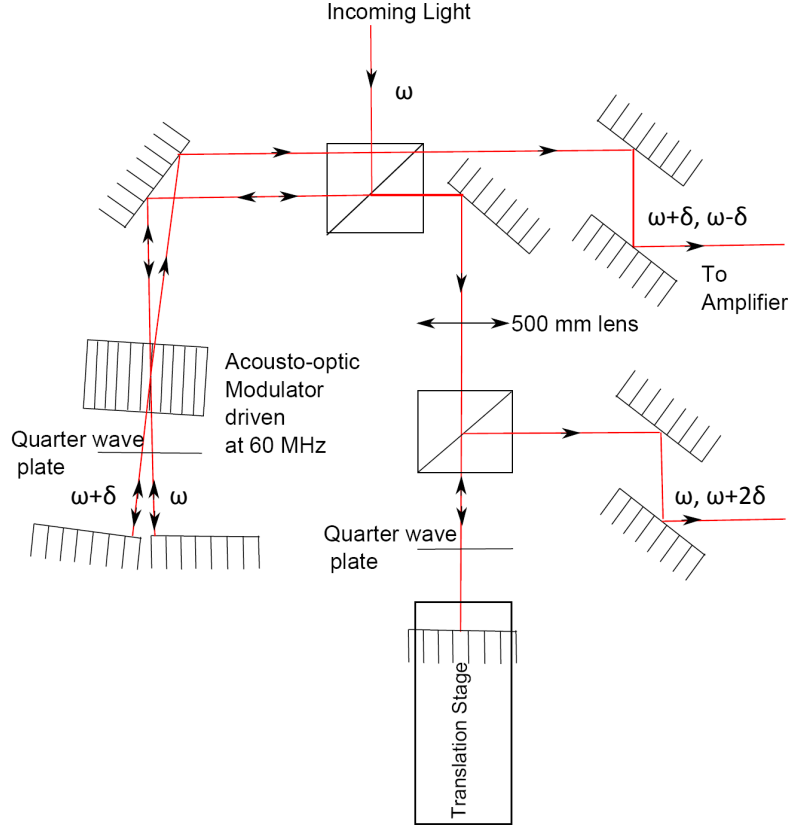
Figure 3.12: Double passing an AOM produces two beam with two frequencies [55]. The $(\omega_0 + \delta, \omega_0 - \delta)$ beam is used for our bichromatic force.

the amplifier is regulated at a fixed output power set point. The device is running in order to maintain a constant optical output power monitored with a photodiode. The current of the pump diode is adjusted to drive a constant output power independent of the input power.

In order for the amplifier to operate safely, it needs to be seeded with at least -3 dBm (0.5 mW) of light. To set the polarization of the light into the input PM fiber of the amplifier, we add a thin fiber paddle (Thorlab FPC560) for polarization control and two mating sleeves for fiber-to-fiber connection. Although we have about 1mW out from the PM fiber between two laboratories, after all those extra components, we only have about -2.5 dBm light into

the fiber amplifier, which is too close to the safety limit. Due to temperature fluctuations, sometimes, it might be even lower than -3 dBm. So before the paddle, we first amplify the light intensity using a OIYb30 fiber amplifier from Optocom Innovation (with maximum output power about 1 W) to maintain the input light of the 5 W amplifier above 0 dBm.

The output from the fiber amplifier is collimated and sent transversely across our atomic beam immediately downstream from the STIRAP beams. It is retro-reflected by a mirror, which is set on a stage to obtain a phase delay of $\pi/2$ (Section 5.2.1). This makes the remaining metastable atoms which are not excited by STIRAP well separated from the main atomic beam, so that we can tell the efficiency of our STIRAP by measuring the pushed-out atomic flux.

Chapter 4

STIRAP

4.1 Introduction

For a two level atomic system, incoherent radiation could change the ratio of the atomic populations by absorption, stimulated emission and spontaneous emission. The rate could be calculated from the Einstein coefficients [61]. For intense radiation near atomic resonance, the excited state population saturates at 50%, as shown in Figure 4.1.

The case of coherent excitation is markedly different. For laser light with frequency on resonance with the atomic transition, we will see an oscillation between 0 and 1 of the population in the excited state. The oscillation frequency is called the Rabi frequency [62][5], which is defined by

$$\Omega = -\frac{e}{\hbar}\mathcal{E}_0\langle e|r|g\rangle = -\frac{\mu\mathcal{E}_0}{\hbar} \tag{4.1}$$

where $\mathcal{E}_0$ is the amplitude of the coherent field, $|g\rangle$ is the ground state and $|e\rangle$ is the excited state, $\mu = e\langle e|r|g\rangle$ is called the dipole transition moment which depends on the quantum numbers of the states involved. And if the laser is not on the atomic resonance frequency,
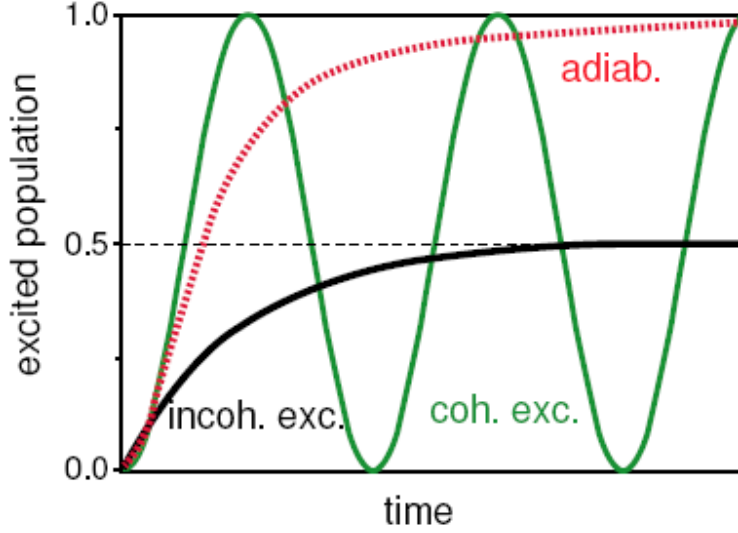
Figure 4.1: Evolution of the population of the upper level in a two-level system, driven by coherent radiation, by an incoherent radiation field, and by an adiabatic passage process [17]

but with a detuning δ, the effective Rabi frequency is

$$\Omega_{eff} = \sqrt{\Omega^2 + \delta^2} \tag{4.2}$$

The oscillation period gets shorter and the maximum population of the ensemble in the excited states goes down from 1 to $(\Omega/\Omega_{eff})^2$, as shown in Figure 4.2. A light pulse with $\delta = 0$ and interval of T which satisfies $\Omega T = \pi$, transfers the atom from the ground/excited state to the excited/ground and is called a π-pulse.

A robust method for achieving efficient population transfer is adiabatic rapid passage (ARP). The frequency of the external field is slowly tuned across the atomic resonance from below resonance to above resonance or in reverse. The time scale of this frequency sweep must be slower than the Rabi frequency, but faster than the spontaneous emission rate. In the Bloch sphere picture, the Bloch vector precesses around Ω_{eff} at the frequency δ.
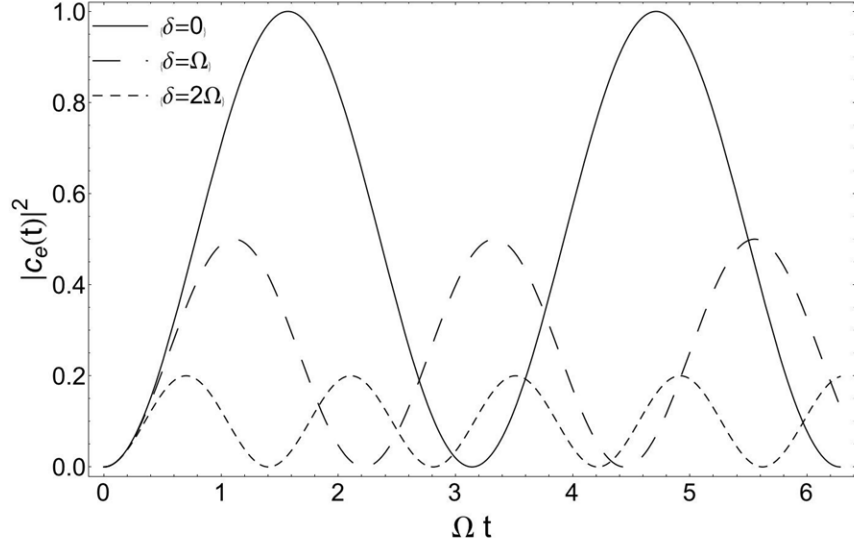
Figure 4.2: Rabi oscillations with and without detuning. When the laser is detuned away from resonance full population inversion no longer occurs and the oscillation period gets shorter.

Consider atoms in the ground state (south pole of the Bloch sphere) and a laser detuned to the far red side of resonance. By sweeping the detuning δ through zero, the Bloch vector will follow Ω_{eff} and end up parallel to $|\Omega_{eff}|$ in the excited state (north pole of the Bloch sphere). A more detailed description about ARP can be found in previous Ph.D. theses [63][64].

In our case, to excite the atoms from the metastable state to high Rydberg states, we need to do a two-photon transition in a three level system. In an intuitive excitation order, due to spontaneous emission and stimulated emission from the intermediate state, we could not get an average efficiency higher than 25%. So we use the technique called "Stimulated Raman Adiabatic Passage" (STIRAP), which permits the complete transfer of population between two quantum states. In essence, this procedure uses a pump pulse (near resonant with transition 1-2) and a Stokes pulse (near resonant with transition 2-3) to achieve complete

transfer of population between states 1 and 3. For this to occur, it is important that the Stokes pulse interact first (counterintuitive pulse order), that the pulses satisfy a few simple constraints on peak value and smoothness, and that the pulse frequencies together satisfy a two-photon resonance condition.

Hioe and Eberly's 1981 paper [65] first described this process in terms of an N-level coherence vector and its rotations. They continued their work with a paper concentrating on a three level system, which Hioe later developed as "generalized adiabatic following" or STIRAP. In this subsequent paper [66], the situation of a three-level system was addressed, including the use of pulsed light to drive the transitions. Interestingly, even though the use of pulses separated by a delay is mentioned, these papers do not specifically address the situation of the pulses arriving in the counter-intuitive order, i.e., the pulse driving the upper transition coming before the pulse driving the lower one, which is the hallmark of the STIRAP process. Among the first experiments to use the counter-intuitive pulse order was the switching of population between molecular vibrational levels by Klaas Bergmann and his colleagues in 1988 [67]. It was in 1990 in a subsequent paper [68] by the same group that the acronym STIRAP was coined. STIRAP experiments may be performed on an atomic (or molecular) beam, with "pulses" generated by the atoms passing through spatially separated laser beams perpendicular to the path of atoms. Alternatively, a sample of atoms can be illuminated by pulsed lasers with a time delay.

4.2 STIRAP Theory

Stimulated Raman Adiabatic Passage (STIRAP) combines features of the process of stimulated Raman scattering and adiabatic passage. A simple analysis of the STIRAP process for a three level system is given [69]. The three levels have eigenvector $|1\rangle$, $|2\rangle$ and
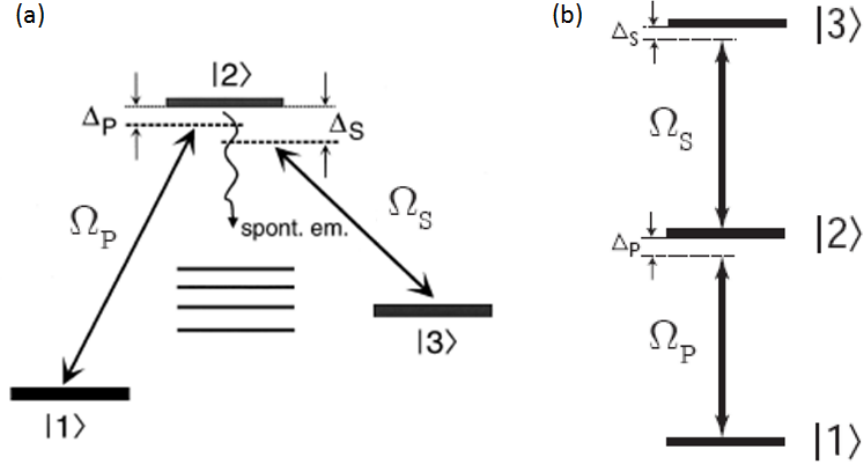
Figure 4.3: Three level Λ (a) and ladder (b) excitation scheme. $\triangle_P$ ($\triangle_S$) are the detunings for pump (Stokes) light and $\Omega_P(t)$ ($\Omega_S(t)$) are the Rabi frequencies of the pump (Stokes) light

$|3\rangle$ with a pumping light connecting the first two levels $|1\rangle$, $|2\rangle$ and a Stokes laser connecting levels $|2\rangle$ and $|3\rangle$. Under the rotating wave approximation (RWA), the Hamiltonian for the three level system, including the atom-field interaction, is:

$$H = \frac{\hbar}{2} \begin{pmatrix} 0 & \Omega_P(t) & 0 \\ \Omega_P(t) & 2\triangle_P & \Omega_S(t) \\ 0 & \Omega_S(t) & 2(\triangle_P \pm \triangle_S) \end{pmatrix} \tag{4.3}$$

where the $\Omega_P(t)$ and $\Omega_S(t)$ are the Rabi frequencies of the pumping light and the Stokes light respectively, and $\triangle_P$ and $\triangle_s$ are the detunings of the pumping field and the Stokes field, as shown in Figure 4.3. $\triangle_P = (E_2 - E_1) - \hbar\omega_P$, $\triangle_S = (E_3 - E_2) - \hbar\omega_S$. ($\omega_P$ and ω_S are the frequencies of pump and Stokes fields.)

In the 3-3 position of the Hamiltonian matrix, the plus sign is taken when the three-level system is a ladder (or cascade) configuration, and the minus sign is used in Lambda or Vee

64

configurations. In the case of STIRAP, the two-photon resonance condition between states $|1\rangle$ and $|3\rangle$ should be fulfilled, so this 3-3 term should be zero, i.e., $\Delta_P = \pm\Delta_S = \Delta$. The eigenvalues $\hbar\omega^k$ of the Hamiltonian in Eqn. 4.3 yield the instantaneous energy corresponding to the instantaneous eigenstates $|a^k(t)\rangle$:

$$
\begin{aligned}
\omega^+(t) &= \triangle + \sqrt{\Omega_P^2 + \Omega_S^2 + \triangle^2} \\
\omega^0(t) &= 0 \\
\omega^-(t) &= \triangle - \sqrt{\Omega_P^2 + \Omega_S^2 + \triangle^2}
\end{aligned}
\tag{4.4}
$$

with eigenstates given as a superposition of the bare states $|1\rangle$, $|2\rangle$ and $|3\rangle$

$$
\begin{aligned}
|a^+(t)\rangle &= \sin\Theta \sin\varphi |1\rangle + \cos\varphi |2\rangle + \cos\Theta \sin\varphi |3\rangle \\
|a^0(t)\rangle &= \cos\Theta |1\rangle - \sin\Theta |3\rangle \\
|a^-(t)\rangle &= \sin\Theta \cos\varphi |1\rangle - \sin\varphi |2\rangle + \cos\Theta \cos\varphi |3\rangle
\end{aligned}
\tag{4.5}
$$

Here $\Theta(t)$ and $\varphi(t)$ are defined as

$$
\tan\Theta(t) = -\frac{\Omega_P(t)}{\Omega_S(t)}
\tag{4.6}
$$

$$
\tan 2\varphi(t) = -\frac{\sqrt{\Omega_P(t)^2 + \Omega_S(t)^2}}{\triangle}
\tag{4.7}
$$

The eigenstate $|a^0(t)\rangle$, known as the trapped state, is of particular interest since this eigenstate does not involve the bare intermediate state $|2\rangle$ at all. In the case that the lifetime of the intermediate state is shorter than the interaction time, populating the intermediate state would be really deleterious due to its spontaneous decay, and would lead to a significant unwanted loss in transferring population to the final states. As for our experiment, the lifetime of the intermediate 3^3P_2 level is about 107 ns. Hence, if we can make sure that the

real time state vector $|\Psi(t)\rangle$ is tied to the trapped state $|a^0(t)\rangle$ during the whole interaction time, then the intermediate state will never be populated.

Then if we let Θ start at zero and go to $\pi/2$, this trapped state eigenvector evolves from $|1\rangle$ to $|3\rangle$, providing efficient population transfer from initial state to the final state. To achieve this, we need to control the Rabi frequencies of the pump and Stokes laser in a suitable way, satisfying the following condition [70]:

$$\frac{\Omega_P(t \to -\infty)}{\Omega_S(t \to -\infty)} \to 0, \qquad \frac{\Omega_S(t \to +\infty)}{\Omega_P(t \to +\infty)} \to 0 \qquad (4.8)$$

This corresponds to a counter-intuitive pulse ordering, as shown in Figure 4.4. We can identify three distinctly different time intervals 1, 2 and 3. In interval 1, only the Stokes laser is present, and the mixing angle Θ is zero. Therefore, the state $|a^0\rangle$ is identical to $|1\rangle$ as well as the state vector $|\Psi\rangle$ since the atom starts in this state, i.e. the three vectors are aligned (see Figure 4.5). In the interval 2, the Stokes laser Rabi frequency is smoothly reduced while the pump laser Rabi frequency increases to its maximum value, changing the mixing angle smoothly form 0 to $\pi/2$. As shown in Figure 4.5, the vector $|a^0\rangle$ is rotated into a position parallel to the bare state $|3\rangle$ in a plane perpendicular to the bare state $|2\rangle$ because $|a^0\rangle$ has no $|2\rangle$ component.

In the region where the Stokes light is very strong and pump beam is very weak, the energy level of the two higher levels are shifted too far off resonance so that the pump light does not produce excitation from the level $|1\rangle$ to intermediate level $|2\rangle$. Since the same mechanism leads to electromagnetically induced transparency (EIT), this region is called "pump induced EIT phase". Similarly, in the region where the pump light is very strong and the Stokes light is very weak, the weak Stokes light is not going to result in any stimulated emission from $|3\rangle$ to $|2\rangle$. It is called "Stokes induced EIT phase".
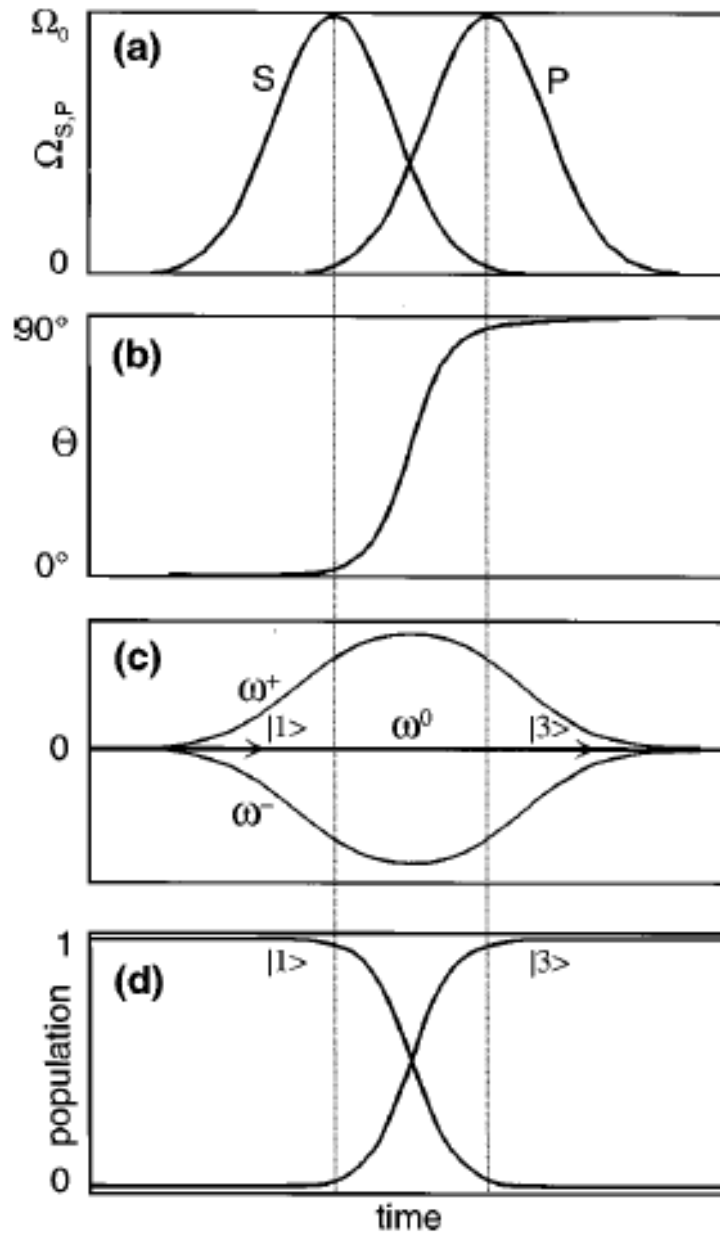
Figure 4.4: Time evolution of (a) Rabi frequencies of the pump and Stokes beams, Ω_P, Ω_S; (b) the mixing angle Θ, (c) the dressed state eigenvalues $\omega^{0,\pm}$; and (d) the population of the initial level $|1\rangle$ and final level $|3\rangle$ [17].
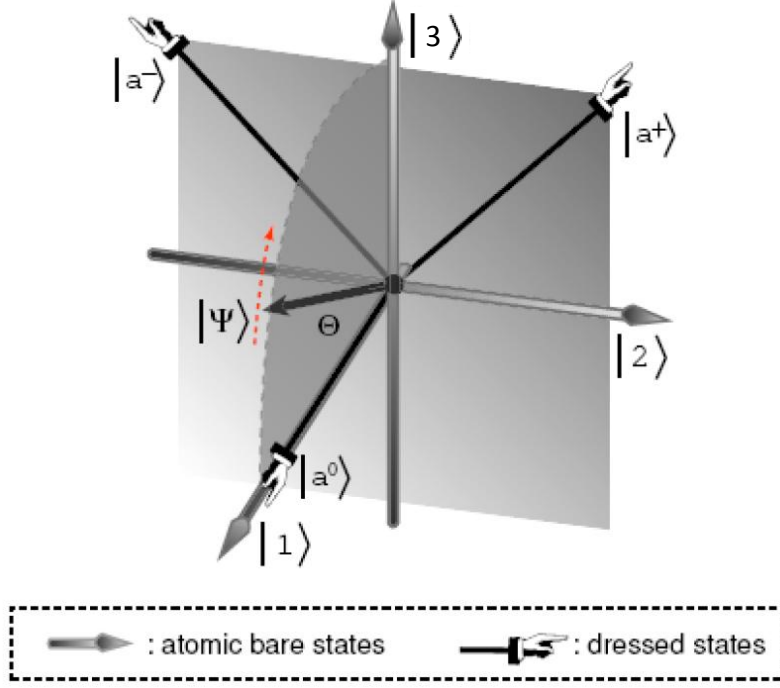
Figure 4.5: State vector $|\Psi\rangle$ for the three level system in the basis of the bare states ($|1\rangle$, $|2\rangle$ and $|3\rangle$) and in the basis of the dressed states ($|a^0\rangle$, $|a^+\rangle$ and $|a^-\rangle$) [17][70].

We can also look at the evolution from the aspect of the eigenvalues, as shown in Figure 4.4 (c). At very early times, both Rabi frequencies are zero, all three dressed state eigenvalues are degenerate as $\omega = 0$. Later in region 1, the degeneracy of the eigenvalues is lifted due to the coupling between states $|2\rangle$ and $|3\rangle$ from the Stokes laser. The eigenvalue that remains unchanged is associated with $|a^0\rangle$. In interval 2, the splitting of the eigenvalues is the largest since the coupling is strongest and both pump laser and Stokes laser contribute to it as in Eqn. 4.4. In the meantime, if the state vector $|\Psi\rangle$ evolves adiabatically, it follows $|a^0\rangle$ and moves from its position parallel to state $|1\rangle$ to a position parallel to state $|3\rangle$ as shown in Figure 4.5, which results in complete population transfer. If the coupling is insufficient (nonadiabatic), the motion of the state vector will lag behind the motion of the dressed

states and it will precess around $|a^0\rangle$, then the state vector acquires a component along $|a^+\rangle$ or $|a^-\rangle$. This means that some population will get to the leaky intermediate state and the transfer process is incomplete.

4.3 Conditions for STIRAP

4.3.1 Adiabatic Following

For the greatest efficiency in adiabatic passage, non-adiabatic coupling must be small. The Hamiltonian matrix element for nonadiabatic coupling between the trapped state $|a^0\rangle$ and the states $|a^\pm\rangle$ is given by $\langle a^\pm|\dot{a}^0\rangle$ [17]. Nonadiabatic coupling is small if this matrix element is small compared to the field induced splitting $|\omega^\pm - \omega^0|$ of the energies of these states, i.e.,

$$|\langle a^\pm|\dot{a}^0\rangle| \ll |\omega^\pm - \omega^0| \tag{4.9}$$

Using equations (4.5) to express the strength of the nonadiabatic coupling, we have

$$\begin{aligned} |\langle a^+|\dot{a}^0\rangle| &= -\dot{\Theta}\sin\varphi \\ |\langle a^-|\dot{a}^0\rangle| &= -\dot{\Theta}\cos\varphi \end{aligned} \tag{4.10}$$

and therefore the adiabatic constraint simplifies to [68]

$$|\dot{\Theta}| \ll |\omega^\pm - \omega^0| = \triangle \pm \sqrt{\Omega_P^2 + \Omega_S^2 + \triangle^2} = \Omega_{eff} \tag{4.11}$$

In the case of one photon resonance ($\triangle = 0$), $\Omega_{eff} = \sqrt{\Omega_P^2 + \Omega_s^2}$. From the definition of Θ, Eqn. (4.6), we have

$$|\dot{\Theta}| = |\frac{\dot{\Omega}_P\Omega_S - \dot{\Omega}_S\Omega_P}{\Omega_P^2 + \Omega_S^2}| \ll \Omega_{eff} \tag{4.12}$$

Adiabatic following is satisfied as long as Eqn. (4.12) holds throughout the whole interaction time. This can be evaluated for any time t with given laser pulses, so it is called the "local" adiabaticity criterion. When the laser pulses have a smooth shape, a "global" adiabaticity criterion may be derived from Eqn. (4.11) by taking a time average of the left side. If the pump and the Stokes pulse overlap in a time interval $\Delta\tau$, the total angle change is $\pi/2$, $\langle\dot{\Theta}\rangle = \frac{\pi}{2\Delta\tau}$, so the global criterion essentially is

$$\Omega_{eff}\Delta\tau \gg 1 \tag{4.13}$$

It is recommended to keep $\Omega_{eff}\Delta\tau$ larger than 10 based on experimental results and numerical simulations. There is a limit, too, to how small the Rabi frequencies can be. Usually, they have to be much larger than the natural linewidth of the corresponding transition.

4.3.2 Detunings from One-Photon and Two-Photon Resonance

In contrast to the case of perfect adiabatic evolution, beyond the adiabatic limit, the intermediate-level detuning does affect the transfer efficiency. This is so because the intermediate detuning is involved in the adiabaticity condition and for any fixed pulse area defined as $\int_{-\infty}^{+\infty} \Omega_{s,p}(t)dt$, the adiabaticity deteriorates as Δ increases. The transfer efficiency vanishes at very large detuning. If we define $\delta_{1/2}$ as the intermediate detuning at which the final state population equals $1/2$ (essentially the half linewidth), it has been demonstrated that $\delta_{1/2}$ grows with the square of the pulse area [71]. $\delta_{1/2} \approx c\alpha^2$, where α is the pulse area and the coefficient c may depend on the pulse shapes, the pulse delay, etc., but not on α.

In the case of detuning from two-photon resonance, the linewidth increases only approximately linearly with the pulse area [72]. It was shown that for a characteristic time of the pulses greater than the spontaneous decay time of the intermediate state, the two-photon
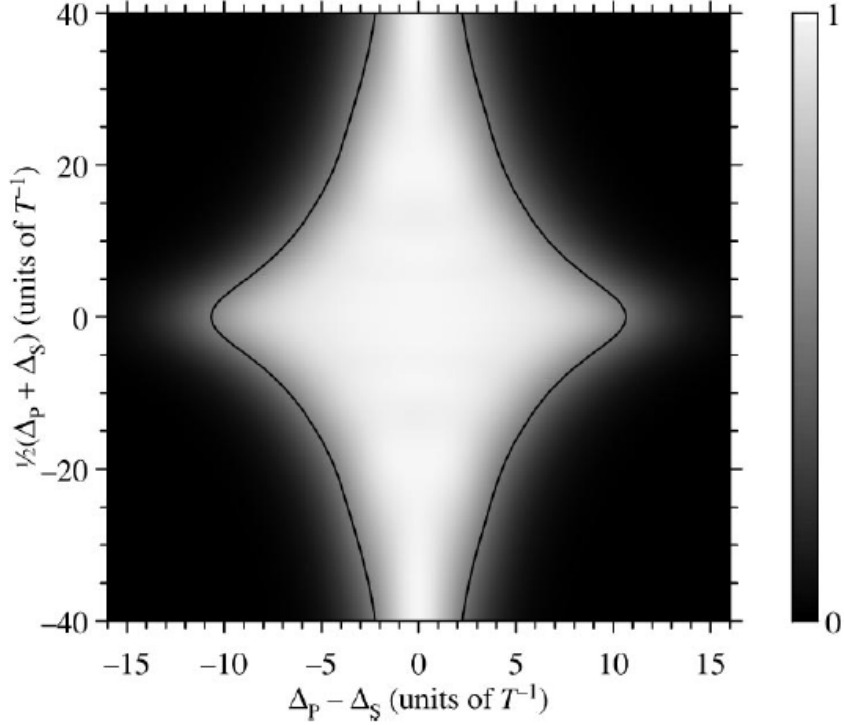
Figure 4.6: Numerically calculated transfer efficiency in STIRAP vs. the sum and the difference of the pump and Stokes detuning (i.e. efficiency vs. the single photon and two-photon detunings) for Gaussian pulse shapes, $\Omega_P = \Omega_0 exp[-(t-\tau)^2/T^2]$, $\Omega_S = \Omega_0 exp[-(t+\tau)^2/T^2]$, with $\Omega_0 T = 20$, $\tau = 0.5T$ [73].

lineshape for population transfer using STIRAP is close to Gaussian. Based on these facts, STIRAP is much less sensitive to single photon detuning than to two-photon detuning [73], as shown on figure (4.6). Figure 4.6 is for a Λ system, so the horizontal axis shows the two-photon detuning and the vertical axis shows single photon detuning.

If the intermediate state is far detuned so that the detuning is a lot larger than the Rabi frequencies Ω_P ($|1\rangle - |2\rangle$) and Ω_S ($|2\rangle - |3\rangle$), then the three level system reduces to a two level system [74]. Thus, the two-photon Rabi oscillation between the first level and the third level with respect to two-photon interaction time would be seen, as in [75]. This is different

from our adiabatic condition.

Generally speaking, if the pulses are coincident or are in the intuitive order, Rabi oscillations result and the system is sensitive to laser parameters, In the counterintuitive order and with Eqn. (4.13) satisfied, the system is relatively insensitive to these parameters.

4.3.3   Pulse Delay

The objective of the delayed-pulse scheme is to maximize the projection of the vector representing the bare state $|1\rangle$ onto the state $|a^0\rangle$, i.e. $|\langle 1|a^0\rangle|$. For overlapping beams, state $|1\rangle$ has nonvanishing components along all states $|a^0\rangle$, $|a^+\rangle$ and $|a^-\rangle$, and only the projection on $|a^0\rangle$ can be used for efficient population transfer, because the population of the other states may be lost through radiative decay. For large delay, $|\langle 1|a^0\rangle|$ approaches unity at earlier times. However, if the delay is too large, then the adiabatic condition (Eqn. 4.11) may be poorly satisfied and nonadiabatic transitions would lead to population loss. It has been calculated that for the optimum delay, the mixing angle should reach an angle of $\pi/4$ when Ω_{eff} reaches its maximum value [17].

To prove that the STIRAP mechanism works with a counter-intuitive pulse order, we measured the relative transfer efficiency as the overlap between the laser beams is varied with all other parameters, such as laser frequencies and intensities, remaining unchanged. Figure 4.7 shows a typical result of our measurements.

The data is taken from an ion detector, which is downstream from our interaction region and monitoring the Rydberg atoms that are ionized after STIRAP, as shown in Figure 2.4 and 2.5. The horizontal axis shows the scanning of the DC electric field in one period (10 Hz). In the first half of the scan the field increases, and in the second half it decreases, so essentially the two sets of peaks are identical. The peaks indicate that excitation to Rydberg

levels occurs as we scan through our Stark map. Both of the laser beams are collimated by cylindrical telescopes to an elliptical shape. The intensity FWHM of both the red and blue beams is about 500 microns horizontally (along the atomic beam direction) and 2.0 mm vertically. The reason that we make both beams much larger than the atomic beam size is that we want to make sure that the atoms at the beam edge see close to the same light intensities to maintain equal Rabi frequencies to the atoms in the beam center. We set the two beams in a co-propagating configuration by using a dichroic mirror which reflects blue light and transmits red light. The dichroic mirror is on a precision stage, and by moving the position of this stage, we can easily change the blue light position with respect to the red. The blue beam position axis tells us the relative position of our red and blue beam. In the positive region, the blue light is ahead of red, in the intuitive order and in the negative region, the red light is ahead of blue, in the counter-intuitive order. Zero is where the two beams are overlapping. Here, we can clearly see that when the red beam us ahead of blue by 0.5 mm ($\sim$ 0.5 μs delay time), the peak signal is about 3 times larger than the signal when red and blue are overlapping. The peak Rabi frequency is about 25 MHz for the blue light and 17 MHz for the red light, so the adiabatic condition $\Omega_{eff}T \gg 1$ is satisfied.

By comparing ion signals with different relative positions of red and blue light, we have confirmed that STIRAP is an efficient way to improve our population transfer rate, but to get an absolute value of the STIRAP efficiency, we need an absolute measurement. Absolute efficiency measurements will be discussed in the next chapter.
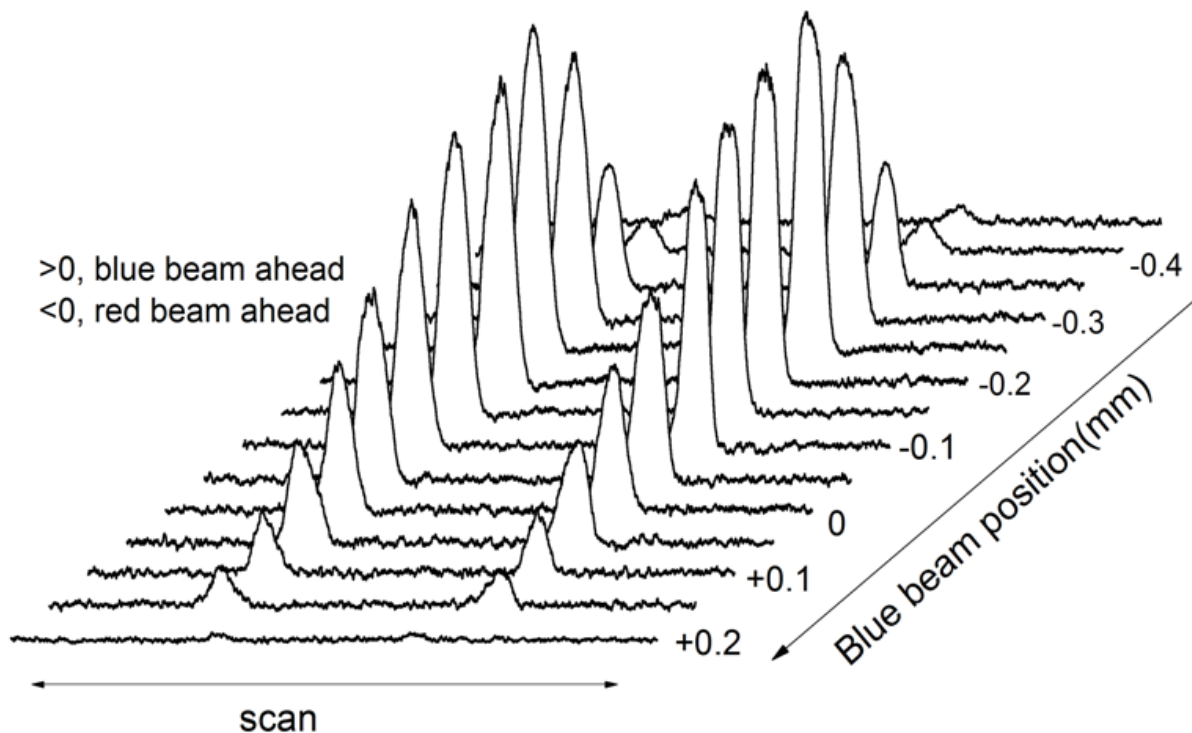
Figure 4.7: Ion detector signal showing relative population transfer from the He metastable state (2^3S_1) to the 24^3S_1 state as a function of the overlap between the Stokes (red) and the pump (blue) lasers. The positive region is where the blue light is ahead of the red, in the intuitive order and the negative region is where the red light is ahead of blue, in the counter-intuitive order. At zero, the two beams are overlapping.

Chapter 5

Absolute Measurements of STIRAP Efficiency

5.1 Introduction

To measure the absolute excitation efficiency for STIRAP, we need an effective way to distinguish the He* atoms that are excited to the Rydberg state from those that remain in the metastable 2^3S_1 state. In previous papers, the absolute efficiency measurements of STIRAP were mostly based on field ionization, photoionization or fluorescence [20][21]. For example, Cubel at al. [22] used two STIRAP stages and counted the Rydberg ^{85}Rb atoms by field ionization after the first and the second STIRAP stage. By comparing these two counts, they got a phenomenological efficiency of 50%, and after corrections, they claimed a maximum efficiency of about 70% near the center of the excitation region.

We first measured the absolute efficiency of STIRAP excitation using radiation pressure from a 30 mm wide curved wavefront light beam of $\lambda = 1083$ nm to deflect residual 2^3S_1 metastable atoms out of the atomic beam. In this way, the metastable atoms are spatially

separated from the rest of the beam and we counted their flux with and without the STIRAP beams with the SSD detector after flight on a long beam path. More recently, we further narrowed down the deflection region in order to lower the decaying probability from the Rydberg states back to the metastable state before and during the deflection process, using the bichromatic force, which is much stronger than the radiative force. If our STIRAP efficiency is 100% so that all the metastable He* atoms are excited to Rydberg states, the 1083 nm bichromatic beam is not going to cause any deflection, because there are no residual 2^3S_1 atoms and only such atoms can be deflected. On the other hand, if there is no Rydberg excitation at all, we will see the highest deflected flux and this can be calibrated by using the bichromatic beam and blocking the STIRAP beams. Therefore, the ratio of the deflected flux measured with STIRAP beams on and off provides an absolute measure of the fraction of the atoms remaining in the 2^3S_1 state, from which we get the STIRAP efficiency with high absolute accuracy.

5.2   Experimental Setup

Figure 5.1 shows a top view of the setup for the absolute efficiency measurements. About 23 cm downstream from the source, a 0.3 mm wide by 0.5 mm high aperture is used to collimate the atomic beam. After 26 cm further, the red (790 $\sim$ 820 nm) and the blue light (389 nm) are incident perpendicularly to the atomic beam in a counter-intuitive order to do the STIRAP excitation from the metastable He* state to a highly excited Rydberg level. Both beams are linearly polarized in the vertical direction along the electric field, and their intensity FWHM is about 0.5 mm along the atomic beam direction and 2.0 mm along the vertical direction. Because the vertical beam waist size is large (1.7 mm), even atoms at the vertical extreme of the atomic beam experience a Rabi frequency that is more than
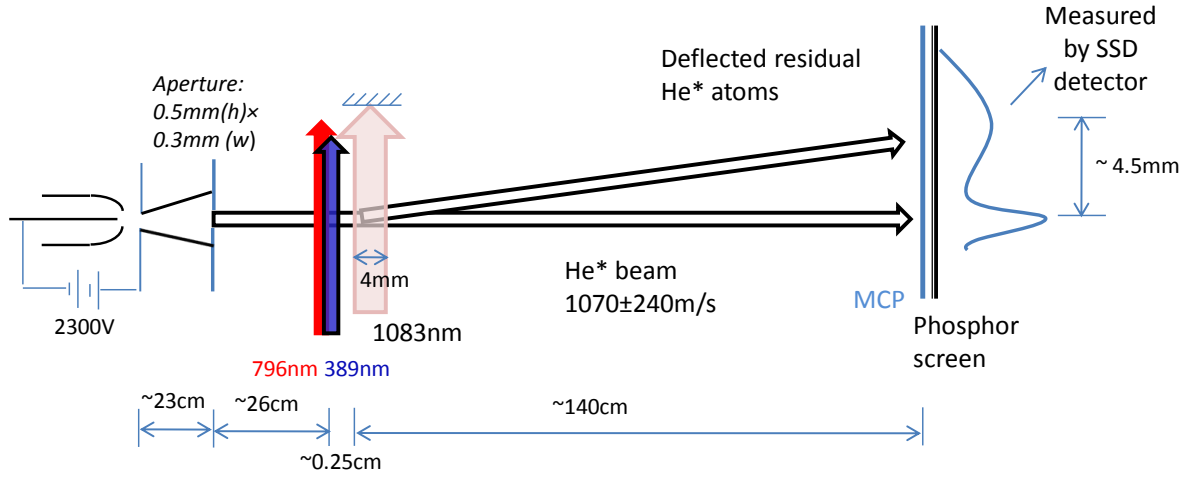
Figure 5.1: Experimental setup for the absolute efficiency measurements for STIRAP.

80% of the maximum at the center. After this interaction region, the atomic beam consists of Rydberg atoms, residual metastable atoms, ground state He, and some UV photons are also mixed in the beam. Just after the STIRAP region, we use the bichromatic force from 1083 nm light, which corresponds to the transition between the metastable 2^3S_1 state and the 2^3P_2 state, to deflect the residual metastable atoms out of the beam while leaving other components unperturbed. The bichromatic beam is only 4 mm wide along the atomic beam path, and the distance between the peak of the blue light and the edge of the bichromatic beam is 2.5 mm. Then in the detection region, we see a deflected peak about 4.5 mm away from the original source center and the strength of this peak changes linearly with the residual metastable counts. Thus, measuring the SSD output current in the deflected beam region with STIRAP beams on and off gives us the absolute efficiency of STIRAP.

5.2.1 Bichromatic Force

The bichromatic force has been described in the literature and well studied in our lab [43][76][77]. For this experiment, we require two optical frequencies to deflect the beam. But in the case of neutral atom lithography, four frequencies are used to collimate the atomic beam in two dimensions [58][47][55]. The four frequency production is described in detail in Chapter 3 Section 3.4.2. Here, a brief description will be given, explaining why the bichromatic force is much larger than the radiative force and hence more suitable in this experiment.

The π-pulse model for describing bichromatic forces provides an intuitive notion of how it works. Consider a laser beam consisting of two frequency components of equal strength and symmetric detuning above and below atomic resonance. The total electric field could be written as:

$$E = E_0\{\cos[(k + \triangle k)z - (\omega_a + \delta)t] + \cos[(k - \triangle k)z - (\omega_a - \delta)t]\} \tag{5.1}$$

$$= 2E_0 \cos(kz - \omega_a t) \cos(\delta t - \triangle kz) \tag{5.2}$$

where ω_A is the atomic resonance frequency, $k = \omega_a/c$ and $\triangle k = \delta/c$. From equation 5.2 we see that the beam can be described as an amplitude-modulated single carrier frequency at the atomic resonance frequency ω_a having modulation period π/δ. If the intensity of the beam is chosen so that the area under the envelope of one modulation period satisfies the π pulse condition for the atomic transition, i.e., $\Omega = \frac{\pi}{4}\delta$ [78], then in each modulation period the atoms undergo a level exchange between the ground state and the excited state.

Then if we retro-reflect the modulated carrier wave back by a mirror to create a standing wave, as shown in Figure 5.2, the atoms can first absorb a photon from the left and before the arrival of the next π-pulse from the left, a pulse from the right will drive the atom back
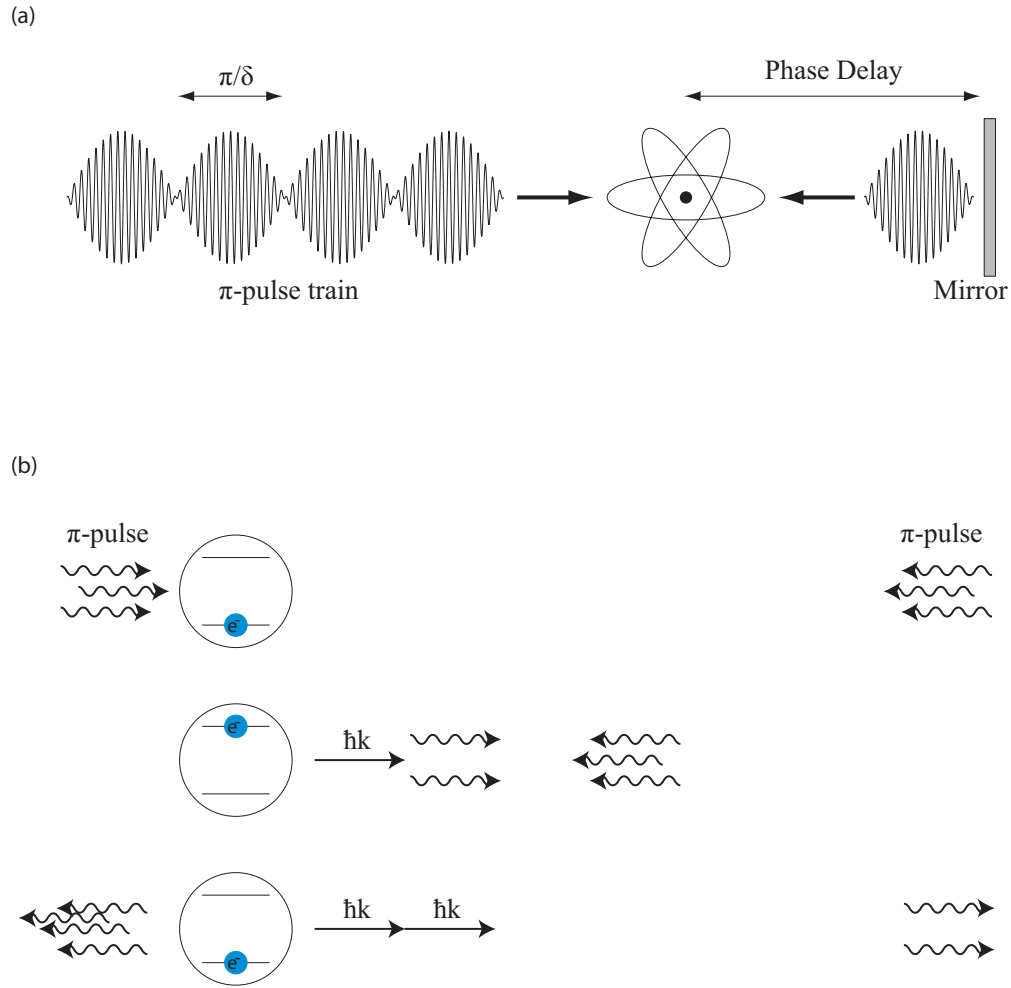
Figure 5.2: The two frequencies in the bichromatic laser beam create a series of π-pulses from the beat frequency. Each π-pulse excites or de-excites the atom in a time of π/δ leading to a force $(\hbar k \delta/\pi)$ much larger than $F_{rad,max} \sim \hbar k \gamma/2$.

to the ground state. The momentum kicks for the absorption and the stimulated emission are therefore in the same direction, to the right. Since this happens with a time period of π/δ, the resulting force can be written as

$$F = \frac{\triangle P}{\triangle t} = \frac{2\hbar k \delta}{\pi} \tag{5.3}$$

which is not limited by the radiative decay rate, γ, so this force can be much bigger than the radiative force $\sim \hbar k \gamma/2$ since δ could be $\gg \gamma$.

However, in order to get a large force in the correct direction, we need to control the phase delay between the counter-propagating beams. If the phase delay is chosen so that the sequence of π-pulses from alternating directions is evenly spaced in time, the average force is zero. A preferred direction for momentum transfer is established by providing an asymmetric pulse timing sequence. Because of this, the average strength of the bichromatic force is reduced by a factor of 2, F $\sim \hbar k \delta/\pi$ [59].

The more accurate way to describe the bichromatic force is by numerical integration of the optical Bloch equations. Now the resulting optimum Rabi frequency becomes $\Omega = \sqrt{\frac{3}{2}}\delta$ [59][47]. For our bichromatic beam, $\delta/(2\pi) = 60$ MHz, and the π-pulse length is 250 cm. To satisfy the π-pulse condition, the theoretical intensity should be $\sim 4000s_0$. Experimentally, the intensity is adjusted by the gain of the fiber amplifier to get the best deflection on our MCP/Phosphor detector.

The output light from the fiber amplifier is first sent to a spherical telescope comprised of two lenses with focal lengths 25 mm and 250 mm respectively to make the beam FWHM about 6.5 mm. Then a vertical slit ~ 0.4 mm confines the beam, so the light beam intensity encountered by the atoms is pretty uniform. A quarter-wave plate is used to change the polarization from linear to circular since the $\triangle m = \pm 1$ is the strongest transition. After
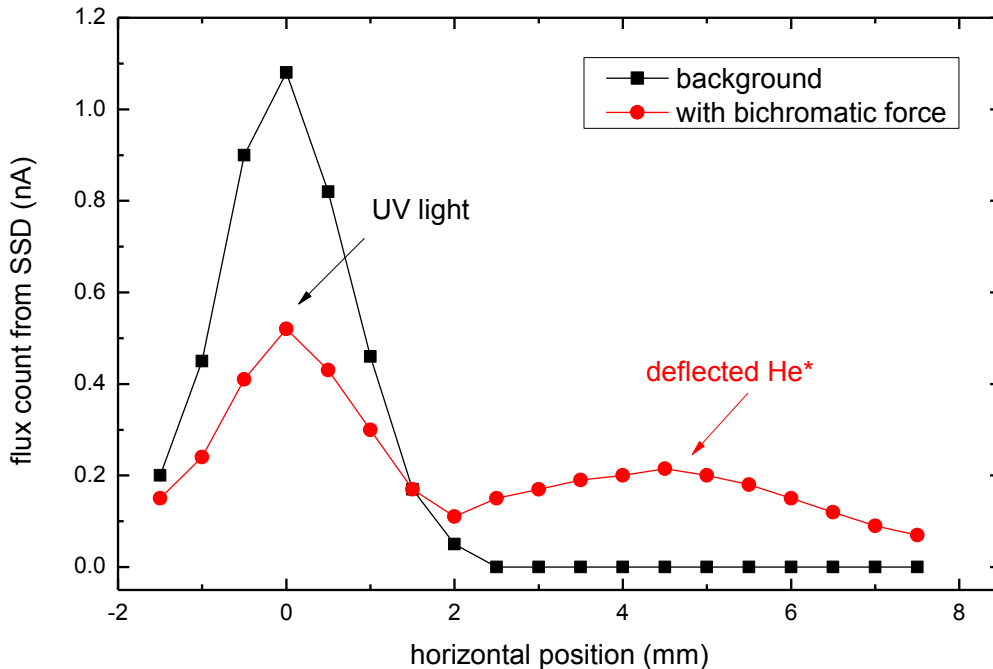
Figure 5.3: Deflection of the atomic beam by the bichromatic force. The line connecting square points is the original spatial profile of the atoms taken with the bichromatic laser beam blocked and the line connecting circle points is the profile with deflection

retro-reflection, the two counter-propagating circularly polarized light beams have the same helicity while they are interacting with the atoms.

Figure 5.3 shows a typical beam profile with and without bichromatic deflection, measured by the SSD. The retro-mirror was placed about 625 mm away from the center of the atomic beam, which corresponds to a path difference of about 125 cm and therefore a phase delay of about $\pi/2$. The intensity of the light is about $5000s_0$, a little higher than the theoretical value. The center of the deflected beam is shifted by about 4.5 mm from the initial center of the atomic beam. The force is a bit smaller than the predicted value, but good enough for our efficiency measurements. The deflected peak width is much broader than the original peak width mainly because of the large longitudinal velocity spread of the atomic

beam. In Figure 5.3, the total area under the curve with bichromatic deflection is a little smaller than the original area, because we are just looking at the deflection to one direction, but actually a small amount of the atoms were deflected in the opposite (wrong) direction. This is attributed to a small number of spontaneous emissions during the interaction time as a result of the long lifetime of the 2^3P state [76]. In the limit of infinite lifetime, the bichromatic force produces an atomic beam splitter [79].

5.2.2   Typical Signals

As mentioned earlier, in our experiments, STIRAP is implemented by scanning the voltage on the field plates through the Stark levels and maintaining the pump and probe beams in the counter-intuitive order. To measure the absolute efficiency of STIRAP, we monitor the flux in the deflected region with / without 1083 nm light and with / without STIRAP beams. A typical set of signals is shown in Figure 5.4.

The triangle wave (blue) shows the scanning of the electric field (or red laser frequency), with scanning range $\sim$ several times of the STIRAP full width. The flux level with bichromatic deflection using 1083 nm light is shown as the higher line (black). This baseline is higher because we have the largest amount of metastable helium atoms encountering the bichromatic force and thus the highest deflected flux. Once the two photon resonance condition is satisfied, some atoms are excited to a Rydberg state and become immune to the 1083 nm light, so fewer atoms get deflected and we see a reduced flux in the deflection region, as shown by the dips in Figure 5.4. The background flux without 1083 nm light is shown with the lower line (red). Without 1083 nm, the atoms are only affected by the radiative push from the 389 nm light, the atoms are not deflected far enough to reach our SSD detection region. One more thing we need to pay attention to are the small peaks sometimes shown
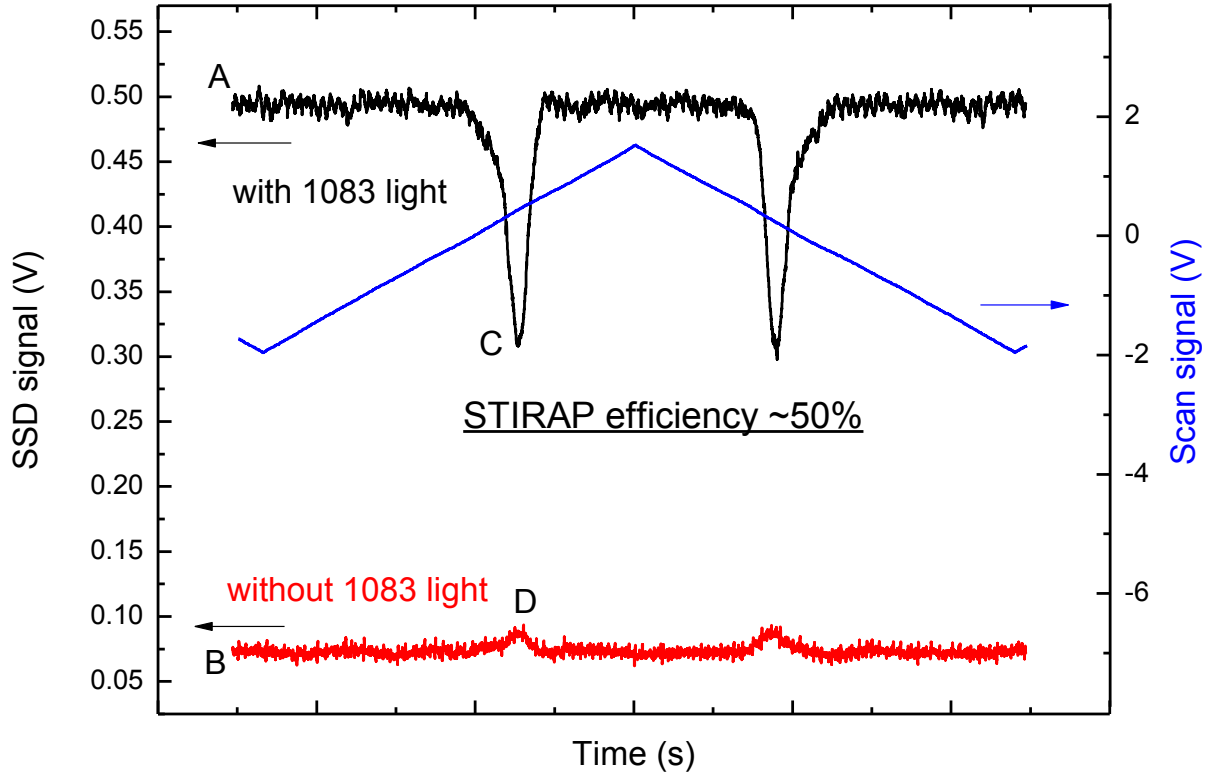
Figure 5.4: Typical signals of the STIRAP absolute efficiency measurements. The triangle wave (blue) shows the scanning of the electric field. The flux level with bichromatic deflection is shown as the higher line (black) and the background flux without 1083 nm light is shown with the lower line (red). A = flux level with 1083 light but without STIRAP excitation, B = flux level with neither the 1083 nm light nor STIRAP, C = flux with both 1083 nm light and STIRAP, D = flux without 1083 nm light but with STIRAP. The efficiency could be calculated as $(A - C + D - B)/(A - B)$. If there are not small peaks on the background signal, then $B = D$ and the formula simplifies to $(A - C)/(A - B)$.

on the background signal at the same voltage as STIRAP occurs. This is probably due to the expansion of the Rydberg beam as they pass the non-uniform electric field at the edge of the field plates. We have to subtract this small peak height out when we calculate the efficiency.

In the case of zero excitation rate, we would just see two horizontal lines. If the STIRAP efficiency is 100%, then the dip level on the upper line would be the same as the level of small peaks on the lower line, since, in this case, when STIRAP occurs, there is no difference with and without 1083 nm light. If we label the baseline of the upper line and the lower line as A and B respectively, and label the dip level on the upper line as C and the small peak level on the lower line as D, then $A =$ flux level with 1083 light but without STIRAP excitation, $B =$ flux level with neither the 1083 nm light nor STIRAP, $C =$ flux with both 1083 nm light and STIRAP, $D =$ flux without 1083 light but with STIRAP beams. The efficiency can then be calculated as $(A - C + D - B)/(A - B)$. If there are no peaks on the background signal, then $B = D$ and the formula simplifies to $(A - C)/(A - B)$. For the signal shown in Figure 5.4, $C - D \sim (A - B)/2$, and the efficiency of this STIRAP is about 50%.

5.3   STIRAP Efficiencies for $n = 24$

The data shown in Figure 5.4 is for the $n = 24$ manifold with red light wavelength at 795.4597 nm and a DC voltage offset on the field plates about 2.5 V. Both the red and the blue light are linearly polarized along the electric field direction. We have focused on $n = 24$ states and studied extensively the STIRAP efficiency with different parameters. The reason we chose $n = 24$ in the first place is that it is not too high to have a high enough Rabi frequency, but high enough to have a strong dipole interaction if we want to focus the atomic

beam with an electrostatic lens [25]. Typically, for the $24S$ state, the raw efficiency is around 40%, but for the manifold, the efficiency depends a lot on which level is being excited. For some of the states, the transition strength is a lot smaller than for the $24S$ state, so we don't have high enough Rabi frequency for the red light and the STIRAP efficiency is very low. The best peaks we could find on the 24 manifold give us efficiencies around $40\% \sim 50\%$.

The STIRAP efficiencies discussed here and also in the following are all with the best pulse delay (beam separation), and correspond to the highest ion signals as shown in Figure 4.7. Due to the drifting of the laser wavelength, beam alignments, source fluctuations, detector noises, etc., the typical absolute error of the efficiency measurements is about $\pm 1.5\%$.

5.3.1   Testing the Laser Parameters

We optimize our STIRAP process by measuring both the laser beam profiles and the total power, and then use the information to compute the spatial dependence of the Rabi frequency of the STIRAP beams from the atomic transition matrix elements. Since the beam profilometer measurements and the power measurements are accurate to a few %, we are confident of these calculated values of the Rabi frequencies.

The Rabi frequencies (defined in Eqn. 4.1) for the pump and Stokes light are related to the corresponding light intensities by $\Omega = \frac{\mu}{\hbar}\sqrt{\frac{2I}{\varepsilon_0 c}}$, where μ is the transition dipole moment and calculated as $e\langle e|r|g\rangle$. By calculating the matrix elements of the selected levels, we calculated conversion relations for the transitions $2^3S_1 \to 3^3P_2$ and $3^3P_2 \to 24^3S_1$ as shown in Table 5.1. For the states on the manifold of $n = 24$, the Stokes light Rabi frequencies are smaller compared to the S state, since the relative transition strengths are a lot smaller, as shown in Figure 1.2.

As we can see from Table 5.1, for comparable Rabi frequencies, the red light intensity

Transitions	$2^3S_1 \rightarrow 3^3P_2$	$3^3P_2 \rightarrow 24^3S_1$
$m = 0$	$\Omega_P(t) = 14.9 \times \sqrt{I_P(t)}\text{MHz}$	$\Omega_S(t) = 1.67 \times \sqrt{I_S(t)}\text{MHz}$
$m = \pm 1$	$\Omega_P(t) = 12.9 \times \sqrt{I_P(t)}\text{MHz}$	$\Omega_S(t) = 1.45 \times \sqrt{I_S(t)}\text{MHz}$

Table 5.1: Conversion from intensity (in the unit of W/cm^2) to Rabi frequencies.

has to be about two orders of magnitude greater than the blue light intensity. With our STIRAP beam size, intensity FWHM of 0.5 mm (horizontal) by 2 mm (vertically), to get a peak Rabi frequency of about 15 MHz, we need only about 14 mW of blue light but 1 W of red light. The difference of the Rabi frequency for $M_J = 0$ and ± 1 is not much, so we usually take the weighted average as the Rabi frequency for the linearly polarized transition.

On the other hand, we also checked the values for $2^3S_1 \rightarrow 3^3P_2$ transition in Table 5.1 by using the atoms themselves as probes by measuring the Autler-Townes splitting [80] of the 3^3P_2 states. We used the strong blue light to drive the $2^3S_1 \rightarrow 3^3P_2$ transition and the weak red light was used as a probe of the two-peak separation. Figure 5.5(a) shows samples from our spectra obtained by scanning the red laser frequency to excite metastable atoms to the 24^3S_1 state, with varying blue powers in zero electric field. These traces are with blue light on resonance, and Figure 5.5(b) is a plot of the separation between the peaks vs. $\sqrt{P_{blue}}$. We have also made measurements with the blue light tuned somewhat off-resonance, and observed the expected asymmetrical peak heights and broadened splitting.

The inset to Figure 5.5(b) shows the geometry of our setup for the Autler-Townes measurements, viewed along the laser beams. The blue light beam was expanded from its STIRAP size to have a FWHM profile as shown by the largest ellipse, and the red beam was moved to its center and focussed to somewhat smaller size as shown by the inner ellipse. The horizontal lines show the atomic beam's width where its profile is flat and maximum,
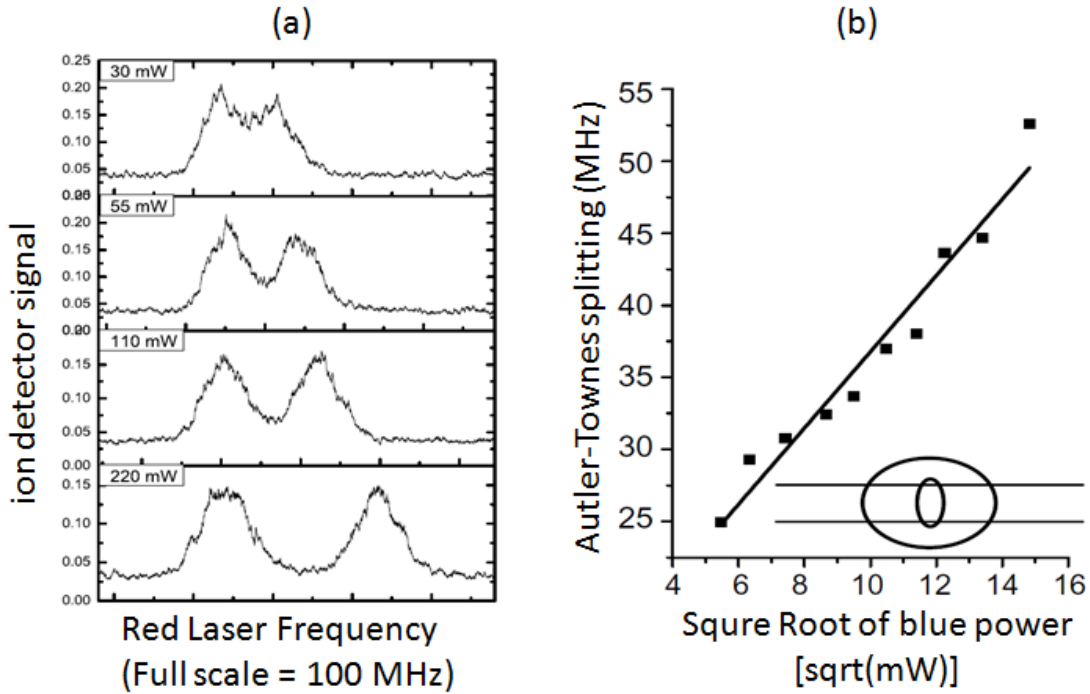
Figure 5.5: (a) shows a few traces of the measured ionization current derived from Rydberg atoms vs. red frequency. The double peaks are separated by the Rabi frequency of the blue light. (b) is a plot of the observed Ω vs. the square root of the uv power. The inset to (b) shows the geometry of the two laser beams and the path of the most intense, central part of the atomic beam.

but it has penumbral regions of comparable size above and below. Crude estimates suggest that 80% of the measured Autler-Townes signal comes from atoms that experience a Rabi frequency of at least 85% of the peak.

We convert P_{blue} to the peak intensity from our beam profilometer's fitted Gaussian parameters. Then, using values in Table 5.1, the weighted average peak Rabi frequency for blue light is $\Omega_P \approx 2.89\sqrt{P_{blue}}$ MHz with P_{blue} in mW. The slope of the fitted straight line in Figure 5.5(b) is $2.79(.22)\sqrt{P_{uv}}$ MHz. The agreement corroborates our confidence in knowing the nature of the light fields that the atoms experience.
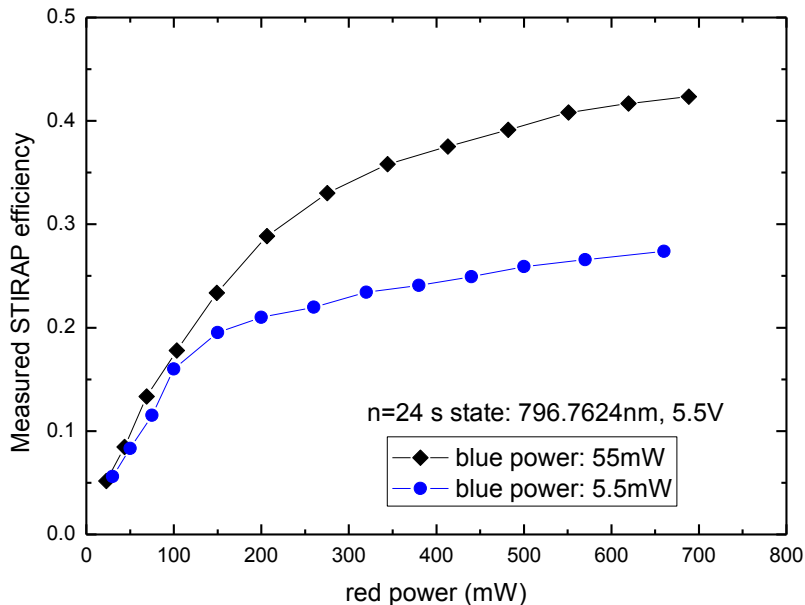
Figure 5.6: Measured STIRAP efficiency for 24S state with different red/blue light power. Red and also blue light are almost saturating the transition.

5.3.2 STIRAP With Different Red/Blue Power

Since we have available up to 60 mW of blue light in the interaction region, but only approximately 1 W of red light, the blue intensity for the STIRAP process could be more saturated. We measured the dependence of the STIRAP efficiencies on different red light powers with blue light at 55 mW and 5.5 mW, as shown in Figure 5.6. The STIRAP efficiency goes up with red light power, but tends to saturate at high power. Although the efficiency is also higher with higher blue light power, it is definitely more saturated with respect to blue light at 55 mW than with respect to red light at 700 mW, because if we attenuate the blue light to its 10% (5.5 mW), the efficiency drops from 42.5% to about 28%, but if we attenuate the right light to its 10% (70 mW), the efficiency drops to about 10%. From the trend of the curves, even with much more red and blue power, the STIRAP efficiency is not
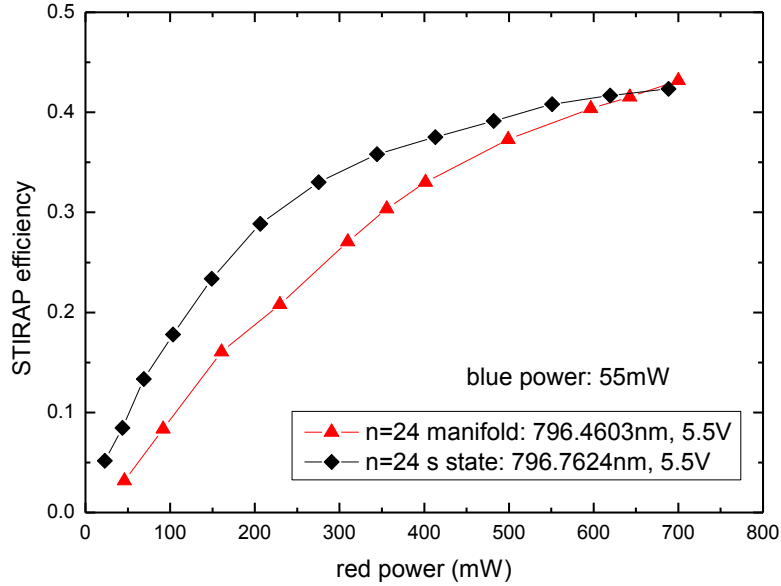
Figure 5.7: Comparison of STIRAP efficiency vs. red light power with 55 mW blue light for $24S$ and manifold. S state is more highly saturated than the manifold state.

going to increase above 50%.

We also compared the STIRAP efficiency vs. red light power curve for the $24S$ state and one of the manifold states. As shown in Figure 5.7, the manifold efficiency is not as highly saturated as the $24S$ state, which corroborates with Figure 1.2 that the transition strength on the mainfold is a lot smaller than it is for the S state, and thus with the same intensities, the Rabi frequency for the manifold is also a lot smaller compared to the S state. From Figure 5.7, we can also conclude that with higher red light power, we would have higher efficiency for the manifold. However, the efficiency we measured is actually smaller than the real efficiency due to the decay in the time interval after the STIRAP and before bichromatic deflection. Some of the atoms decay back to the metastable state as if they were never excited. In fact, the S state decays a lot faster than the manifolds. So this must be at least part of the reason why the measured efficiency for the manifold, if the red light

intensity is highly saturated, could be larger than it is for the S state.

Furthermore, the measured STIRAP efficiency for a pure D state at zero electric field is a little smaller than for the S state (blue light at 55 mW and red light at 700 mW), $\sim$ 39.0% compared to 42.5%. The red light intensity was highly saturated for the pure D state (different from the manifold states at nonzero field) because we attenuated the red light to 100 mW and the efficiency almost did not change. But the pure D state decays faster. If we take 1/(radiative lifetime τ), $1/(10.4\mu s)$ for $24S$ and $1/(8.66\mu s)$ for $24D$, as the decay rate [81], and take the distance from the center of the blue beam and the center of the bichromatic beam, $\sim$ 4.5 mm, as the decaying length d, then the ratio of measured STIRAP efficiency vs. real efficiency is $\sim$ 0.67 for $24S$ and 0.62 for $24D$ ($exp[-d/(\tau v)]$, v is the average of the atom longitudinal velocity $\sim$ 1070 m/s). If we add this correction back, their efficiency is roughly the same, $\sim$ 63%.

5.3.3 STIRAP With Different Intermediate States

If we include all the m_J sublevels of the intermediate and final states, our system is not a pure three level system any more. But with only the earth's magnetic field and the DC electric field in our interaction region, the sublevels are roughly degenerate with splitting less than 1 MHz. Based on the dependence of the STIRAP efficiency on magnetic field that Martin et al. have shown [82], this might not be a problem. They have shown that efficient transfer is possible for zero and large energy splitting (larger than the effective Rabi frequency), but fails for small splitting because the adiabatic transfer path is blocked due to the interaction of the states.

Because of the concern about multi-level interference in our system, we decided to lock the blue light frequency to the 3^3P_0 state and use 3^3P_0 as the intermediate level, making
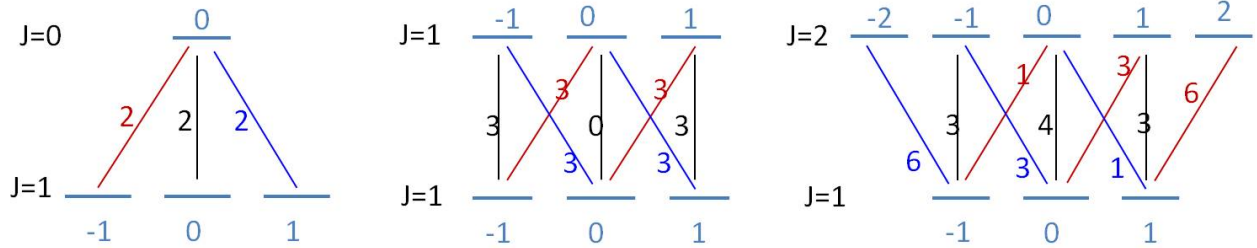
Figure 5.8: $^3S_1$ to $^3P_{0,1,2}$ transition strengths for various M_J and $\triangle m_J$ values

our system much simpler. With linearly polarized light, we would have only one possible transition, $m_J = 0 \rightarrow m_J = 0$. But since the atoms are initially evenly distributed on the three possible m_J levels in the S state, we will only have 1/3 of the atoms participating in the STIRAP transition and theoretically the best average efficiency we could get is 33%.

The wavelength for the blue light is around 777.9430 nm when it is locked to 3^3P_0 state. Since this was an increase in the blue light frequency, we had to tune the red light to lower frequency in order to get to the same final states. For example, if we want to excite the atoms to the 24S state at zero electric field, we need to tune the red light wavelength from 796.7615 nm for 3^3P_2 locking to 796.7804 nm for 3^3P_0 locking. In addition, as shown in Figure 5.8 [5], the transition strength to J = 0 is a little smaller compared to J = 2 for π-polarized light, so we also increased the red and blue light intensity about $1.5 \sim 2$ times to match the Rabi frequencies. Interestingly, the efficiency results (and also the ion signals) with intermediate level J = 0 turned out to be approximately 1/3 of what they were with intermediate level J = 2, which is consistent with the state populations. The best we have achieved is less than 15% for both the S state and the manifolds.

Similarly, we also tried to lock the blue light to the 3^3P_1 state. In this case, with vertically

polarized light, the (J=1, $m_J = 0$) to (J=1, $m_J = 0$) transition is forbidden as shown in Figure 5.8. Only 2/3 of the atoms could possibly be excited, which is consistent with our experimental results that STIRAP efficiencies (and also the ion signals) are about 30% less than the original values (with blue light locked to the 3^3P_2 state).

After all these tests, we are really confident that the coupling between different magnetic sublevels is not the reason for our relatively low STIRAP efficiency. Otherwise, we would have seen efficiencies with 3^3P_0 intermediate state close to 30%, significantly larger than 1/3 of the efficiencies we saw with the 3^3P_2 as the intermediate state.

5.3.4   STIRAP With Different Source Parameters

The source output is about 10^{14} He* atoms/sr-s. The solid angle of the atomic beam passing through the rectangular aperture is $\sim 2.5 \times 10^{-6}$ sr, so the flux is $\sim 3 \times 10^8$ He* atoms/s. It expands to $\sim 1.2 \times 1.5$ mm in the interaction region so that the density of our He* atoms is $\sim 2 \times 10^5$/cm^3 and the density of ground state Helium atoms is $\sim 5 \times 10^5$ times higher. The collisional mean free path for He* on He* at this density is about 5×10^7 m using the approximate geometric cross section, 10^{-15} cm^2. The corresponding free beam path for ground state He atoms is 5×10^5 times smaller, but still much longer than the distance the atomic beam travels in our system. We believe that collisions of He* on ground state He have negligible effect on the population transfer process. We also think that, with an average distance of 150 microns between atoms, the Rydberg-Rydberg interaction is also small, so that the Rydberg excitation blockade [30] is not happening.

To further confirm these ideas, we changed the densities of the metastable He* and ground state He by changing the He* source parameters. As shown in Figure 5.9(a), we changed the voltage on our source needle from 1300 V to 2900 V in 100 V increments and the metastable

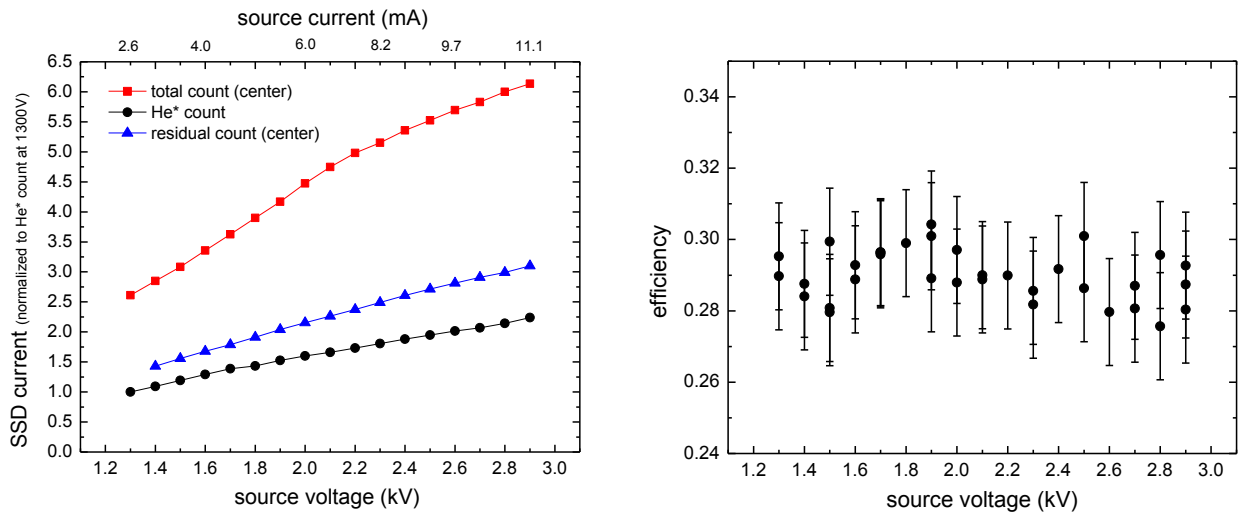Figure 5.9: (a) SSD current (He* count) vs. source voltage (current); (b) STIRAP efficiency vs. source voltage, showing efficiency essentially unchanged within the uncertainty range ±1.5%.
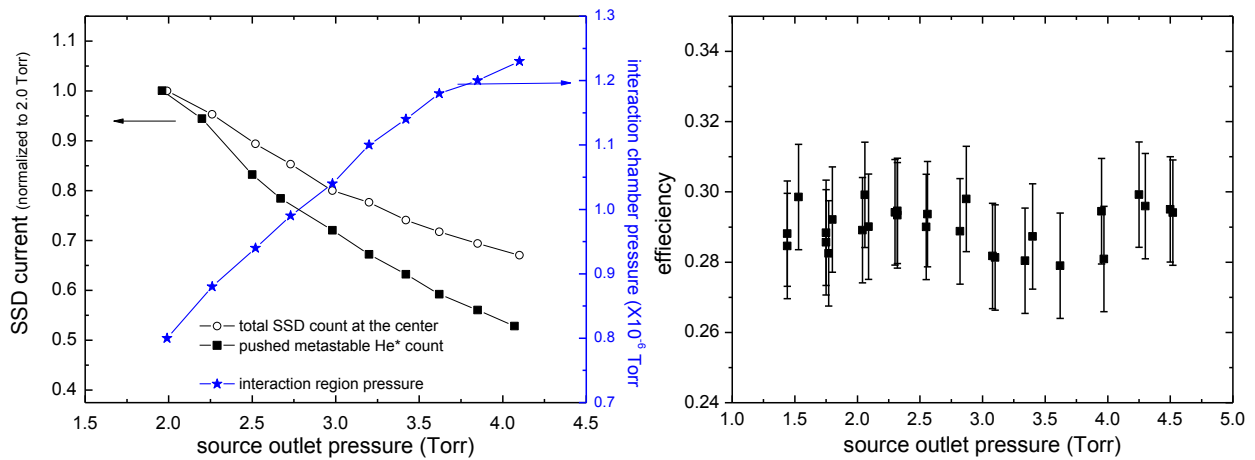
Figure 5.10: (a) Normalized SSD current (He* count) and chamber pressure vs. source outlet pressure; (b) STIRAP efficiency (remaining essentially unchanged) vs. source outlet pressure, uncertainty of the efficiency measurement ∼ ±1.5%.

He* count increased to 2.2 times of its original value, shown as the black dots. This was measured by the SSD using 1083 nm light to deflect He* atoms out of the beam. The red squares are measured with SSD at the center without any deflection (total count), and blue triangles are with SSD also at the center but with He* pushed out (the background photon counts). We did the efficiency measurements at each voltage setting. The results in Figure 5.9(b) do not show a He* density dependence and all lie in the range of $29\% \pm 1.5\%$, where $\pm 1.5\%$ is about the same as the absolute measurement uncertainty.

We also changed the He* source flow pressure and the results are shown in Figure 5.10. With source outlet pressure going from 2 Torr to 4.1 Torr, the He* population went down by about 50%, and the background pressure went up from 0.8×10^{-6} Torr to 1.24×10^{-6} Torr as a result of the increased density of ground state He. The resulting efficiencies of $29\% \pm 1.5\%$, seem independent of the flow pressure. Since we have shown that the STIRAP efficiency doesn't change with He* density in Figure 5.9(b), we can conclude that collisions with ground state He have negligible effects too.

5.3.5 Other Tests

We have made several attempts to improve our STIRAP efficiency, but have been unsuccessful. First we tried different red and blue beam sizes. We took out the cylindrical telescopes and made both the red and blue beam cross sections circular with intensity FWHM about 2 mm. We also tried to use a cylindrical lens to focus each beam to the center of the atomic beam so that their FWHM are about 170 microns along the atomic beam direction. In both cases, the efficiency didn't change by more than 3% in absolute value compared with original results, which could be due to differences in the alignment precision. Another thing we have tried is doubling the separation between the field plates to 12 mm, keeping

the atomic beam in the center of the gap. Accordingly, we also doubled the DC offest on the field plates to keep the actual electric field fixed. We were a little worried about the interaction between the Rydberg atoms and the field plates, but the results did not change. The STIRAP efficiency has no dependence on the distances from the atomic beam to the field plates. Finally, we attached several power resistors on both the top and bottom field plates to heat up the plates and increase their blackbody radiation rate. We went up to 370 K from room temperature, we didn't see any change on the STIRAP efficiency although the ion signals increased significantly. So blackbody radiation is not a problem in limiting STIRAP efficiency.

5.4 STIRAP Efficiencies for Different n

After we studied the $n = 24$ states extensively and could not get the raw STIRAP efficiency higher than 50%, we went to other n states with n ranging from 12 to 30 and even in the 50s. With higher n, the decay rates go down so the correction for decay is not as important. But in the meantime, the relative Rabi frequencies for the Stokes light also go down, we might not have enough red light intensity, especially for transitions to the manifolds.

5.4.1 States on the Manifolds

We used STIRAP to excite He* atoms to Stark manifolds with different n values. Table 5.2 shows some of the results. As I discussed in Section 1.2.3, on each manifold, different states have different transition strength, so if the Rabi frequency is not highly saturated, we do see different STIRAP efficiencies. We searched extensively on each manifold and the results shown in Table 5.2 yield the best measured efficiencies for red light power of 550 mW

and blue light power of 50 mW.

n value	wavelength (nm)	DC voltage (Volts)	raw efficiency (error:$\pm 1.5\%$)
12	834.4395	20.0	35.2%
13	826.6702	30.0	47.1%
14	820.6048	25.2	53.2%
15	815.7697	15.3	55.4%
16	811.8620	20.5	55.5%
17	808.6453	15.5	55.2%
18	805.9793	26.9	48.9%
20	801.8203	13.8	47.0%
24	796.4603	5.5	39.1%
30	792.1369	4.0	13.4%

Table 5.2: Measured STIRAP efficiencies on the manifolds of different n states.

For $n = 15 \sim 17$, the measured efficiencies are around 55%, the highest we have ever achieved. Using $n = 16$ for example, we measured the decay rate of the Rydberg state back to the ground state by moving the bichromatic deflection beam further away from the STIRAP beams. This time delay allowed some of the Rydberg atoms to decay back to the metastable state, causing the measured efficiency to be lower than the real value. The decay curve for the $n = 16$ manifold (with electric field at 34.3 V/cm and red light wavelength at 811.8620 nm) is shown in Figure 5.11. The "lifetime" is about 19.1 μs, corresponding to 20.4 mm travelling distance on average for the atoms. If we take the distance between the peak of the blue light and the center of the bichromatic beam, approximately 4.5 mm, as the decay length, then the real STIRAP efficiency is shown where the fitted exponential curve is at -4.5 mm. This value is $\sim 67.7\%$ as seen in Figure 5.11.

It is a little surprising that for the $n = 12$ manifold, the measured efficiency is considerably
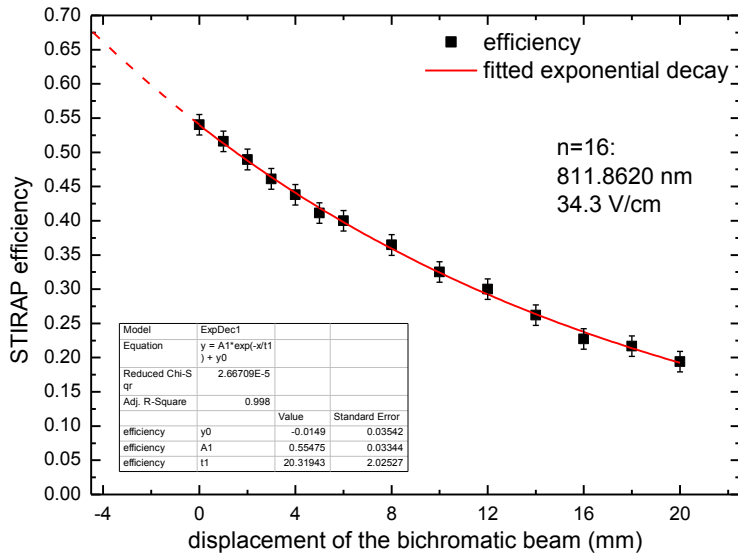
Figure 5.11: Decay from the $n = 16$ manifold state back to metastable states, measured by moving bichromatic beam further and further away from the STIRAP interaction region, $\lambda = 811.8620$ nm, E = 36.8 V/cm
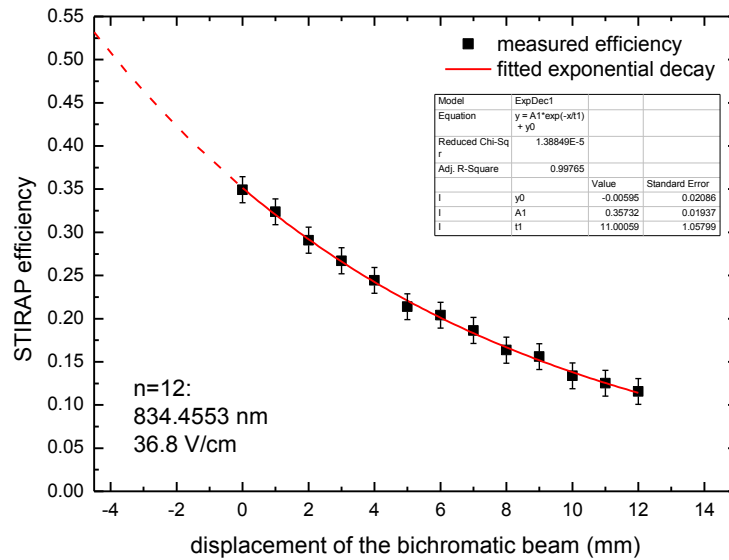
Figure 5.12: Decay from the $n = 12$ manifold state back to metastable states, measured by moving bichromatic beam further and further away from the STIRAP interaction region, $\lambda = 834.4553$ nm, E = 34.3V/cm
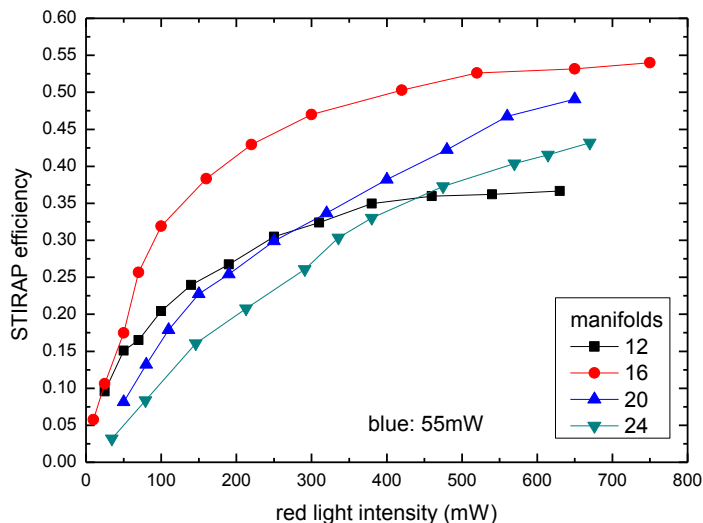
Figure 5.13: Measured STIRAP efficiency vs. red light power for excitation to manifold states for $n = 12, 16, 20$ and 24.

lower. One possible reason could be its faster decay rate. So we measured the decay curve for the $n = 12$ manifold as well and plotted the results in Figure 5.12. The measured characteristic decaying distance is about 11.0 mm, corresponding to a "lifetime" of 10.3 μs because atoms are moving with an average velocity of 1070 m/s. The raw efficiency at the position closest to the blue light is $35.2\% \pm 1.5\%$. If we add the -4.5 mm back for the correction, we get an efficiency of $\sim 53.2\%$ as shown in Figure 5.12, which is still smaller than the efficiency for the $n = 16$ manifold. And moreover, the red light Rabi frequency for $n = 12$ should be higher than that for higher n's. So the lower efficiency remains a mystery.

For higher n states, the efficiencies are also smaller despite their smaller decay rate. It is possible that our Rabi frequencies for higher n's are not high enough, especially for the manifold. We therefore measured the STIRAP efficiencies vs. red light power, with blue light power at 55 mW, for $n = 12, 16, 20$ and 24. The results are shown in figure 5.13, where it is very clear that the red light intensity is much more saturated for $n = 12$ and 16. For n

98
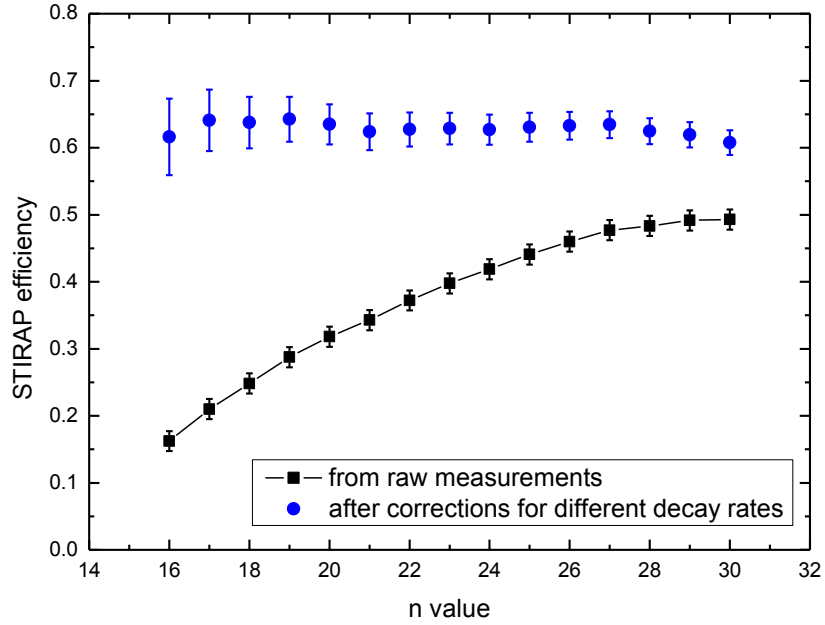
Figure 5.14: STIRAP efficiency for excitation to different n^3S_1 states, n = 16 - 30. Black squares are from raw measurements and blue dots are corrected for different decay rates.

= 20 and 24, we need more red light power to improve STIRAP efficiencies. This also could explain why, at the $n = 30$ manifold, we have a STIRAP efficiency of only 13.4%.

5.4.2 n^3S_1 States

We also measured the STIRAP efficiency at different n^3S_1 levels at zero electric field, with all other parameters, such as the red/blue light intensities, beam sizes, relative overlapping positions, etc., the same. The red and blue light intensities were 900 mW and 50 mW respectively. The results are shown in Figure 5.4 as the black square points. The efficiency behavior is different from the case for the manifold states. While n increases, the measured raw STIRAP efficiency tends to saturate at about 50%. With lower n, the efficiency is significantly lower. For example for the 16^3S_1 state, the STIRAP efficiency is only 16%.

However, these data marked as the square points are not corrected for different decay rates. Atoms in lower lying nS states decay a lot faster to the metastable states, making our measured efficiencies a lot smaller than the actual excitation rate. We corrected the measured raw data with their respective radiative lifetimes (as obtained from [81]) for the decaying distance of 4.5 mm, and the results are also shown in Figure 5.14 as the blue circles. The absolute uncertainties of each measurement are the same $\sim \pm 1.5\%$, but the larger correction factors for smaller n's lead to larger uncertainties for the corrected efficiencies. From Figure 5.14, we know that STIRAP efficiencies for different nS states are roughly the same, $\sim 63\%$, which is different from the case for the manifold states. The red light Rabi frequencies are highly saturated for all states, so essentially there is no difference for different n states in the STIRAP process.

Overall, raw measurements on manifolds and S states show totally different behavior for different n values. For lower n, e.g. 16, raw STIRAP efficiency is a lot better on the manifolds than on the S state. For intermediate n values, around 24, we have comparable efficiencies on the manifolds and the S states. But for higher n, >30, the S state is much better than all the manifold states. Decay rates and red light Rabi frequencies are definitely two important and also correlated factors. However, for states with high enough red light Rabi frequency, even after correction for radiative decay, we could not get an efficiency higher than 70%. There might be some other limiting factors. It will require further investigation to determine what they are.

Chapter 6

Rydberg Atom Detection

6.1   Introduction

Detection of Rydberg atoms is almost always by ionization since these highly excited states are quite weakly bound and ionization is easy. In the last 30 years, many radiation sources have been used to study the ionization mechanisms of Rydberg atoms. The physical mechanism of ionization depends on the radiation frequency. For very low frequency, the field amplitude determines the ionization, the so-called field ionization, while for higher frequencies the photon energy is most critical [83]. If the radiation frequency is on resonance with the atom ionization energy, the ionization rate is enhanced significantly. For Rydberg atoms, a microwave field or just black-body radiation (thermal photoionization) are enough to produce photoionization. Collisions with other Rydberg atoms or metastable atoms are also very likely to ionize Rydberg atoms. If Rydberg atoms are too close to each other, one atom's electron can drop to a more deeply bound level while the other atom's electron is ionized [84]. Metastable atoms carry a very high internal energy and can thus collisionally ionize any atom whose ionization energy is smaller than the internal energy of the metastables

in a process called Penning ionization [85]. Overall, any of these mechanisms could possibly contribute to ionization of Rydberg atoms, but their rates might be a lot different, so we need to make a concrete analysis of the specific conditions.

As I showed earlier in Figure 2.4, we have an ion detector downstream of the interaction region above the field plates monitoring the Rydberg ions. But it wasn't clear initially what was causing the ionization in our system. In order to determine this, we have done many different experiments. According to the results, we have ruled out all other mechanisms, and we believe the observed signals are produced by blackbody ionization at the ambient room temperature (~ 300 K) at a very low rate, but nonetheless sufficient to ionize about 1% of the atoms in a region viewed by our detector. The ionization process is a mixture of a single step photoionization or diffusion among Rydberg states, but always driven by the local thermal radiation field. This low blackbody ionization rate also agrees with theoretical expectations.

6.2   Rydberg-Stark Spectroscopy

Based on the ion signals, we have made Stark maps of the energy level structures of helium in a weak field below 170 V/cm, such as shown in Figure 6.1 for $n = 24$. This was done in the center of the field plates to keep a uniform electric field, and by fixing the frequency of the $\lambda = 785 \sim 820$ nm laser while scanning the voltage across the plates. (We can also fix the voltage and scan the red laser frequency.) We did not make careful Stark maps for all the n-states, but we can easily resolve the S-states from the manifold of other l states because of their significant quantum defects. We can also resolve the D-state at zero field because the resulting splitting is a few hundred MHz.

In Figure 6.1, the dots are our experimental results and the dashed lines are from the
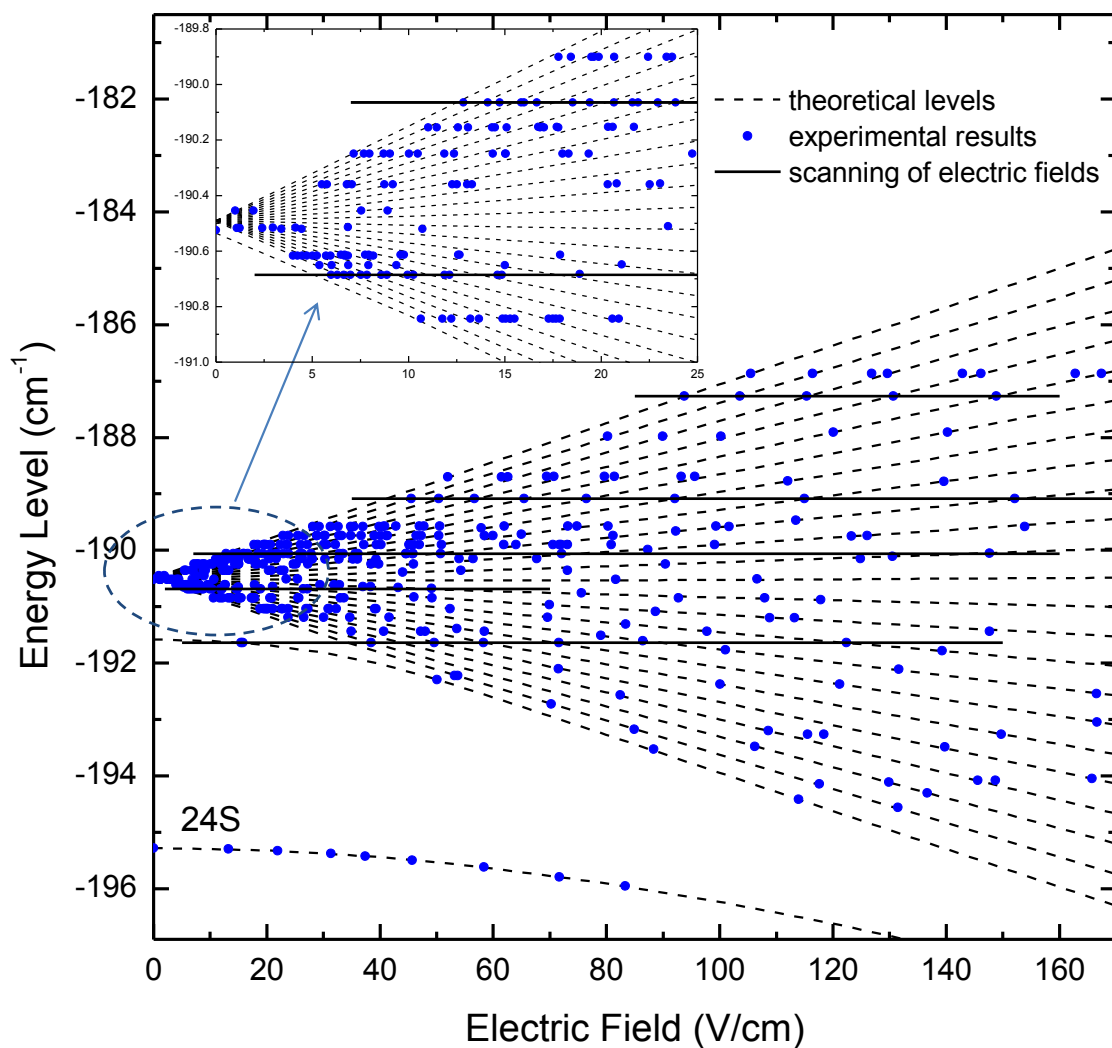
Figure 6.1: Stark map on the n = 24 Rydberg states. The dots are our experimental results, the dashed lines are the theoretical calculations done by Prof. Tom Bergeman, and the solid horizontal lines represent the scanning of the electric fields.

theoretical calculations done by Prof. Tom Bergeman for $n = 24$. The overlap is excellent, so we know exactly where we are on the Stark maps. We also show the scanning of the electric fields as the solid horizontal lines. When a scan crossed an energy level, we could see an ion signal peak from our ion detector on the oscilloscope. Of course the peak sizes depended on the excitation efficiencies and also the ionization rates. But the positions of these peaks are determined only by the Stark effect. The error bars of our measurements in the energy axis are typically less than 600 MHz, i.e. 0.02 cm^{-1}, which includes the uncertainty of the reading on our wavemeter and the Doppler detuning due to deviation of the laser beams from absolute perpendicularity to the atomic beam. The uncertainties of the electric field are only from measurements of the separation between the field plates and the voltage reading, typically within 2%. Overall the error bars of our measurements are less than the dot sizes on the figure so are not included.

At very low electric field, the data points are very close to each other, so we zoomed into this region as shown in the inset. The agreement at low field might be not quite as good as at higher field because there is some earth's magnetic field mixing up the electric field, so the z axis is not well defined. In some regions, there are two dots very close to each other due to the fine structure splitting for both $m_J = 0$ and ± 1. The theoretical lines shown here are from a simplified picture which ignores the L-S coupling.

6.3 Testing the Ionization Mechanism

6.3.1 Decay of the Ion signals

The ions we collect are mostly the ones ionized right below the ion detector, not the total number of ions along the flight path. Ions formed before the detector would curve and

collide on to the field plates with even very weak electric fields. For example, with an electric field of 1 V/cm, it takes atoms just 1.6 μs to travel vertically from the middle between the field plates to one of the field plates. In other words, ions fly only ~ 1.7 mm along the beam direction before they collide with the field plates. So by measuring the relative change of the ion signal peak while moving the interaction region further away from the ion detector, we could get a sense of the ionization rate along the flight path of the atoms. We have observed several individual Stark peaks as a function of distance between the STIRAP region and ion detector, and have measured the variation of their strength from their radiative decay. Figure 6.2 shows typical sets of data for the 24^3S and 30^3S state with electric field ~ 0.2 V/cm.

The red and the blue light are reflected by mirrors on the same big translation stage and on top of that, the blue light is on another small stage. The horizontal axis corresponds to position of the big stage. For each big stage step, the relative position of the red and blue beams are optimized for the best STIRAP signal.

The ion signal decreases as the interaction region is moved further upstream, because we have fewer Rydberg atoms due to radiative decay. The measured curves fit well with an exponential decay function, showing characteristic traveling distances of 17.6 mm for 24^3S and 35.7 mm for 30^3S, which correspond to average "decay lifetimes" of 16.4 μs and 33.4 μs respectively. These are a little longer than the theoretical radiative lifetimes for Helium, 10.4 μs for 24^3S and 20.1 μs 30^3S [81], because thermal-induced depopulation competes with spontaneous decays. As a result, a fraction of the atoms are redistributed to some nearby states that have larger ionization rate, making the observed ion signals decay slower. We also measured the decay rates of Rydberg S states to the metastable state by changing the 1083 nm deflection light position (efficiency decay curve), and they turned out to be very close to the theoretical radiative decay rates, suggesting that redistribution to longer lifetime states

105

The figure contains the following fitted-parameter tables.

30S fit table:

Model	ExpDec1		
Equation	y = A1*exp(-x/t1) + y0		
Reduced Chi-Sqr	6.20759E-4		
Adj. R-Square	0.98147		
		Value	Standard Error
C	y0	0.01047	0.18408
C	A1	0.97469	0.17408
C	t1	35.67494	10.23763

24S fit table:

Model	ExpDec1		
Equation	y = A1*exp(-x/t1) + y0		
Reduced Chi-Sqr	4.41707E-4		
Adj. R-Square	0.99295		
		Value	Standard Error
E	y0	0.01789	0.05435
E	A1	0.98991	0.04792
E	t1	17.57952	1.93942

Figure 6.2: Distance dependence of signal strength for 24^3S and 30^3S state with the detector sitting right above the mini-holes. For each data point, the relative position of the red and blue beams was optimized for the best STIRAP signal. Each set of points is fitted with an exponential curve.

is at a low rate and therefore not the reason for the slow ion signal decay. Anyway, from this we conclude that the ionization rate of the process that produces our signal is much slower than the radiative decay lifetime of the state.

6.3.2 Field Ionization

In order to qualitatively measure the ionization rate in our system, we wanted to compare it with the field ionization rate. Field ionization is convenient as the ionization threshold scales as $\sim 16/n^4$. States with $n = 24$ can be field ionized around 900 V/cm.

We couldn't do field ionization with our typical setup because the detector was outside - downstream - of the field plates. So we replaced the upper field plate with an Al piece with a series of about 30 small holes at the center with diameter ~ 0.5 mm, typically separated by 4 mm from each other in a hexagonal array. The ion detector was placed directly above the small holes to detect ions that came through them. When the voltage was high so that the field between the plates could ionize the spectroscopically selected Rydberg states, the signal was very strong if the laser excitation region was directly below a hole. It vanished if it was moved 0.5 mm away, which means pretty much all the atoms were immediately ionized after they were excited to the Rydberg states. If excitation happens before the holes, then field ionization leaves no Rydberg atoms to be ionized by the mysterious ionization process in regions below the holes and therefore nothing gets to the detector. We could map out the position of the holes by moving the excitation region. As soon as we dropped the field below the ionization threshold, there was a weak signal that did not depend much on the position of the exciting laser beams. This signal was smaller than when the ion detector was outside the field plates, because the holes pass fewer ions.

For field ionization, we are on the continuum of the Stark map, so the STIRAP efficiencies are always low (typical $< 5\%$, best $< 20\%$). To compare the field ionization rate above threshold and the mysterious ionization rate at low electric field, we divided the ion signal by the STIRAP efficiency and the resulting rate for field ionization is about 20 times higher. This showed us that the strength of the ionization signal we usually detect represented only a small fraction of the Rydberg state population.

We did the field ionization tests for a few different n values. The threshold is ~ 2930 V/cm for $n = 18$, ~ 940 V/cm for $n = 24$, ~ 390 V/cm for $n = 30$ and only ~ 25V/cm for $n = 60$, which agrees well with the classical ionization limit, $5 \times 10^9 / 16 n^4$ V/cm. This direct field ionization corroborated our spectroscopic measurements because we could identify the

states we chose to excite by their field ionization threshold as well as their optical frequency.

6.3.3 Ion Counts

As I have described earlier in the previous chapter, the metastable He* flux is $\sim 3\times10^8$ atoms/s through the rectangular aperture. If we could count the total ion number, also based on the STIRAP excitation efficiency measurements, we can easily calculate our Rydberg-atom ionization rate. The ion counts were measured in two different ways using the detector set around the edge of the field plates. First, we estimated the ion rate from the current out from the ion detector and the gain of the two MCPs. To get a better idea, we sent the ion detector signal directly to a counter. Those two results agreed well with each other.

From the ion detector, we could see single pulses of width about 5 ns and amplitude about 3.5 mV with the oscilloscope. We used 50 Ω coupling while 750 V / 800 V were supplied across each of the two separate MCPs. This tells us that the total MCPs gain is $\sim$ 2.2 $\times10^6$ ($\frac{3.5mW/50\Omega\times5ns}{1.6\times10^{-19}Coulomb}$), which is also consistent with the MCP specifications provided by Photonis, Inc, gain of $\sim 10^3$ at 750 V and $\sim2\times10^3$ at 800 V. When we monitor ion signals on the oscilloscope using 1.25 MΩ to convert it to a voltage and a pre-amplifier with gain of 20, the typical signal is about 1 V for the $24S$ state, which corresponds to an absolute current of 40 nA. Then the ion counts could be calculated as 40 nA/(2.2$\times10^6$)/(1.6 $\times 10^{-19}$ Coulomb), i.e. $\sim 1.1\times10^5$ /s.

In the other way, since each ion generates a single pulse of 5 ns, we sent the signal from the ion detector to a PRE Amp (ORTEC mode 113) and a multimode amplifier (ORTEC mode 410), then to a 50 MHz counter (HP 5302A) to directly count the total pulse rate. The result we got for the ion flux rate is $\sim 10^5$ /s for the $24S$ state. For different levels and different excitation efficiencies, the rates could vary, but generally, they agree very well with

our estimates.

The ions were counted with our ion detector sitting downstream, outside of the field plates, and the STIRAP region was located about 35 mm away from the edge of the field plates to avoid the penetrating electric field from the ion detector. From the measured ion signal decay curve of $24S$ in Figure 6.2, this is only 15% of the number if the ion detector is right after the interaction region. So after this correction for decay, the ion count for the $24S$ state should be $\sim 6.7 \times 10^5$ /s. Considering the total He* flux is $\sim 3\times 10^8$ atoms/s and the STIRAP excitation rate is $30\% \sim 50\%$, the ionization rate is approximately 0.6% in our detection region.

We also used the same methods to count the rate of the metastable He atoms, which are deflected out of the original beam by 1083 nm light. The signal was measured by the SSD at the end of the beam line in the detection chamber, and there is a 2 mm wide vertical slit in front of the SSD. While moving the detector horizontally, the peak flux rate we got is about 2×10^6 /s. The direct count and the derivation from the current out of the SSD agreed with each other. Considering the broad distribution of the deflected metastable atoms, the metastable flux passing through the slit is about 10% of the total amount. Furthermore, the efficiency of the SSD is about 70%, so the estimated metastable count is about 3×10^7 /s. This is lower than what we expected. Possible reasons for that are: a. 1083 nm deflection is not very effective; b. MCPs were not good at certain region, we only measured a small fraction of the total amount; c. We lost a lot of metastable atoms during the long beam path.

6.3.4 Numerical Estimates of the Ionization Rate

We now estimate both the collisional ionization rate and the blackbody ionization rate in order to compare the results with our experimental values.

The collisional ionization rate will be calculated first. Based on Robicheaux's paper about Penning ionization of Rydberg states [84], we can estimate that the cross section of Rydberg-Rydberg Penning ionization is roughly $\sigma \sim \pi \times (4n^2 a_0)^2$, which yields $\sigma \sim 4.4 \times 10^{-10}$ cm^2 for $n \sim 24$. If we take 3×10^4 cm/s as the relative thermal speed of the atoms in the beam, it gives us a volume collision rate $\sim 1.3 \times 10^{-5}$ cm^3/s. This is a high rate, but our density is very low, $\sim 1.4 \times 10^5$ cm^{-3} for metastable He* and $\sim 0.7 \times 10^5$ cm^{-3} for He Rydberg states (using 50% as the STIRAP efficiency). So the ionization rate (density $\times$ volume collision rate) is $\sim$ 0.9 Hz. Thus, we would expect ionization of 9×10^{-6} of our beam flux along each cm of the beam (10 μs time duration). Since the Ryberg beam flux is estimated to be half of He* flux $\sim 1.5 \times 10^8$ /s, the corresponding ion rate is $\sim 1.35 \times 10^3$ ions/s for each cm of length. Since our ion detector could well collect ions from 1.5 cm of beam length, we might expect a count rate of $\sim 2 \times 10^3$ /s from such collisions. In fact, we typically have an ion count rate about 6.7×10^5 /s after the correction for decay, more than two orders of magnitude higher. So we conclude Rydberg-Rydberg collisions are not relevant to our ionization process. Here we used the relative velocity of the atoms to calculate the ionization rate, because Penning ionization with zero relative velocity would be much less likely due to the low Rydberg density.

The metastable-Rydberg collision cross section is even two orders of magnitude smaller than the Rydberg-Rydberg collision cross section, so it can also be ruled out. Although the density of background Helium atoms is five or six orders of magnitude higher, they move slowly compared to the electron velocity in the Rydberg state; thus, transition probability from Rydberg-ground He collision is expected to be very small because the electron wave

n	$24S - nP$ transition rates (1/s)	nP ionization rates (1/s)
20	1127.8	1386.5
21	1726.2	1410.7
22	3135.2	1420.6
23	9337.3	1419.0
24	3762.4	1408.3
25	142.6	1390.3
26	133.4	1366.8
27	101.7	1339.2
28	78.1	1308.5
29	61.4	1275.7

Table 6.1: Transition rates for $24S \to n$P and ionization rate for np states at T $= 300$ K [data from Glukhov et al through private communications].

function will adiabatically deform, as we were advised by Robicheaux. These estimates further confirm that collisions are also not the cause of our low STIRAP efficiency, because the collision rate is too low.

On the other hand, according to Glukhov et al's calculation [86][87], the rate of direct blackbody radiation for $n = 24$ is 299.4 /s, which means in 15 μs, 0.45% of the atoms in $24S$ state will be ionized by blackbody radiation. For the $24D$ states, the rate of direct blackbody radiation is 1535.8 /s, so that the fraction of ionized atoms in $24D$ state is 2.3%. (Some of these numbers are not listed in their papers, but were privately communicated by the authors).

Blackbody radiation causes not only direct photoionization of the initially populated Rydberg levels, but also induces transitions between neighboring Rydberg states, thus leading to population redistribution. Therefore multi-step ionization also occurs [26]. For example, the $24S$ state in triplet He may be ionized as follows: $24S \to nP \to$ continuum. Taking into account $n = 20 \sim 29$ in P-series, rates for transition from $24S$ to nP ($n = 20{\sim}29$) and p-states ionization rates at T $= 300$ K are listed in Table 6.1.

By adding all possible paths together, within 15 μs, the total two-step ionization rate is approximately 0.62%. Similarly, the probability for a two-step ionization for 24D is 0.1%. The three-step ionization process is not significant because the time dependence of the optimized process is $(t/3)^3$, so higher orders of stepwise ionization become vanishingly small. The total probability of blackbody radiation ionization at T = 300 K for the 24S state in triplet helium is roughly the sum of direct and two-step ionization rates, 0.45%+0.62%=1.07%. For 24D, this sum is 0.1%+2.3%=2.4%. These rates also explain why we typically have a larger ion signal on the manifolds of the Stark map than on the S states, even with the same STIRAP efficiency.

The blackbody radiation rate seems to be reasonably close to our experimental result, while the Penning ionization rate is two or three orders of magnitude smaller, so we basically narrow down our hypothesis for the mechanism for ionization to blackbody radiation. In the next section, we report further experiments to confirm this hypothesis.

6.4   Testing the Blackbody Radiation Hypothesis

6.4.1   Increasing Radiation Temperature

The most direct way to test the blackbody radiation hypothesis is to increase the temperature in the interaction chamber. We heated up the field plates by attaching (with good thermal contact) four power resistors (each 25W) in series onto each of the Al field plates. The temperature of the resistors and the field plates was varied by changing the current through the resistors. A thermocouple gauge (Nickel-Chromium vs. Nickel Aluminum) was used to measure the temperature by making contact with one of the resistors. The real temperature is proportional to the voltage offset across the thermocouple, -0.023 mV at zero
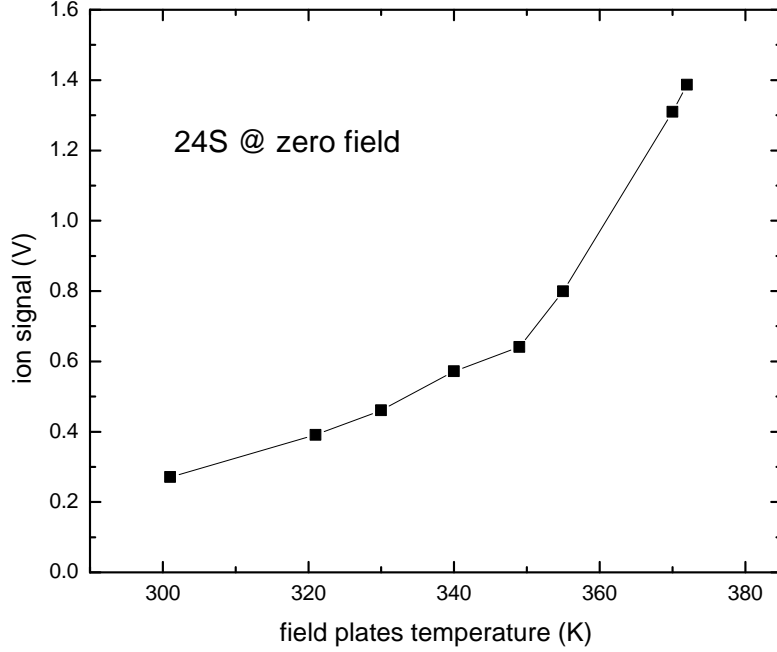
Figure 6.3: Change of the ion signal amplitude with field plate temperature. This confirms the increase of ionization rate with increasing blackbody radiation intensity.

^{0}C and 2.27 mV at 100 ^{0}C. As shown in Figure 6.3, for the 24S state at zero electric field, the ion signal increased significantly with higher plate temperature. Since, with increasing temperature, only the blackbody radiation is increasing, this must be the significant mechanism. Ion signals for other Rydberg states showed similar behaviors.

Since the temperature was measured on one of the power resistors, which is different from the actual temperature of the plates, and also since the radiation region is not a closed space, Figure 6.3 does not provide accurate quantitative results. However, qualitatively, it proves that higher temperature raises the ionization rate and the ion signal we typically see results from blackbody radiation.
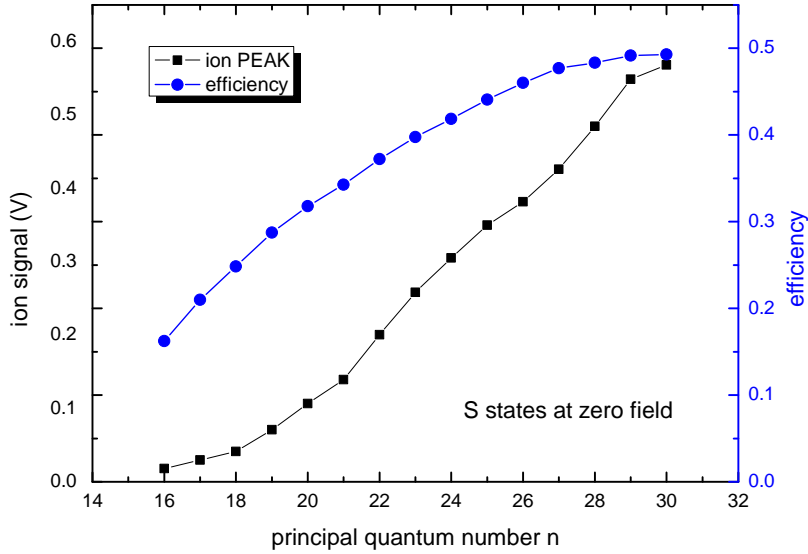
Figure 6.4: Ion signal peak strengths and also the STIRAP excitation efficiencies for nS states with principal quantum number n ranging from 16 to 30.

6.4.2 Ion Signals for nS States

The n dependence of the total blackbody ionization rate has also been calculated in some recent papers [88][87]. It was shown that at about 300 K, there is an increase from $n \sim 10$ to 18 and then the rate is basically flat from $n = 18$ to 30. In order to compare the ionization rates for different n, we measured the ion signals for nS states and their corresponding STIRAP excitation rate at room temperature, as shown in Figure 6.4.

Both the efficiency measurements and the ion signal sizes are not corrected for the related decay rate (see Section 6.3.1). Since the decay rates for the efficiency measurements are a little smaller than the ion signal decay rates and the decay region is also a lot shorter, 4 mm compared to 35 mm, here I will only consider the corrections for the ionization signals.

The measured ion signal N_I should be proportional to $\sigma_n \times \rho_n \times exp(-d/r_n)$, where σ_n is the ionization rate, ρ_n is the STIRAP excitation rate, d is the distance between the laser
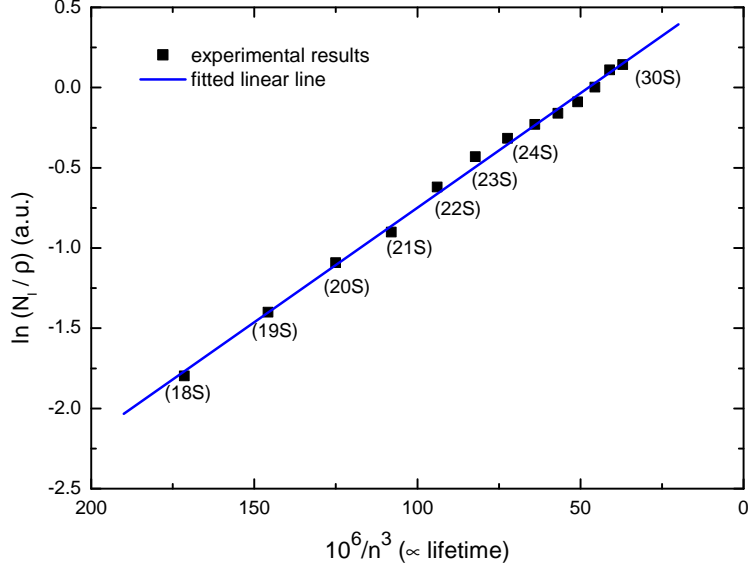
Figure 6.5: $ln(N_I/\rho)$ vs $1/n^3$ for nS with $n \sim 18$ - 30, where N_I is the measured ion signal, ρ_n is the STIRAP excitation rate. The points are from our measurements as shown in Figure 6.4, and the solid line is a linear fit.

beams and the ion detector which is the same for every n, and r_n is the average traveling distance corresponding to the n-dependent decaying lifetime. If it is true that the ionization rate σ_n is constant, then $ln(N_I/\rho) \propto 1/r_n$ should be satisfied. The decay lifetimes here are a little different from the theoretical spontaneous decay lifetime, but are roughly $\propto n^3$, thus $1/r_n \propto 1/n^3$. In Figure 6.5, we plotted $ln(N_I/\rho)$ vs $1/n^3$ for $n \sim 18$ - 30 and fitted the data with a straight line. As we can see, it fits well for n ~ 18 - 30. The deviation from the straight line is actually the change of log(ionization rate). This behavior agrees well with the theoretical blackbody ionization rates. This would not be the case if the ion signals were not due to blackbody ionization.

6.5   Suppressing Collisional Ionization

In order to confirm that collisional ionization is not a contributing factor to our ion signals, we changed the metastable helium density and background pressure by changing the source parameters.

Raising the source voltage raises the discharge current, producing more metastable He atoms, and also more UV photons (Figure 5.9(a)). The efficiency of STIRAP under these conditions remains the same (Figure 5.9 (b)). So the ion signal size divided by He* count could be referred to as the relative ionization rate. As seen in figure 6.6, with source voltage increasing from 1300 V to 2900 V, the relative He* count increased by $\sim$ 2.2 times and the resulting ion signal increased by $\sim$ 2.1 times, i.e. the size of the ion signal is almost directly proportional to the He* count. We can then conclude that the ionization rate is almost constant, independent of the He* density, which confirms that neither He*- Rydberg nor Rydberg-Rydberg collisions are responsible for the Rydberg ionization, because otherwise the ionization rate would increase with higher He* density. Similarly, UV photons have nothing to do with the ionization mechanism either.

Raising the source flow pressure leads to more ground state He and less metastable atoms in the interaction region while STIRAP efficiency remains constant (Figure 5.10). With source outlet pressure increasing from $\sim$ 2.00 Torr to $\sim$ 4.10 Torr, both the relative He* count and the ion counts decreased by $\sim$ 50%, while the background pressure in the interaction chamber went up from 0.80×10^{-6} Torr to 1.23×10^{-6} Torr, as shown in Figure 6.7. The ion signals changed roughly in the same rate as the metastable atom counts, i.e. the ionization rate is roughly constant, which tells us that our ionization is not caused by collisions with ground state Helium. If it was, after the He* density has been accounted for, the ionization rate would increase with higher He flow.
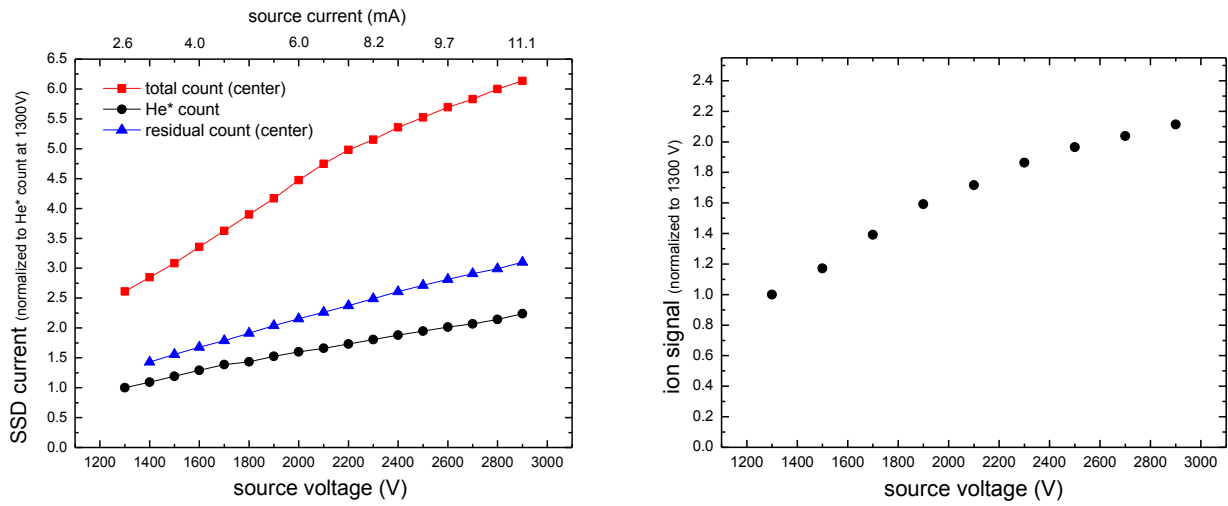
Figure 6.6: We changed the density of the He* by adjusting the source current, the resulting ion signal size is almost proportional to the He* count, i.e. ionization rate is independent of He* density.
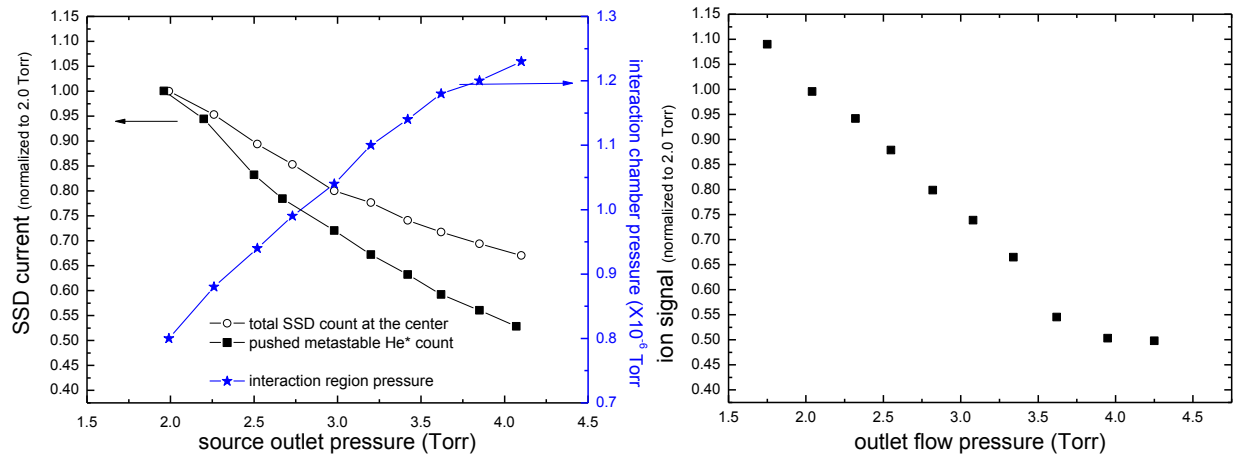
Figure 6.7: By changing the source flow pressure, we increased the density of ground state He but reduced the He* density. The ion signal size is roughly linear with He* count, i.e. ionization rate has no dependence on background He flux.

We increased the background pressure in the interaction chamber by reducing our pumping rate. We didn't see any increase in the ion signal amplitude. Instead, increased pressure resulted in a reduced ion signal due to a drop in the number of metastable atoms.

In conclusion, we are very confident that collisional ionization is not the source of our ion signals. Blackbody radiation ionizes Rydberg atoms with a rate $\sim 1\%$ in the region viewed by our ion detector.

Chapter 7

Conclusions

In order to excite all helium atoms to high-lying Rydberg states for focusing with an inhomogeneous electric field, we used STIRAP, a process that excites atoms in a counter-intuitive order and could have a theoretical efficiency of 100%. This is done at a tunable DC electric field with the pump light of $\lambda = 389$ nm connecting the metastable 2^3S state atoms to the 3^3P states and the Stokes light of $\lambda = 792 \sim 830$ nm coupling the 3^3P states to the Rydberg states. We demonstrated that with an optimized delay of pump light after the Stokes light, we typically have about 3 times higher Rydberg production as compared to the overlapping case. We have also examined the Stark spectrum of different Rydberg states for helium. The experimental results showed superb overlap with theoretical calculations. So we know exactly where we are on the Stark map when we do the STIRAP excitation.

To measure the absolute excitation efficiency of STIRAP, we employed a scheme based on the strong bichromatic force on the 2^3S_1 to 2^3P_2 transition at $\lambda = 1083$ nm. About ~ 2.5 mm downstream of the STIRAP beams, we deflect the remaining 2^3S_1 atoms out of the beam and the ratio of this signal measured with STIRAP beam on and off provides an absolute quantitative measure of our STIRAP efficiency. Our raw measurements are

typically around 50% efficiency, and vary with both n and l of the Rydberg states. On one hand, different states have different transition strengths and thus different Rabi frequencies for the Stokes light. On the other hand, those states with high transition strength typically decay faster, making our measured efficiency lower than the actual excitation rate. For states with high enough Rabi frequencies, after correction for the decay, the highest efficiencies are around 70%. For some states, the efficiencies are a bit lower, and the reasons are still under investigation.

We have also done many measurements to determine the ionization mechanism of atoms in Rydberg states in our system. We believe that the observed ion signals are produced by black-body ionization at a very low rate, but sufficient to ionize about $0.5 \sim 1.0$ % of the atoms in a region viewed by our detector. This is in very good agreement with some recent theoretical papers.

In the future, an electrostatic lens will be applied to manipulate the trajectories of Rydberg helium atoms. Although a focussing effect with a hexapole lens has been demonstrated in previous theses, major improvements are needed. A more complicated electrostatic lens or some feedback algorithm could be used to move the focal point of the lens. Furthermore, bichromatic collimation and optical molasses could be applied to reduce the transverse velocity of the thermal beam produced by our source. The focusing might be more efficient with precollimated beam. Beyond that, the He* atomic beam can be used to do neutral atom lithography, where the focused He* atoms are used to expose a suitable resist material.

Bibliography

[1] Otto Stern. Bending a molecular ray by crystal lattice face. *Naturwissenschaften*, 17: 391–391, 1929. ISSN 0028-1042. 10.1007/BF01506798.

[2] B. Friedrich and D. Herschbach. Stern and Gerlach: How a bad cigar helped reorient atomic physics. *Physics Today*, 56:53–59, 2003.

[3] I. Estermann. History of molecular beam research: Personal reminiscences of the important evolutionary period 1919-1933. *Am. J. Phys*, 43:661–671, 1975.

[4] T. W. Hänsch and A. L. Schawlow. Cooling of gases by laser radiation. *Optics Communications*, 13(1):68–69, Jan. 1975.

[5] H. J. Metcalf and P. van der Straten. *Laser Cooling and Trapping*. Springer, Berlin, 2002.

[6] D. S. Hall. Resource Letter: BEC-1: Bose-Einstein condensates in trapped dilute gases. *Am. J. Phys.*, 71(7):649–660, 2003.

[7] Richard J. Cook and Richard K. Hill. An electromagnetic mirror for neutral atoms. *Optics Communications*, 43(4):258–260, Oct. 1982.

[8] Philip E. Moskowitz, Phillip L. Gould, Susan R. Atlas, and David E. Pritchard. Diffraction of an atomic beam by standing-wave radiation. *Phys. Rev. Lett.*, 51(5):370–373, Aug 1983.

[9] Peter J. Martin, Bruce G. Oldaker, Andrew H. Miklich, and David E. Pritchard. Bragg scattering of atoms from a standing light wave. *Phys. Rev. Lett.*, 60(6):515–518, Feb 1988.

[10] J. J. Berkhout, O. J. Luiten, I. D. Setija, T. W. Hijmans, T. Mizusaki, and J. T. M. Walraven. Quantum reflection: Focusing of hydrogen atoms with a concave mirror. *Phys. Rev. Lett.*, 63(16):1689–1692, Oct 1989.

[11] Gregg M. Gallatin and Phillip L. Gould. Laser focusing of atomic beams. *J. Opt. Soc. Am. B*, 8(3):502–508, March 1991.

[12] J. L. Cohen, B. Dubetsky, and P. R. Berman. Atom focusing by far-detuned and resonant standing wave fields: Thin-lens regime. *Phys. Rev. A*, 60(6):4886–4901, Dec 1999.

[13] R. B. Doak, R. E. Grisenti, S. Rehbein, G. Schmahl, J. P. Toennies, and Ch. Wöll. Towards realization of an atomic de Broglie microscope: helium atom focusing using Fresnel zoneplates. *Phys. Rev. Lett.*, 83(21):4229–4232, Nov 1999.

[14] Heung-Ryoul Noh, Kazuko Shimizu, and Fujio Shimizu. Imaging of an atomic beam with electrostatic lenses. *Phys. Rev. A*, 61(4):041601, Feb 2000.

[15] Juris G. Kalnins, Jason M. Amini, and Harvey Gould. Focusing a fountain of neutral cesium atoms with an electrostatic lens triplet. *Phys. Rev. A*, 72(4):043406, Oct 2005.

[16] Thomas Breeden and Harold Metcalf. Stark acceleration of Rydberg atoms in inhomogeneous electric fields. *Phys. Rev. Lett.*, 47(24):1726–1729, Dec 1981.

[17] K. Bergmann, H. Theuer, and B. W. Shore. Coherent population transfer among quantum states of atoms and molecules. *Rev. Mod. Phys.*, 70(3):1003, 1998.

[18] U. Gaubatz, P. Rudecki, M. Becker, S. Schiemann, M. Külz, and K. Bergmann. Population switching between vibrational levels in molecular beams. *Chem. Phys. Lett.*, 149 (5,6):463–468, Sept. 1988.

[19] B. Broers, H. B. van Linden van den Heuvell, and L. D. Noordam. Efficient population transfer in a three-level ladder system by frequency-swept ultrashort laser pulses. *Phys. Rev. Lett.*, 69(14):2062–2065, Oct 1992.

[20] A. Lindinger, M. Verbeek, and H. G. Rubahn. Adiabatic population transfer by acousto-optically modulated laser beams. *Z. Phys. D*, 39:93–100, 1997.

[21] W. Süptitz, B. C. Duncan, and P. L. Gould. Efficient 5D excitation of trapped Rb atoms using pulses of diode-laser light in the counterintuitive order. *J. Opt. Soc. Am. B*, 14(5):463–468, May 1997.

[22] T. Cubel, B. K. Teo, V. S. Malinovsky, J. R. Guest, A. Reinhard, B. Knuffman, P. R. Berman, and G. Raithel. Coherent population transfer of ground-state atoms into Rydberg states. *Phys. Rev. A*, 72(2):023405, Aug 2005.

[23] B. Brezger, Th. Schulze, U. Drodofsky, J. Stuhler, S. Nowak, T. Pfau, and J. Mlynek. Nanolithography with neutral chromium and helium atoms. *J. Vac. Sci. Technol. B*, 15 (6):2905–2911, 1997.

[24] S. Nowak, T. Pfau, and J. Mlynek. Nanolithography with metastable helium. *Appl. Phys. B.*, 63:203–205, 1996.

[25] S. H. Lee. *Coherent Manipulation of Rydberg Helium Atoms in Inhomogenous Electric Fields*. PhD thesis, SUNY Stony Brook, Stony Brook, NY, August 2006.

[26] Thomas F. Gallagher. *Rydberg Atoms*. Cambridge University Press, New York, 1994.

[27] W. N. Hartley. LVI.- on Homologous Spectra. *Journal of the Chemical Society*, 43:390, 1883.

[28] J. R. Rydberg. On the structure of the line spectra of the chemical elements. *Phil. Mag. 5th Ser*, 29:331, 1890.

[29] Myron L. Zimmerman, Michael G. Littman, Michael M. Kash, and Daniel Kleppner. Stark structure of the Rydberg states of alkali-metal atoms. *Phys. Rev. A*, 20(6):2251–2275, Dec 1979.

[30] M. D. Lukin, M. Fleischhauer, R. Cote, L. M. Duan, D. Jaksch, J. I. Cirac, and P. Zoller. Dipole blockade and quantum information processing in mesoscopic atomic ensembles. *Phys. Rev. Lett.*, 87(3):037901, Jun 2001.

[31] T. Förster. *Modern Quantum Chemistry*. Academic Press, New York, 1996.

[32] I. Mourachko, D. Comparat, F. de Tomasi, A. Fioretti, P. Nosbaum, V. M. Akulin, and P. Pillet. Many-Body effects in a frozen Rydberg gas. *Phys. Rev. Lett.*, 80(2):253–256, Jan 1998.

[33] M. P. Robinson, B. Laburthe Tolra, Michael W. Noel, T. F. Gallagher, and P. Pillet. Spontaneous evolution of Rydberg atoms into an ultracold plasma. *Phys. Rev. Lett.*, 85 (21):4466–4469, Nov 2000.

[34] Igor I. Ryabtsev, Denis B. Tretyakov, and Ilya I. Beterov. Spontaneous evolution of Rydberg atoms into an ultracold plasma. *J. Phys. B: At. Mol. Opt. Phys.*, 38(2):S421–S436, Jan 2005.

[35] M. J. Seaton. Quantum defect theory. *Reports on Progress in Physics*, 46(2):167, Feb. 1983.

[36] C. J. Lorenzen and K. Niemax. Quantum defects of the $n^2P_{1/2,3/2}$ levels in ^{39}KI and ^{85}RbI. *Physica Scripta*, 27(4):300–305, July 1983.

[37] T F Gallagher. Rydberg atoms. *Rep. Prog. Phys.*, 51:143–188, 1988.

[38] Thomas Bergeman. *Department of Physics and Astronomy, Stony Brook University*.

[39] H. Rinneberg, J. Neukammer, G. Jönsson, H. Hieronymus, A. König, and K. Vietzke. High n Rydberg atoms and external fields. *Phys. Rev. Lett.*, 55(4):382–385, Jul 1985.

[40] G. W. F. Drake. Theory of relativistic magnetic dipole transitions: Lifetime of the metastable 2^3s state of the helium-like ions. *Phys. Rev. A*, 3(3):908–915, Mar 1971.

[41] A. Derevianko and W. R. Johnson. Two-photon decay of 2^1S_0 and 2^3S_1 states of helium-like ions. *Phys. Rev. A*, 56(2):1288–1294, Aug 1997.

[42] H. Hotop. *Experimental Methods in the Physical Sciences*, volume 29B. Academic Press, New York.

[43] M. R. Williams, F. Chi, M. T. Cashen, and H. Metcalf. Bichromatic force measurements using atomic beam deflections. *Phys. Rev. A*, 61(2):023408, Jan 2000.

[44] A. Vernaleken. Stark spectroscopy and atom optics with Rydberg helium atoms. Master's thesis, SUNY Stony Brook, Stony Brook, NY, August 2006.

[45] K. Shimizu F. Shimizu J. Kawanaka, M. Hagiuda and H. Takuma. Generation of an intense low-velocity metastable-Neon atomic beam. *Appl. Phys. B: Lasers Opt.*, 56: 21–24, 1993.

[46] H. C. Mastwijk, J. W. Thomsen, P. Van der Straten, and A Niehaus. Optical collisions of cold, metastable helium atoms. *Phys. Rev. Lett.*, 80(25):5516–5519, Jun 1998. ISSN 0031-9007.

[47] Claire Allred. *Neutral Atom Lithography with Metastable Helium*. PhD thesis, SUNY Stony Brook, Stony Brook, NY, May 2009.

[48] J. L. Wiza. Microchannel plate detectors. *Nuclear Instruments and Methods*, 162: 587–601, 1979.

[49] R. D. Rundel F. B. Dunning and R. F. Stebbings. Determination of secondary electron ejection coefficients for rare gas metastable atoms. *Rev. Sci. Instrum.*, 46(6):697–701, 1975.

[50] R. V. Pound. Electronic frequency stabilization of microwave oscillators. *Rev. Sci. Inst.*, 17:490, 1946.

[51] R. W. Drever and J. L. Hall. Laser phase and frequency stabilization using an optical resonator. *Appl. Phys. B*, 31:97, 1983.

[52] T.W. Hänsch and B. Couillaud. Laser frequency stabilization spectroscopy of a reflecting reference cavity. *Optics Communications*, 35(3):441, 1980.

[53] C. J. Foot. *Atomic Physics*, volume 7 of *Oxford Master Series in Physics*. Oxford University Press, Oxford, UK, 2005.

[54] T. W. Hänsch, I. S. Shahin, and A. L. Schawlow. High-resolution saturation spectroscopy of the sodium D lines with a pulsed tunable Dye Laser. *Phys. Rev. Lett.*, 27 (11):707–710, September 1971.

[55] Jason Reeves. *Neutral Atom Lithography Using the 389 nm Transition in Metastable Helium*. PhD thesis, SUNY Stony Brook, Stony Brook, NY, August 2010.

[56] Eric D. Black. An introduction to Pound-Drever-Hall laser frequency stabilization. *Am. J. Phys.*, 69(1):79–87, January 2001.

[57] *Instruction manual, CW single-frequency ring Ti:Sapphire laser model TIS-SF-07, Tekhnoscan Company.*

[58] M. C. Keller. Optical manipulation of helium atoms with application to neutral atom lithography. Master's thesis, SUNY Stony Brook, Stony Brook, NY, August 2006.

[59] M. Cashen, O. Rivoire, L. Yatsenko, and H. Metcalf. Coherent exchange of momentum between atoms and light. *Journal of optics B–quantum and semiclassical optics*, 4(1): 75–79, Feb. 2002.

[60] M. R. Williams. *Measurement of the Bichromatic Force on Rubidium Atoms*. PhD thesis, SUNY Stony Brook, Stony Brook, NY, August 1999.

[61] A. Einstein. Zur Quantentheorie der Strahlung. *Physikalische Zeitschrift*, 18:121, 1917.

[62] I. I. Rabi. Space quantization in a gyrating field. *Phys. Rep.*, 51:652, 1937.

[63] X. Miao. *Optical Force on Atoms with Periodic Adiabatic Rapid Passage Sequences*. PhD thesis, SUNY Stony Brook, Stony Brook, NY, August 2006.

[64] Benjamin Simon Gläßle. Properties of adiabatic rapid passage sequences. Master's thesis, SUNY Stony Brook, Stony Brook, NY, August 2009.

[65] F. T. Hioe and J. H. Eberly. N-level coherence vector and higher conservation laws in quantum optics and quantum mechanics. *Phys. Rev. Lett.*, 47:838, 1981.

[66] J. Oreg, F. T. Hioe, and J. H. Eberly. Adiabatic following in multilevel systems. *Phys. Rev. A*, 29(2):690–697, Feb 1984.

[67] U. Gaubatz, P. Rudecki, M. Becker, S. Schiemann, M. Kulz, and K. Bergmann. Resonant light pressure forces in a strong standing laser wave. *Chem. Phys. Lett.*, 149:463, 1988.

[68] U. Gaubatz, P. Rudecki, S. Schiemann, and K. Bergmann. Population transfer between molecular vibration levels. *J. Chem. Phys.*, 92:5363, 1990.

[69] J. R. Kuklinski, U. Gaubatz, F. T. Hioe, and K. Bergmann. Adibatic population transfer in a three-level system driven by delayed laser pulses. *Phys. Rev. A*, 40(3):6741, 1989.

[70] N. V. Vitanov, M. Fleischhauer, B. W. Shore, and K. Bergmann. Coherent manipulation of atoms and molecules by sequential laser pulses. *Adv. Atom. Mol. Opt.*, 46:55, 2001.

[71] N. V. Vitanov and S. Stenholm. Properties of stimulated Raman adiabatic passage with intermediate-level detuning. *Opt. Comm.*, 135:394–405, 1997.

[72] V. I. Romanenko and L. P. Yatsenko. Adiabatic population transfer in the three-level λ system: two photon lineshape. *Opt. Comm.*, 140:231–236, 1997.

[73] N. V. Vitanov, T. Halfmann, B. W. Shore, and K. Bergmann. Laser-induced population transfer by adiabatic passage techniques. *Annu. Rev. Chem.*, 52:763–809, 2001.

[74] A. F. Linskens, I. Holleman, N. Dam, and J. Reuss. Two-photon Rabi oscillations. *Phys. Rev. A*, 54(6):4854–4862, Dec 1996.

[75] T. A. Johnson, E. Urban, T. Henage, L. Isenhower, D. D. Yavuz, T. G. Walker, and M. Saffman. Rabi oscillations between ground and Rydberg states with dipole-dipole atomic interactions. *Phys. Rev. Lett.*, 100(11):113003, Mar 2008.

[76] M. T. Cashen and H. Metcalf. Bichromatic force on helium. *Phys. Rev. A*, 63(2):025406, Jan 2001.

[77] M. Partlow, X. Miao, J. Bochmann, M. Cashen, and H. Metcalf. Bichromatic slowing and collimation to make an intense helium beam. *Phys. Rev. Lett.*, 93(21):213004, Nov 2004.

[78] L. Allen and J. H. Eberly. *Optical Resonance and Two-Level Atoms*. Dover Publications, Inc., New York, 1987.

[79] R. Grimm, J. Soding, and Yu. B. Ovchinnikov. Coherent beam splitter for atoms based on a bichromatic standing light wave. *Optics Letters*, 19(9):658, May 1994.

[80] S. H. Autler and C. H. Townes. Stark effect in rapidly varying fields. *Phys. Rev.*, 100 (2):703–722, Oct 1955.

[81] Constantine E. Theodosiou. Lifetimes of singly excited states in He I. *Phys. Rev. A*, 30 (6):2910–2921, Dec 1984.

[82] J. Martin, B. W. Shore, and K. Bergmann. Coherent population transfer in multilevel systems with magnetic sublevels. iii. experimental results. *Phys. Rev. A*, 54(2):1556–1569, Aug 1996.

[83] G. M. Lankhuijzen and L. D. Noordam. Rydberg ionization: From field to photon. *Advances In Atomic, Molecular, and Optical Physics*, 38:121, Sept. 1998.

[84] F. Robicheaux. Ionization due to the interaction between two Rydberg atoms. *Journal of Physics B: Atomic, Molecular and Optical Physics*, 38(2):S333, Jan 2005.

[85] F. M. Penning. Über ionisation durch metastable atom. *Naturwiss*, 15:818, 1927.

[86] I. L. Glukhov and V. D. Ovsiannikov. Thermal photoionization of rydberg states in helium and alkali metal atoms. *J. Phys. B: At. Mol. Opt. Phys.*, 42(7):075001, January 2009.

[87] I. L. Glukhov, E. A. Nekipelov, and V. D. Ovsiannikov. Blackbody-induced decay, excitation and ionization rates for Rydberg states in hydrogen and helium atoms. *J. Phys. B: At. Mol. Opt. Phys.*, 43(12):125002, June 2010.

[88] I. I. Beterov, D. B. Tretyakov, I. I. Ryabtsev, V. M. Entin, A. Ekers, and N. N. Bezuglov. Ionization of Rydberg atoms by blackbody radiation. *New Journal of Physics*, 11: 013052, January 2009.